University of Zurich^UZH

Background Measurement and MC Simulations for the DARWIN Demonstrator

---

Master Thesis

Professor:
Prof. Dr. Laura Baudis

Supervision:
Dr. Patricia Sanchez, Dr. Neil McFadden

Student:
Stefan Hochrein

Date:
November 26, 2021

Acknowledgements

At this point I would like to thank Prof. Laura Baudis for giving me the opportunity to do my master thesis in this interesting and promising field of research. Although I already wrote my bachelor thesis in the group, I learned a lot of new things throughout my work. This is mainly thanks to Dr. Patricia Sanchez, who invested a lot of time and effort in my project, especially after Dr. Neil McFadden left the university. For this, and for always finding time for my questions and discussions, I would like to express my sincere thanks. Of course I would also like to thank Neil, who contributed many ideas in the first phase of the project. Furthermore I would like to thank Frédéric Girard who helped me a lot, especially with the setup design. Moreover, I would like to thank Kevin Thieme, Alexander Bismark, Yanina Biondi, Ricardo Peres, Giovanni Volta, Dr. Michelle Galloway, and Dr. Christian Wittweg, who always helped me with advice and practical support. Also, many thanks to Andreas James for the help with the collimator.

Finally, I would also like to thank my girlfriend, family and friends for their support outside the university life.

Contents

Introduction

It was almost 100 years ago, when the Swiss-American astronomer Fritz Zwicky for the first time inferred the possible existence of dark matter, that is, matter that has mass but does not interact with light [1]. Due to a multitude of experiments and technical advances, evidence has accumulated over the years and has led to the development of the standard model of cosmology, in which about 26% of the universe consist of cold dark matter [2]. Nevertheless, its existence could not be proven directly yet.

At this point, a broad range of experiments is trying to fill this gap in knowledge with many different detection ideas and experimental setups. The currently most promising dark matter experiments use so called dual-phase time projection chambers (TPCs) to set limits to possible dark matter masses and scattering cross sections [3]. DARWIN, a next-generation experiment, employing this same detector technology, will further investigate this open issue. It will use a target of 40 t of liquid xenon to reach unprecedented sensitivity to weakly interacting dark matter with masses above $5\,\mathrm{GeV/c^2}$. In addition, its ultra-low background will make DARWIN competitive in other physics channels, including neutrinoless double beta decay and solar neutrinos [4]. Building such a detector requires, however, technological advances and new ideas to solve arising problems. To test the feasibility of the DARWIN project, an R&D detector was designed and built at the University of Zurich, called Xenoscope. It has a similar working principle and the full 2.6 m height of the DARWIN TPC and serves therefore as its Vertical Demonstrator. The main goal of Xenoscope is to prove for the first time that it is, indeed, possible to drift electrons over such a long distance in liquid xenon [5].

In order to calibrate and run Xenoscope, it is crucial to know the expected background rate in the detector. Determining this background rate and finding out which sources can be used to calibrate the detector are the main goals of this work. To this end, first, the radiogenic background in the lab was measured with a thallium doped sodium-iodide (NaI(Tl)) detector. From the measurements, the extent of radiation hitting the detector was derived. Using Geant4 [6], a Monte Carlo software for the simulation of the passage of particles through matter, the amount of energy deposited inside the detector was determined. Further, the expected signal of different internal and external calibration sources was simulated by the same means. For the external sources, additionally, a calibration setup was designed and incorporated in the simulation geometry, which will be built once its needed. Finally, the simulated events were analyzed to find the background rate and to identify the sources that are best suited for calibrations in different energy ranges as well as their required activities.

This thesis is structured as follows: In the first chapter, open questions and current experiments in dark matter and neutrino physics are discussed. In chapter 2, the DARWIN project is presented and its detection principle is explained. A special focus is placed on the DARWIN Vertical Demonstrator located at the University of Zurich. In chapter 3, the background measurements in the experimental hall with an NaI(Tl) detector, and the corresponding data analysis, is shown. Chapter 4 is then dedicated to the simulations of the background an calibration sources. The analysis and results of the whole procedure are shown in chapter 5. Finally, in chapter 6, the findings are summarized and discussed.

1 Dark Matter Research and Neutrino Physics

The direct search for dark matter is a relatively new field of physics which quickly gained momentum in the last decades. Since the early 2000s, the sensitivity of dark matter experiments has increased by an order of magnitude roughly every three years [7]. This development has opened new perspectives for multipurpose ultra-low background experiments: The next generation of dark matter experiments will have excellent sensitivity to various dark matter candidates, as well as to additional physics channels like the neutrinoless double β-decay and solar neutrinos.

In this chapter, first, the evidence for dark matter, current detection ideas, and dark matter experiments are introduced. The second section addresses neutrinos, an additional physics channel for extremely sensitive detectors. Finally, in the third section, the chances and challenges of a simultaneous search for dark matter and neutrinos are briefly discussed.

1.1 Dark Matter

The standard model of cosmology, Λ Cold Dark Matter (ΛCDM), suggests that the constituents of our universe are still unknown for the most part. It predicts that only ~5 % of the universe consists of well-known matter and radiation. The rest of its density is composed of cold dark matter (CDM) and dark energy, which account for ~26 % and ~69 % respectively [2]. However, even though the existence of dark matter can be inferred from its gravitational effects, it has never been directly measured to this date. The search for dark matter is one of the major open research fields of modern physics.

This section starts with the evidence for dark matter that led to the development of the ΛCDM-model. Then, possible candidates for dark matter are briefly presented. The section concludes with an overview of current experiments aiming to prove the existence of dark matter.

1.1.1 Evidence for Dark Matter

Dark matter was first mentioned in a paper by Fritz Zwicky in 1933 [1]. Over the years, evidence accumulated due to novel astrophysical and cosmological observations benefiting from better technical capabilities. In the following subsections, the milestones in dark matter research, that led to the development of the ΛCDM-model, are presented in chronological order.

Rotation of Galaxies and Stars

In 1933, the Swiss-American astronomer Fritz Zwicky found the first indication of dark matter in the Coma Cluster. As he tried to estimate the mass of the cluster using two different methods, a large discrepancy emerged. The first method, an estimate of the visible mass based on the brightness of the cluster, resulted in a mass 400 times smaller than the second method, an estimate of the gravitational mass based on the measurement of the orbital velocities of galaxies around the cluster's center. Zwicky suggested that this inconsistency could be solved by a new type of matter that does not interact with light, which he, therefore, called *Dunkle Materie*, German for dark matter [1].

A similar piece of evidence was found by Vera Rubin in 1978, analyzing the velocities of stars around the galactic center of ten disk galaxies. Newtonian dynamics predict a radius-dependent orbital velocity, $v_{orb}(r)$, related to the mass enclosed by the orbit, $M(r)$, of

$$v_{orb}(r) = \sqrt{\frac{G \cdot M(r)}{r}}, \tag{1.1}$$

where G is the gravitational constant. Taking into account the visible mass only, the prediction differed from the velocities measured using the redshift of the respective stars, especially at large radii. This measurement allowed for the first time to map the dark matter distribution (dark matter halo) in a galaxy [8]. A schematic of such a study is shown in figure 1 (a). It can be seen that at large radii, instead of decreasing, the orbital velocity levels out to a constant value. Solving formula 1.1 for the mass, and substituting $M = \rho \cdot V$, then yields a dark matter halo density distribution $\rho \propto 1/r^2$.

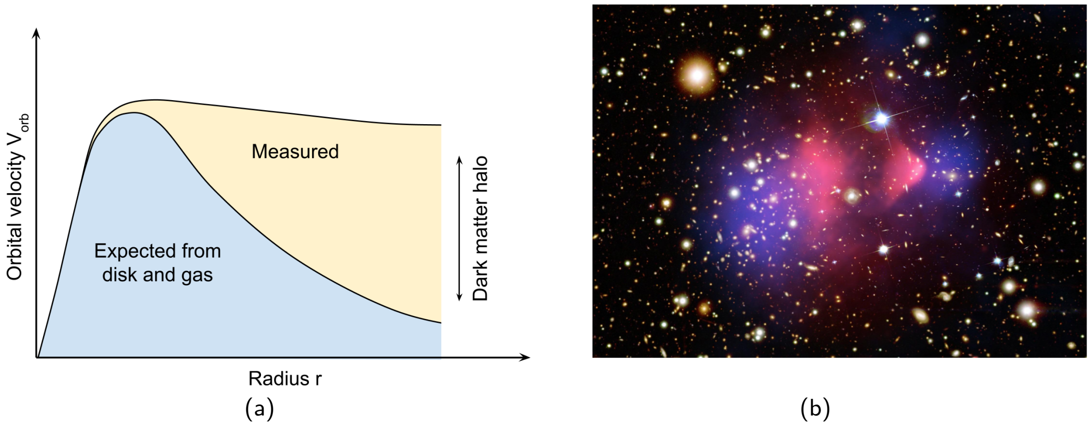

(a) (b)

Figure 1: (a): Schematic of the orbital velocities of stars in a disk galaxy as a function of the radius. The measured velocities at large radii are much higher than expected from the visible mass. Figure created based on [9]. (b): Baryonic mass (pink) and gravitational mass (blue) distribution in the Bullet Cluster merger (1E 0657-558). Figure from [10] based on data presented in [11].

Gravitational Lensing

A very strong indication for dark matter was observed in 2006 in the merger of the Bullet Cluster. Using the effect of gravitational lensing, that is the bending of light trajectories by large masses according to Einstein's general relativity, Douglas Clowe and his team mapped the gravitational mass distribution in the cluster merger. Once again, the mass was estimated in a second way, by detecting X-rays from the heated-up gas clouds, the dominant baryonic mass component in the cluster. While the gas slows down in the merger due to friction, dark matter continues its initial trajectory [11]. Therefore, the mass distributions are shifted with respect to each other, as can be seen in figure 1 (b).

Cosmic Microwave Background Radiation

The most important evidence for dark matter today comes from the precise measurement of the cosmic microwave background (CMB). The CMB was discovered in 1965 by Penzias and Wilson [12]. It provides information about the early universe because it consists of radiation released during recombination area, about 380 000 years after the Big Bang. At this time, electrons became bound to nuclei forming neutral atoms, which made the universe transparent to light. Density fluctuations in the early universe, sensitive to the proportion of ordinary matter and dark matter, are since then imprinted in the CMB [13]. The latest measurements by the Planck satellite show that the CMB follows an almost perfect black body radiation spectrum with a temperature of about 2.7 K, interspersed with small anisotropies of $\mathcal{O}(10^{-5}\,\mathrm{K})$, as shown in figure 2. These fluctuations produce several peaks in the angular power spectrum, as shown in figure 3. The best fit to the data is achieved with the ΛCDM-model including a cold dark matter density ($\Omega_c h^2$) of [14]:

$$\Omega_c h^2 = 0.11933 \pm 0.00091, \tag{1.2}$$

where h is the dimensionless Hubble constant. This corresponds to dark matter accounting for 26.07% of the density of the universe.

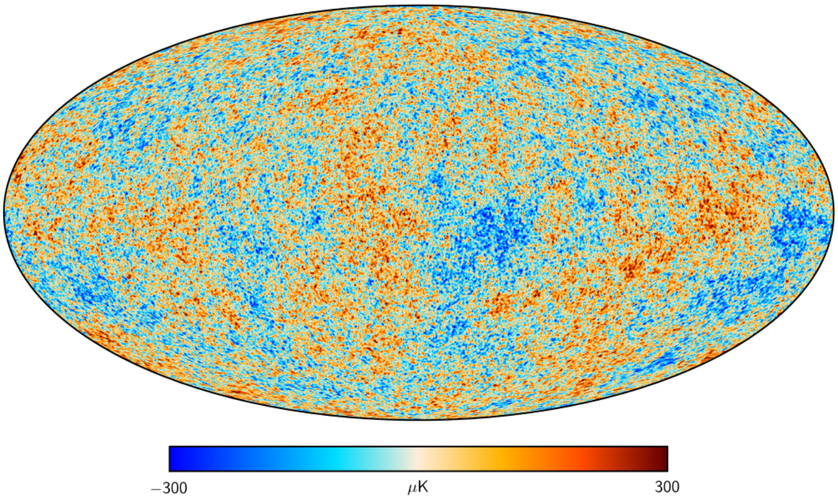

Figure 2: Map of the CMB temperature with its fluctuations across the sky, as measured by the Planck experiment in 2015. Warmer regions are shown in red while cooler region are colored in blue. Figure from [15].

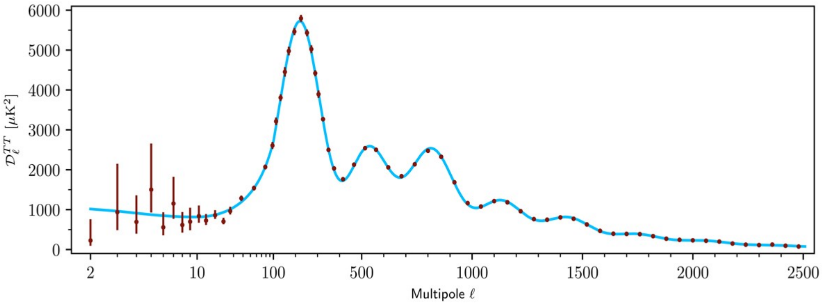

Figure 3: CMB power spectrum: The red dots show the CMB temperature fluctuations as a function of the multipole moment l. The blue line, showing a fit based on the ΛCDM-model including dark matter, is in excellent agreement with the data. Figure from [16].

1.1.2 Dark Matter Candidates

Even though evidence for dark matter accumulated over the past decades, its nature is completely unknown. However, some properties can already be inferred from astrophysical and cosmological observations. The ΛCDM-model assumes gravitationally interacting and stable particles. They must be neutral with respect to the strong and electromagnetic forces, while the possibility of weakly interacting dark matter cannot be ruled out. Furthermore, dark matter must be relatively slow (non-relativistic) in order to be bound to galaxies. These constraints rule out all standard model (SM) particles.
Nevertheless, the list of dark matter candidates is quite broad and the composition of dark matter from multiple candidates cannot be ruled out. Ideas range from baryonic massive astrophysical compact halo objects (MACHOs), for example brown and white dwarfs, stellar black-hole remnants, and neutron stars, to new particles species, as sterile neutrinos, weakly interacting massive particles (WIMPs), and axions. There are even theories trying to explain some of the observations mentioned above without a particles, for example by modified Newton dynamics (MOND) [7]. In the following subsections, two of the most promising candidates are discussed in more detail.

WIMPs and the WIMP Miracle

WIMPs are a type of particles arising in extensions of the SM. Among the most popular candidates are the hypothetical neutralino and sneutrino from supersymmetric theories. WIMPs have masses in the GeV-TeV range and, as their name suggests, interact with SM particles only through the weak interaction. Besides the fact that many theories predicting WIMPs already exist, they are attractive candidates for dark matter for two more reasons. Firstly, because of their interaction with baryonic matter, WIMPs can be detectable, meaning that the WIMP hypothesis can be tested. Secondly, there exists a WIMP production mechanism that can explain the abundance of dark matter observed today in the universe. Let us assume a hypothetical dark matter particle χ. In the hot and dense early universe, this particle existed in an equilibrium with SM particles, maintained by the counterbalancing annihilation and production processes $\chi\bar{\chi} \rightleftharpoons \mathrm{l}\bar{\mathrm{l}}$, where l is a lighter SM particle and the bar denotes anti-particles. As the universe expanded and the temperature decreased, it eventually fell below the χ-mass and the χ-production reaction stopped, leading to an exponential drop in its abundance. Later, when the χ-annihilation rate fell below the expansion rate of the universe, the comoving χ number density froze in to a constant value. The dark matter abundance of today is therefore determined by the freeze-out point, that predominantly depends on the χ-annihilation cross section, σ_A, and χ-velocity,v. This mechanism is sketched in figure 4. The remarkable coincidence is that considering σ_A around the weak scale - as predicted by the theoretical supersymmetrical extensions of the electroweak sector - leads to a dark matter abundance very close to what is observed today. This is known as the "WIMP miracle" [7].

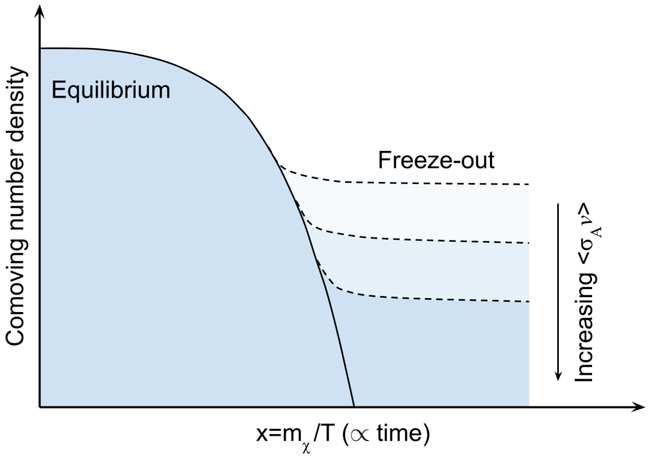

Figure 4: Schematic of the comoving WIMP number density over time, from the early equilibrium short after the Big Bang to the relic abundance after freeze-out today. As shown by the dashed lines, the relic abundance depends on the WIMP velocity, v, and annihilation cross section, σ_A. The higher the cross section and velocity, the later the annihilation reaction stopped, and the less WIMPs remain after freeze-out. Figure based on [17].

Axions and the Strong CP Problem

The commonly called strong CP problem arises from the non-Abelian nature of the quantum chromodynamics (QCD) gauge symmetry. As in the electroweak sector (also non-Abelian), charge-parity (CP) symmetry can in principle be violated. CP violation is one of the necessary condition to explain the matter-antimatter asymmetry observed in our universe today [18]. In the electroweak sector, CP violation was observed in different weak interactions of quarks (quark mixing). It was first measured in 1964 in neutral kaon decays [19]. Only recently, in 2020, also in the lepton sector CP violation was found by the T2K experiment measuring neutrino oscillations [20].

Similarly, the strong interaction could give rise to CP violation proportional to the angle θ describing the QCD vacuum state. However, CP violation in the strong interaction has never been observed. Furthermore, it would naturally generate a neutron electric dipole moment about ten orders of magnitude above the current limit of $d(n) < 0.0 \pm 1.1_{stat} \pm 0.2_{sys} \times 10^{-26}\, e$.cm [21]. Peccei and Quinn solved this problem by introducing a new global $U(1)_{PQ}$ symmetry [22]. Spontaneous breaking of the $U(1)_{PQ}$ symmetry yields an initially massless Nambu–Goldstone boson, called the axion. Non-perturbative effects result in a potential for the axion, causing it to acquire mass and relax to the CP conserving minimum of the potential at $\theta = 0$, thus solving the strong CP problem. In this framework, the mass of the axion turns out to be inversely proportional to the arbitrary symmetry breaking scale. Various experiments have already ruled out a large range of axion masses, leaving only the possibility of very light axions with a mass of $\mathcal{O}$(µeV - meV) or axion-like particles (ALPs). ALPs are also Nambu–Goldstone bosons generated by spontaneous breaking of an additional $U(1)$ symmetry, but unrelated to the strong CP problem. ALPs therefore do not have a mass related to the symmetry breaking scale [23, 7].

1.1.3 Looking for Dark Matter

To confirm the ΛCDM-model, the existence of dark matter has to be proven. The goal is to measure the properties of dark matter, for example its mass and interaction cross section, and finding a theory beyond the SM which is able to explain them. So far, no evidence of dark matter interactions, apart from gravitational, have been observed. Nevertheless, a wide range of experiments is looking for such rare interaction processes. They can be categorized into three groups based on the type of events they are looking for: Collider experiments, indirect-, and direct detection.

In the subsections below, the different ideas and techniques behind these experiments are presented, with an emphasis on direct detection.

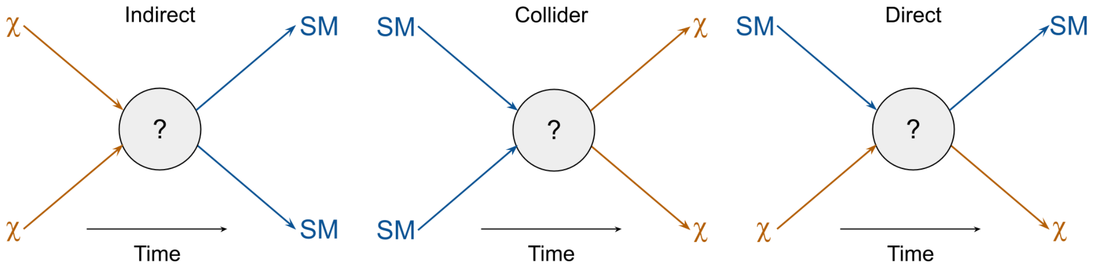

Figure 5: Underlying processes of the different kinds of dark matter detection experiments.

Indirect Detection

Indirect detection experiments are searching for products of dark matter self-annihilation into SM particles, as shown in figure 5, left. These processes are expected to happen predominantly in regions of high dark matter density, such as the Sun, dwarf galaxies, or the galactic center. Possible channels are

$$\chi\bar{\chi} \rightarrow \gamma\gamma,\ \gamma Z,\ \gamma H,\ q\bar{q}, W^+W^-, ZZ. \tag{1.3}$$

The unstable Z, H, and W and the coloured q and $\bar{q}$ further produce $e^+e^-, p\bar{p}, \gamma\gamma$, and neutrinos in the final state. Specialized experiments dedicated to looking for specific final state particles are under operation. Ground-based telescopes like H.E.S.S-II [24], MAGIC [25], VERITAS [26] and CTA [27] are looking for high energy γ-rays that produce Cherenkov light in the atmosphere. Such γ-rays can originate, besides from dark matter annihilation, from various interesting galactic or extragalactic sources. Therefore, indirect searches of dark matter are not the main goal of these experiments. An excess of γ-rays at a well defined energy could, however, indicate a dark matter decay. The same holds for neutrinos, which are also searched with ground based Cherenkov detectors, but because of their small interaction cross section more massive targets are required. Examples are the ice based IceCube [28] and the water based Super-Kamiokande [29] and KM3Net [30]. Finally, cosmic positrons and anti-protons as well as low energy γ-rays that do not reach the earth are measured in satellite based experiments such as PAMELA [31], Fermi-LAT [32] and AMS-2 [33]. PAMELA and AMS-2 reported an excess in cosmic positrons in 2009 and 2013 [34, 35]. However, the measured signal could also be explained by a nearby pulsar and was rejected by Fermi-LAT [36].

Collider Experiments

Dark matter collider experiments are looking for the annihilation of SM particles into dark matter, as shown in figure 5, center. In high energy colliders, like the Large Hadron Collider (LHC) at CERN, the dark matter produced in p-p collisions would escape the detector and show up as missing transverse energy and momentum [37]. Based on this signature, the mass of the missing particle could be reconstructed. So far, no such signal has been detected [38, 39, 40]. Moreover, even if a new particle would be discovered in this way, its validity as dark matter particle would have to be proven by direct detection.

Direct Detection

Direct detection experiments look for scattering processes of dark matter with SM particles, as shown in figure 5, right. They mainly focus on WIMPs elastically scattering off nuclei in earthbound targets, producing nuclear recoils. The recoil energy can be deposited in three different ways, as ionization charge, scintillation light, or phonons/heat. Various experiments exploiting one or two of these signal channels are under operation or being planned, as shown in figure 6.

The first limits on the WIMP-nucleon scattering cross section were obtained in experiments measuring ionization charge in germanium detectors [41]. This technique is still employed in experiments such as CDEX-1B [42]. Other detectors like SuperCDMS [43], EDELWEISS-III [44] and CRESST-III [45] use cryogenic bolometers that can read out phonons in addition to ionization charge or scintillation light. Further, there are experiments, like PICO-60 [46], using bubble chambers filled with superheated liquids to measure heat depositions causing bubble nucleation. Experiments such as DAMA/LIBRA [47] use solid scintillation detectors (in this case NaI(Tl)) looking for annual modulation of dark matter events due to the Earth motion through the dark matter halo. This experiment indeed found such a signal, however, the reported result was rejected by other experiments like ANAIS [48] and COSINE [49] that

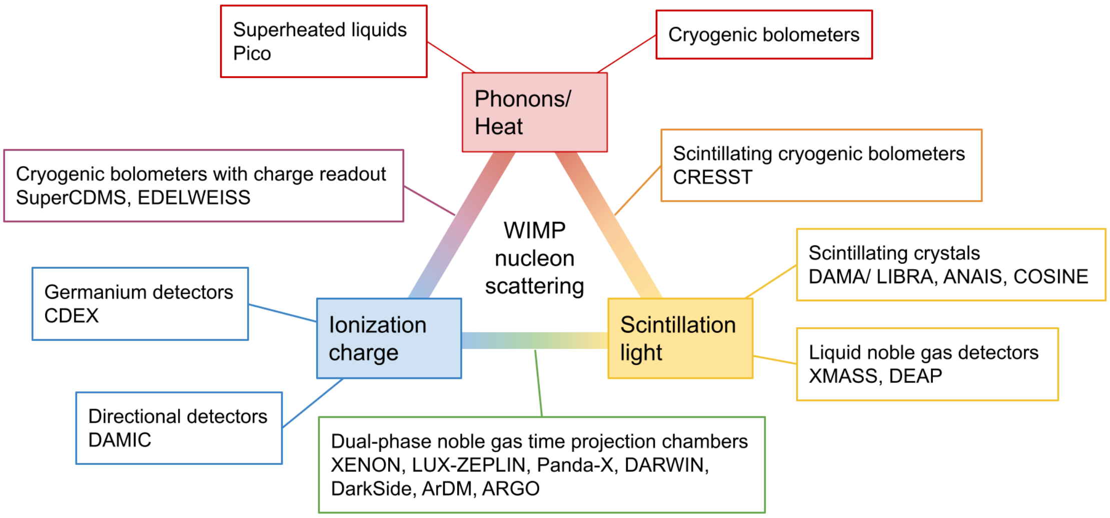

Figure 6: A selection of different present and future direct dark matter detection experiments. The signal(s) they are looking for is indicated by the respective color.

use the same detection technique. Finally, a big family of detectors use (liquid) noble gas as a target material. Some of them use single phase detectors that can only measure scintillation light, like XMASS [50] and DEAP-3600 [51]. However, the most promising detectors today, reaching the best exclusion limits, are dual-phase (liquid/gas) xenon and argon time projection chambers that can measure scintillation light and ionization charge. The ones using liquid argon, like DarkSide-50 [52] and ArDM [53], so far reach worse sensitivities than those using liquid xenon, like XENON1T [3], LUX-ZEPLIN [54] and PandaX-II [55]. XENON1T recently reported an excess of electronic recoil events that could be caused by axions [56]. However, the signal did no reach the 5σ discovery limit and could also be explained by an additional background, e.g., from ^{3}H β-decays.

In order to compare the results of different experiments, the exclusion of WIMPs of certain mass and interaction cross section has to be defined in a target independent way. For this, the expected differential event rate in terms of the recoil energy E_R has to be known. It can be written as [57]:

$$\frac{\mathrm{d}R}{\mathrm{d}E_R} = \frac{\rho_\chi N_T}{m_\chi} \int_{v_{min}}^{v_{esc}} v f(v) \frac{\mathrm{d}\sigma}{\mathrm{d}E_R} \mathrm{d}v, \tag{1.4}$$

where ρ_χ, m_χ, and $f(v)$ are the dark matter density, mass and velocity distribution. N_T is the number of target atoms, and σ is the scattering cross section. Apart from the rate, R, that is measured, only N_T is unambiguously known. Therefore, to compare results, the different experiments have to agree on additional assumptions for ρ_χ and $f(v)$, based on the standard halo model. The local density of the dark matter halo is assumed to be $\rho_\chi = 0.3\,\mathrm{GeV/cm^3}$, based on cosmological observations in the Milky Way similar to the one shown in figure 1 (a). Further, the observed $\rho_\chi \propto 1/r^2$ of the halo can be explained by assuming dark matter behaves as a collisionless gas, compressed by gravity, and following a Maxwell-Boltzmann velocity distribution. The velocity distribution is therefore commonly assumed to be

$$f(v) = \frac{1}{\sqrt{2\pi\sigma_0}} \cdot \exp\left(\frac{-|v^2|}{2\sigma_0^2}\right), \tag{1.5}$$

where the circular velocity dispersion is $\sigma_0 = \sqrt{3/2} \cdot v_0$, with $v_0 \simeq 220\,\text{km/s}$, the velocity of our solar system through the dark matter halo. The integration goes from the minimal velocity that can produce a recoil of energy E_R, v_{min}, up to the maximal velocity for which dark matter remains bound to the Milky Way, $v_{esc} \simeq 544\,\text{km/s}$. The unknown scattering cross section σ can be written in terms of the spin-independent and -dependent WIMP-nucleon cross sections and nuclear form factors in order to compare experiments with different target atoms. Using the expected rate of events, the probability of a null result in a given detector can be calculated for a range of WIMP masses and WIMP-nucleon cross sections. If indeed no excess in the event rate was observed, a region of the parameter space can be excluded. Usually, this is done at the 90 % confidence level. A comparison of the latest results for the WIMP-nucleon spin-independent cross section can be found in figure 7.

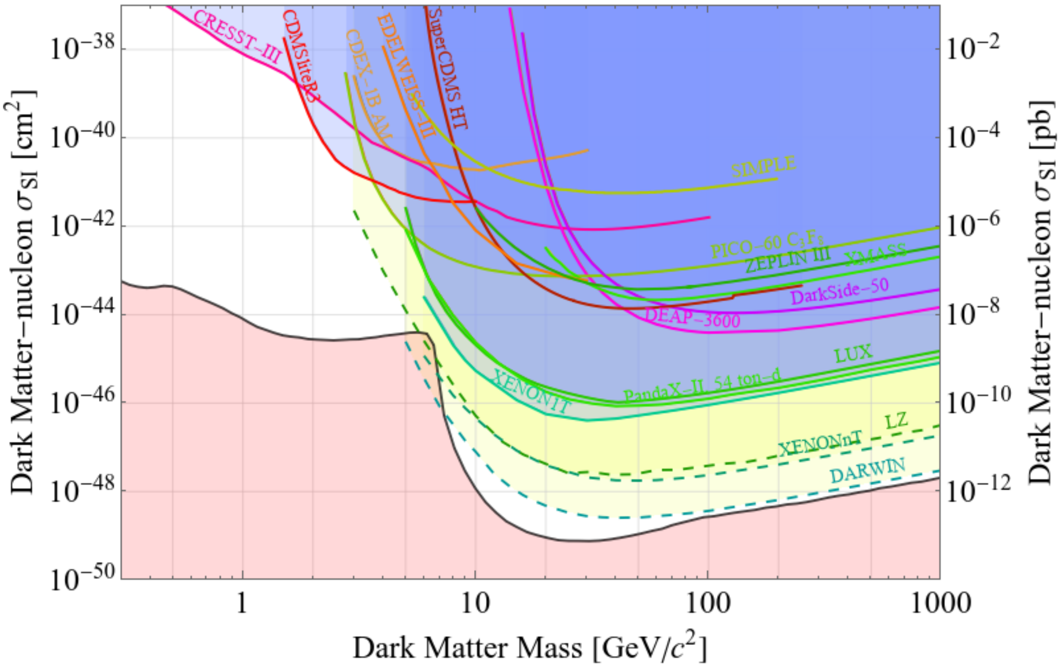

Figure 7: Exclusion limits for the spin-independent WIMP-nucleon cross section of the current experiments along with some future projects. The best current limit is from XENON1T [3]. The already excluded area is shaded in blue. The area that will be covered by future experiments is shown in yellow and the neutrino fog in red. Figure created using [58], based on data published by the individual collaborations.

1.2 Neutrino Physics

In the SM of particle physics, for every charged lepton (e, μ, τ) there is an uncharged counterpart, the neutrino, called ν_e, ν_μ, and ν_τ respectively. Neutrinos were already predicted in 1930 by Wolfgang Pauli based on the electron energy spectrum observed in β-decays [59], as described in section 3.1.2. The first direct detection succeeded in 1953 [60]. However, even today neutrinos are among the most mysterious particles of the SM because they have incredibly small masses of unknown origin and are very hard to detect due to their also small interaction cross section.
This section will give a short insight into neutrino physics and experiments with a focus on neutrino masses and neutrinoless double beta decay, as well as solar neutrinos.

1.2.1 Flavour Oscillations and Neutrino Masses

For a long time neutrinos were assumed to be completely massless. In 1960, R. Davis measured the solar neutrino flux in a radiochemical experiment in the Homestake mine. The result was about $1/3$ of the expected neutrino flux based on the J. Bahcall solar model [61]. This result, later confirmed by other experiments [62, 63], was called the Solar Neutrino Puzzle. A theoretical solution to this problem was found in 1985 by Mikheyev and Smirnov [64], based on the work by Wolfenstein [65]. They explained the low neutrino flux with neutrinos that oscillated into another flavour. The oscillations are based on the nondiagonal nature of the neutrino mixing Pontecorvo–Maki–Nakagawa–Sakata (PMNS) matrix. Wolfenstein realized that the equations need to be modified for the passage of neutrinos through matter. However, such flavor oscillations are only possible if neutrinos have mass because they are, analogous to quark mixing, introduced by the Dirac mass term. In 1998 Super-Kamiokande announced the first observation of atmospheric ν_μ neutrino oscillations [66]. The Solar Neutrino Puzzle was finally solved in 2002 by the Sudbury Neutrino Observatory (SNO) collaboration. The key to their discovery was that the detector was not only sensitive to ν_e, that are predominantly produced in the Sun, but also to ν_μ, and ν_τ. SNO proved that the missing ν_e had oscillated on their way from the Sun to Earth into neutrinos of another flavor [67]. Since then, several neutrino-appearance and -disappearance experiments, like OPERA [68], T2K [69], and MINOS [70], have been conducted in order to constrain the oscillation probability, which provides information about the squared neutrino mass difference. Today the squared mass differences are tightly constrained. Nonetheless, the absolute neutrino masses and the mass ordering are still unknown.

1.2.2 Dirac and Majorana Mass Terms and the Seesaw Mechanism

In quantum field theory (QFT) the neutrino masses can in principle be generated with a Dirac mass term analogously to the masses of the down type quarks using the conjugate Higgs doublet Φ_c. This neutrino Yukawa term reads

$$\mathcal{L}_{Yuk,\nu} = -\sum_{i,j} \left(\bar{L}^i_L \lambda_{ij} \Phi_c \nu^j_R + h.c. \right) , \tag{1.6}$$

where $\bar{L}_L$ is the left-handed lepton doublet, λ is the Yukawa coupling, and ν_R is the right-handed neutrino. After spontaneous symmetry breaking, this term leads to the neutrino masses $m_i = \frac{\lambda_i}{\sqrt{2}} v$, where, v is the Higgs vacuum expectation value. Assuming non-zero Yukawa couplings, this mass term can explain the observed neutrino oscillations. However, the neutrino masses are at least ten orders of magnitude smaller than the quark- and other lepton masses. There is no satisfying reason why the neutrino couplings should be so much smaller than the other Yukawa couplings.

A solution to this problem could be provided by the right-handed neutrinos. They are the only SM particles carrying zero $SU(3)$ and $SU(2) \times U(1)$ quantum numbers. Therefore, they are the only SM particles being their own anti-particles and thus fulfilling the Majorana condition (invariance under charge conjugation: $\psi = \psi^c$). This allows them to have an additional mass term called the Majorana mass term:

$$\mathcal{L}_{Maj,\nu} = -\frac{1}{2} \sum_{i,j} \left(\bar{\nu}^c_{R,i} M_{ij} \nu_{R,j} + h.c. \right). \tag{1.7}$$

The Majorana mass term is not related to the Higgs mechanism and can be generated by a non-renormalizable dimension five operator, suppressed by the energy scale Λ at which a grand unified theory (GUT) is expected. Diagonalyzing the overall mass matrix produced by the two mass terms yields three very light eigenstates, scaled by $1/\Lambda$, and three heavy eigenstates. This effect, commonly referred to as the Seesaw mechanism, could be an explanation for the very light neutrino masses [71].

1.2.3 Neutrinoless Double Beta Decay

A direct implication of the Majorana mass term is that the neutrino would be its own anti-particle. This makes possible a process called neutrinoless double beta decay ($0\nu\beta\beta$). As can be seen in the schematic shown in figure 8, this is a double beta decay in which the two neutrinos annihilate. More information about β-decays can be found in section 3.1.2.

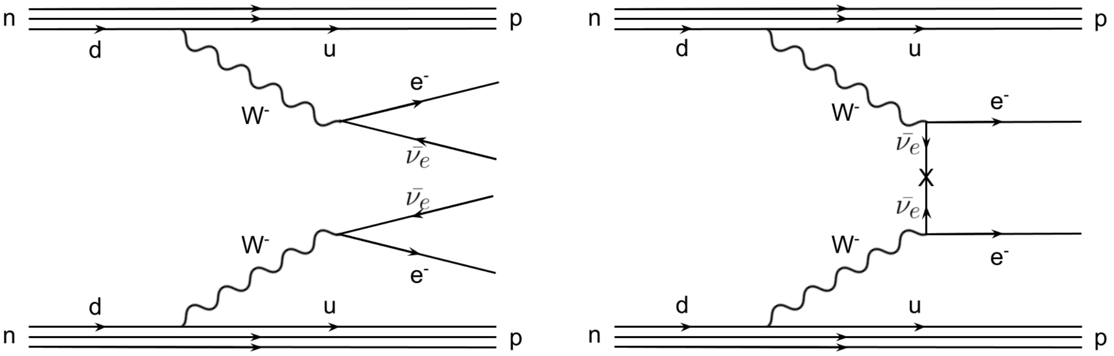

Figure 8: Feynman diagrams of the $2\nu\beta\beta$-decay (left) compared to the $0\nu\beta\beta$-decay (right). Because the final state neutrinos can not be measured due to their small interaction cross section, these processes can only be distinguished based on the electron energy distribution.

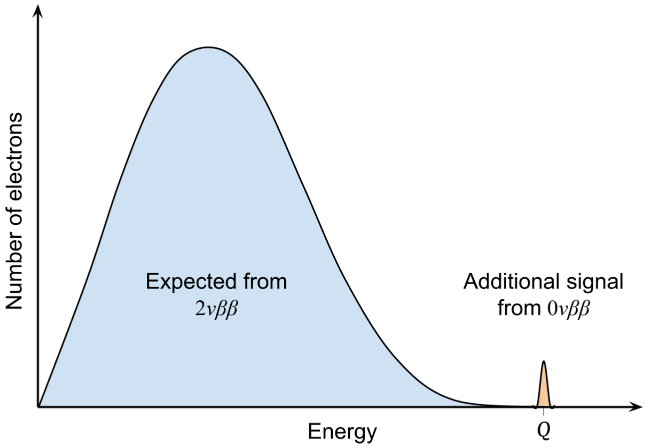

Figure 9: (b): Schematic of the summed up electron energy spectrum in a $2\nu\beta\beta$-decay and the expected additional signal from $0\nu\beta\beta$-decay. The width of the $0\nu\beta\beta$ peak is only due to the finite energy resolution of a detector. For an ideal detector the signal would be a δ-function.

This process would have a very clear signature, a sharp peak at the Q-value, because the two electrons carry the whole available decay energy, as can be seen in figure 9. Because of the small neutrino scattering cross section it would, however, also be extremely suppressed with respect to the already rare normal double β-decay ($2\nu\beta\beta$), which can only be measured in a few isotopes. The $2\nu\beta\beta$-decay was first measured by Inghram and Reynolds in 1950 using ^{130}Te. This experiment was based on measuring the daughter nuclei and was therefore unable to distinguish between $0\nu\beta\beta$ and $2\nu\beta\beta$ [72]. The first direct observation of the $2\nu\beta\beta$-decay, measuring the electron energy spectrum of ^{82}Se, was achieved in 1987 in a time projection chamber [73]. On the other hand, the $0\nu\beta\beta$-decay has never been observed to this date. Experiments, exploiting different detection techniques, are looking for this process in various isotopes. The theoretically expected $0\nu\beta\beta$-decay rate depends on the effective Majorana mass, that is defined as $\langle m_{ee}\rangle = |\sum_{i=1}^{3} U_{ei}^2 m_i|$ where m_i are the diagonalized neutrino masses and U is the neutrino mixing PMNS matrix. Thus, based on a null result and the background model, a limit on $\langle m_{ee}\rangle$ can be calculated for all experiments. However, a proper comparison between experiments using different isotopes is almost impossible because the results strongly depend on the respective nuclear matrix elements which are not very well known. For a given lightest neutrino mass, $\langle m_{ee}\rangle$ differs depending on whether the mass ordering is normal or inverted. Therefore, $0\nu\beta\beta$-decay experiments are also sensitive to the neutrino mass ordering, as can be seen in figure 10.

The best current limit for the half-life of ^{136}Xe is set by KamLAND-Zen [74] in a Xe-loaded liquid scintillator. Future experiments with larger amounts of ^{136}Xe, such as nEXO [75] and NEXT-100 and NEXT-HD [76] are already planned. Other experiments, like GERDA [77] and MAJORANA [78] used solid state germanium diodes enriched in ^{76}Ge to look for $0\nu\beta\beta$-decay. GERDA was the first experiment to reach zero background in the region of interest. LEGEND, a merged collaboration from GERDA and MAJORANA, will further improve the $\langle m_{ee} \rangle$ limit in the LEGEND-200 (under construction) and LEGEND-1000 (planned) experiments [79]. Finally, experiments like CUORE [80] use cryogenic bolometers to search for $0\nu\beta\beta$-decay in ^{130}Te. Also for this type, follow-up experiments such as CUPID [81] are being planned.

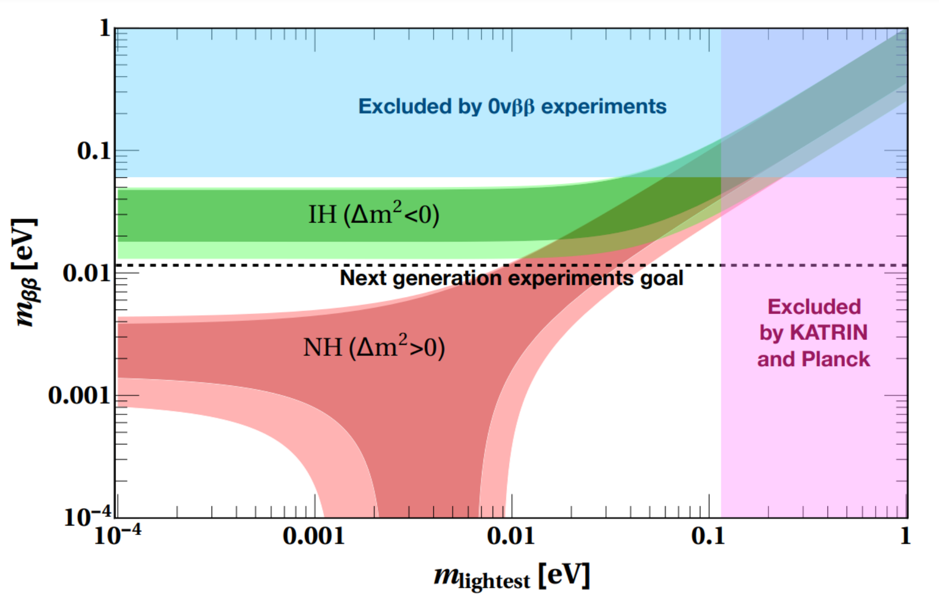

Figure 10: Effective Majorana mass $m_{\beta\beta} = \langle m_{ee} \rangle$ plotted against the mass of the lightest neutrino for the case of normal- (NH) and inverted (IH) mass hierarchy. The region excluded by $0\nu\beta\beta$-experiments is shaded in blue. Figure from [82], modified from [83].

1.2.4 Solar Neutrinos

Neutrinos are not only interesting objects of research themselves, but are also carrying information about other physical phenomena. An example are the solar neutrinos which are produced by various processes in the Sun. While the sunlight we see on Earth originates predominantly from the Sun's surface, neutrinos can reach the Earth from everywhere inside the Sun due to their small interaction cross section. Their energy spectrum therefore contains information about the internal structure of the Sun as for example about the relative importance of the different fusion and decay processes in which neutrinos are produced.
Several experiments have measured solar neutrinos, as already mentioned in section 1.2.1. After the SNO experiment which solved the solar neutrino problem, mainly Borexino remains to be mentioned. This experiment achieved an energy threshold of 0.19 MeV, measured solar ^{8}B neutrinos with high precision, and for the first time detected solar ^{7}Be, pep, pp, and CNO neutrinos [84, 85, 86]. However, the measured fluxes still permit several slightly varying solar models and therefore need to be determined with higher accuracy.

1.3 Simultaneous Search for Dark Matter and Neutrinos

In this chapter, various experiments employing diverse detection techniques for the search of dark matter, $0\nu\beta\beta$-decay and solar neutrinos have been presented. Despite large differences, it is noticeable that these experiments push in the same direction: They all belong to the class of rare event searches that have the main goal of reducing the background hiding a possible signal. Although the potential signals are expected at different energies, this is generally done by the same means. Low background experiments actively and passively shield the detector, carefully select materials with low radioactivity, and an additionally rejection background event-by-event in the data analysis. It can also be noticed that in the last decades, most experiments scaled up their target mass in order to increase the exposure and raise the chance of measuring a signal. These developments make it increasingly difficult and expensive for experiments to improve their sensitivity and discovery potential in a short time scale. Also, experiments start getting limited by the availability of required materials, such as xenon or enriched germanium.

This raises the question weather a simultaneous search with different physics channels is feasible. Regarding the possible target materials, xenon seems to be a very convenient choice. Firstly, because the currently most sensitive dark matter experiments use liquid xenon as a target material, secondly because xenon naturally contains ^{136}Xe which is used by some of the most sensitive $0\nu\beta\beta$-experiments, and thirdly because the high density and atomic number enhance the neutrino scattering rate. However, despite the advantage of pooling forces and resources, such an experiment faces new challenges. For example, the level of enrichment in ^{136}Xe has to be carefully balanced to perform competitive measurements in $0\nu\beta\beta$- and dark matter searches simultaneously, because the $2\nu\beta\beta$ background could hide a possible dark matter signal. Also, the background has to be reduced in a wide energy range, and the signal has to be read out with high efficiency and resolution in the entire region of interest from vew keV to several MeV.

DARWIN, a next generation dark matter experiment, will try to overcome these challenges and profit from the advantages of a simultaneous search. The project is described in detail in the next chapter.

2 The DARWIN Project and Its Vertical Demonstrator

DARWIN is a proposed next-generation experiment that emerged from the experience gained from the XENON experiments, with the idea of building the ultimate dark matter detector. The detector will be a dual-phase xenon time projection chamber (TPC) with improved sensitivity to WIMP searches compared to the currently running XENONnT experiment. Thanks to its target mass of 40 t, DARWIN will also have high sensitivity to the $0\nu\beta\beta$-decay of ^{136}Xe and to low energy solar neutrinos. The design and construction of such a large detector poses huge challenges that require careful preparation. Parts of the required technologies will be tested by an R&D project located at the University of Zurich, called Xenoscope.
This chapter starts by explaining the working principle and benefits of TPCs filled with liquid xenon. Then, the DARWIN experiment is described in detail. The chapter ends by explaining the purpose and setup of the DARWIN Vertical Demonstrator.

2.1 Dual-Phase Xenon Time Projection Chambers

The use of a dual-phase TPC for WIMP detection was originally proposed by Barabash and Bolozdynya in 1989 [87]. Xenon TPCs were then pioneered in the early 2000s with the ZEPLIN I [88] and XENON10 [89] experiments. Today, three different collaborations (XENON, LUX-ZEPLIN, and Panda-X) are employing and refining this detection technique with the main goal of directly measuring WIMP dark matter. At the moment, they hold the best exclusion limits in this discipline.
In this section, the working principle of a dual-phase xenon TPC and its components will be explained in detail.

2.1.1 Xenon as a Detector Medium

Xenon is widely used in low background experiments. It is the heaviest non-radioactive noble gas, with a high mass number ($A = 131$), enhancing the spin-independent WIMP-nucleon cross section, proportional to A^2. It has a natural abundance of 87 ppb in the Earth's atmosphere and can be found naturally as nine different isotopes, two of which, ^{124}Xe and ^{136}Xe, are radioactive. While ^{124}Xe is very rare, ^{136}Xe has an abundance of almost 9 % and a half-life of 2.17×10^{21} years [90]. ^{136}Xe undergoes $2\nu\beta\beta$-decay and can be used in the search for $0\nu\beta\beta$-decay. The ^{129}Xe and ^{131}Xe isotopes can be used to probe spin-dependent WIMP-nucleon interactions, due to their non-zero nuclear spin of 1/2 and 3/2 respectively. Further, liquid xenon has a high density of 2.86 g/cm^3 at 177 K [91] which allows for building compact detectors with efficient self-shielding against penetrating background radiation from outside.

Besides these well-suited attributes, xenon is mainly used in astroparticle physics detectors due to its excellent scintillation and ionization properties, which allow for discrimination between nuclear- and electronic recoil events.

When a particle interacts in liquid xenon, the deposited energy is shared between ionization, excitation of xenon atoms and heat. While the heat deposition can not be detected, ionized (Xe^+) and excited (Xe^*) states produce light in the detector through the following processes: (Xe^+) forms a bound state (diatomic molecule) with another xenon atom. This molecule can recombine with a free electron, causing it to split up, releasing heat, and forming an excited state. The full process can be written as

$$\mathrm{Xe}^+ + \mathrm{Xe} \rightarrow \mathrm{Xe}_2^+, \tag{2.1}$$

$$\mathrm{Xe}_2^+ + \mathrm{e}^- \rightarrow \mathrm{Xe}^{**} + \mathrm{Xe}, \tag{2.2}$$

$$\mathrm{Xe}^{**} \rightarrow \mathrm{Xe}^* + \mathrm{heat}. \tag{2.3}$$

The excited Xe^* state (exciton), which can also be produced directly, again forms a diatomic molecule (excimer). In the de-excitation process, this molecule releases a characteristic xenon scintillation photon of 178 nm wavelength (VUV light). This process can be written as

$$\mathrm{Xe}^* + \mathrm{Xe} \rightarrow \mathrm{Xe}_2^*, \tag{2.4}$$

$$\mathrm{Xe}_2^* \rightarrow 2\mathrm{Xe} + \mathrm{h}\nu. \tag{2.5}$$

The number of produced scintillation photons, N_{ph}, is therefore

$$N_{ph} = a \cdot N_{ex} + b \cdot r \cdot N_i, \tag{2.6}$$

where N_{ex} and N_i are the number of excited and ionized xenon atoms, r is the fraction of ionized atoms that recombine, and a and b are the photon production efficiencies, assumed to be $a \simeq b \simeq 1$. It directly follows that the number of produced electrons is

$$N_{e^-} = (1 - r) \cdot N_i. \tag{2.7}$$

Due to differing ionization processes, the ratio between N_{ph} and N_{e^-} is different for nuclear- and electronic recoil events. More precisely,

$$\left(\frac{N_{e^-}}{N_{ph}}\right)_{ER} > \left(\frac{N_{e^-}}{N_{ph}}\right)_{NR}, \tag{2.8}$$

which allows for background reduction through specific event selection [92].

2.1.2 Working Principle

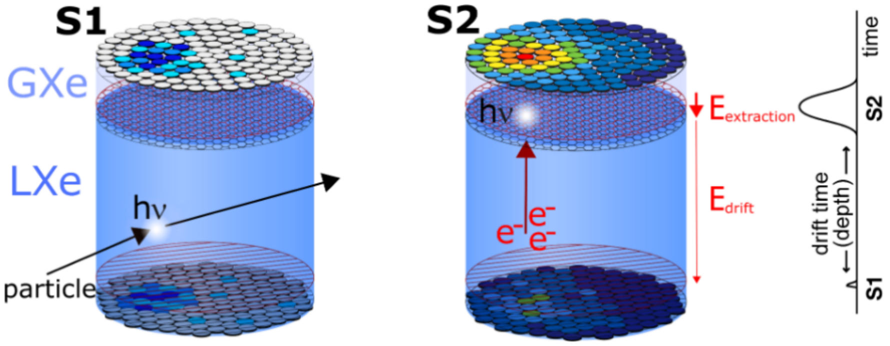

Figure 11: Illustration of the working principle of a dual-phase xenon TPC. LXe stands for liquid xenon, while GXe stands for gaseous xenon. Figure adapted from [93].

A dual-phase TPC consists of a large volume of liquid noble gas such as argon or xenon, with a small gas phase on top. As shown in figure 6, dual-phase TPCs can detect the energy deposited as charge and light while the heat is not accessible. This is done by viewing the detector volume with photosensors. The scintillation process, depicted above for the case of xenon, produces a prompt scintillation light signal, called S1, that can be directly measured. Simultaneously, the electrons produced in the ionization process are accelerated towards the gas phase in a uniform electric drift field. On top, the electrons get extracted from the liquid by a second, stronger field. The accelerated electrons then produce an amplified electro-luminescence signal proportional to the charge in the gas phase, called S2. The whole working principle of a dual-phase xenon TPC is illustrated in figure 11.
One of the main advantages of a dual-phase TPC is the three-dimensional position reconstruction. The x- and y position can be deduced from the light hit pattern of the S2 signal in the photosensors on top, because the electrons drift vertically upwards. The z position can be calculated from the time delay of the S2 signal with respect to the S1 signal knowing the electron drift velocity. This allows for selecting a fiducial volume in the middle of the detector, making use of the xenon self-shielding, and cutting away events from regions with enhanced background near the walls of the detector. In addition, the ratio between the measured S1 and S2 signal is proportional to the ratio between produced photons and electrons in an event, since

$$N_{ph} = \mathrm{S1}/g_1, \quad \text{and} \quad N_{e^-} = \mathrm{S2}/g_2, \tag{2.9}$$

where g_1 and g_2 are detector parameters called photon detection efficiency and charge amplification factor respectively. Therefore, similar to equation 2.8, the ratio between S2 and S1 signal allows discriminating very efficiently between nuclear- and electronic recoil events.

2.1.3 General Setup

In order to operate a dual-phase TPC, several components are required that need to work together. The exact design of them of course depends on the particular experiment. In the following subsections, however, a more general overview of the most important subsystems will be given.

Cryostat

Optimal detector conditions for a dual-phase xenon TPC are reached at a temperature of roughly 177 K (−96 °C) and a pressure around 2 bar. These conditions are reached by placing the TPC in a pressure-tight double-walled cryostat with vacuum insulation. The cooling power can be provided by liquid nitrogen or by a pulse tube refrigerator, while the temperature is fine-adjusted using a heater. Usually, the cryostat has a cylindrical shape and is made out of steel.

Photosensors

Photosensors are the eyes of a detector and are crucial for the light-signal readout. Usually, they are placed at the top and bottom of the TPC. Current experiments, like XENONnT and LZ, use photomultiplier tube (PMT) arrays for this purpose. PMTs are widely used in physics for light detection, also in other fields. The principle was invented already in 1936 [94] and has been optimized over many years for the use in xenon TPCs. PMTs relay on the photoelectric effect to transform light into a charge signal. If a photon enters trough the transparent window into the evacuated PMT, it first falls onto a photocathode where a photoelectron (PE) is released. The PE is then accelerated through a focusing electrode onto an electron multiplier dynode, where more electrons are produced. These secondary electrons are then consecutively amplified in several dynode stages until a shower of electrons falls onto the anode. Here the charge signal, proportional to the number of initial photons, is read out. A schematic of the PMT working principle can be seen in figure 12.

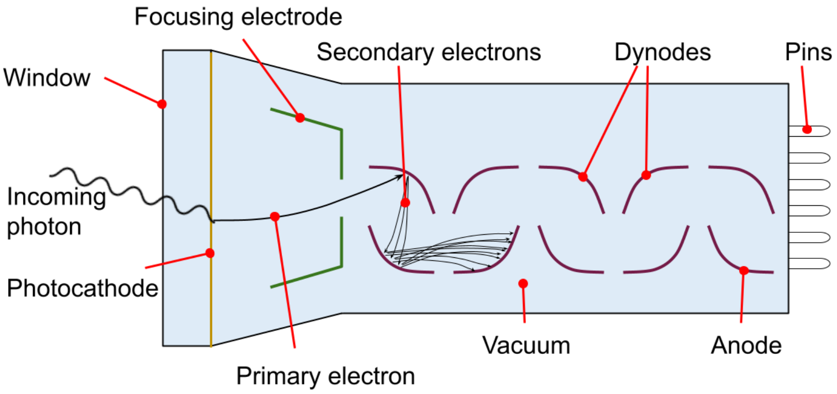

Figure 12: Schematic of the working principle of a PMT.

PMTs have the advantage of a good light detection efficiency for xenon scintillation light (around 20 %) along with a low dark count rate at liquid xenon temperature (about 0.01 Hz/mm^2) [95]. However, they are expensive, somewhat bulky, and account for a significant fraction of the radioactive background.

In the last years, another type of photosensor has moved into focus. Silicon photomultipliers (SiPMs) are newer devices, used for the first time in a dual-phase xenon TPC in 2020 in the Xurich-II experiment [96]. SiPMs are based on semiconductor technology and consist of $\mathcal{O}(10^5)$ microcells. Every cell contains an n-doped region above a p-doped region on a silicon substrate. If a photon hits a microcell, an avalanche of $10^5 - 10^6$ electrons is released. The cells operate in Geiger-mode, meaning that the produced charge is summed up in the read-out electronics. A schematic of the SiPM working principle can be seen in figure 13. As long as every microcell is hit by only one photon, the produced signal is proportional to the number of initial photons. Above this threshold, SiPMs lose their linearity. SiPMs also have a good VUV light detection efficiency similar to PMTs [97]. Their main advantage is the small size that allows for good position reconstruction and low radioactivity. However, despite improvements in the last years, their high dark count rate (about 1 Hz/mm^2) and crosstalk probability at the relevant temperature for a xenon TPC are still a problem [98, 96].

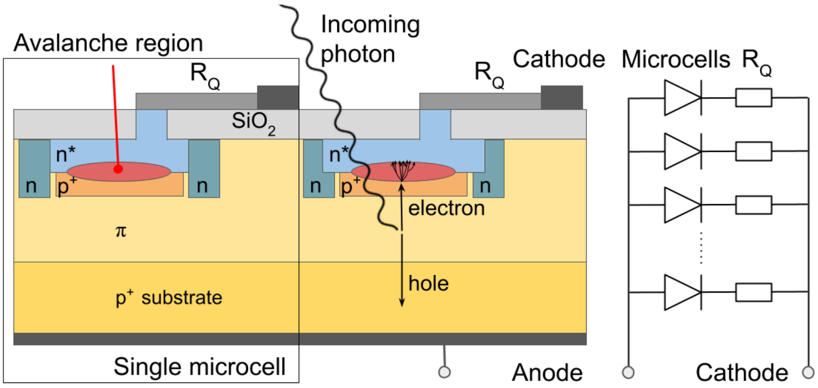

Figure 13: Schematic of the working principle of a SiPM.

Field Cage

In order to drift the electrons up and to extract them into the gas phase, two electric fields have to be established in the TPC. This is done with a field cage that is immersed in the liquid xenon inside the cryostat. It mainly consists of a sequence of concentric copper rings held by pillars which create its cage-like appearance, as well as three electrodes: cathode, gate, and anode. To keep the TPC transparent to light as much as possible on top and bottom, the electrodes are three meshes on which individual voltages are applied. The cathode mesh is located at the bottom, right above the photosensors. It operates at a negative voltage to repulse the electrons. The gate mesh, usually operating around ground, is placed in the liquid xenon directly below the gas phase. To keep the drift field, E_{drift}, between cathode and gate uniform throughout the whole liquid xenon volume, regularly spaced copper field shaping rings with a constant voltage gradient surround the drift region. Finally, the anode mesh is located in the gas phase on top, right below the photosensors. It operates at a positive voltage to attract the electrons. The electric field on top, $E_{extraction}$, needs to be stronger than the drift field to extract the electrons into the gas phase such that an amplified S2 signal can be seen. To assure the homogeneity of $E_{extraction}$, the liquid xenon level between gate and anode is continuously monitored by several level meters. The electric fields and meshes are sketched in figure 11.

Gas System

Xenon TPCs feature an elaborate gas system for various purposes. First of all, it is needed for filling and recuperating the TPC. In addition, during a science run, the gas system is used to continuously purify the xenon. The xenon in a TPC needs to be extremely pure for several reasons. On one hand, electronegative impurities, such as oxygen, can absorb the drifting electrons resulting in a reduced charge readout (S2 signal), especially for events located in the bottom region. On the other hand, water impurities are expected to reduce the light production efficiency as found in liquid argon [99, 100] and radioactive impurities contribute to the internal background. Usually, the impurities get filtered out of the xenon by a hot metal getter placed in the gas flow. Recent experiments started to additionally use a liquid purification system that is capable of quickly cleaning larger amounts of xenon [101]. Apart from that, the gas system can be used to introduce internal calibration sources into the detector. More about this can be found in the section 4.4.1.

2.1.4 Coping With Backgrounds

In a TPC, different particle interactions can mask potential dark matter signals or neutrino interactions. These background events have to be suppressed to reach the best possible sensitivity. In order to do so, different backgrounds have to be addressed separately with targeted measures. For that purpose, first, the main background sources have to be identified. In general, they can be divided into two groups, radiogenic and cosmogenic backgrounds.

Radiogenic Background

One part of the background is due to radioactive α-, β-, and γ-decays in the vicinity of the detector and is hence called radiogenic background. Its origin and characteristics are described in detail in section 3.1. In general, this background is reduced by carefully selecting materials with low radioactivity for the detector components. However, perfectly radiopure materials do not exist. Therefore, different techniques are employed to further reduce this background. Electrons and photons (β- and γ-rays) can be distinguished from the expected WIMP signal because they produce electron recoil events in contrast to the searched nuclear recoils. They can hence be eliminated in the data analysis using the fraction of S1- to S2-signal. For the α particles, the situation is a bit more complicated. In liquid xenon, they have a very short absorption length. Thus, if an α-decay takes place in the detector walls or even outside the detector it can be avoided by fiducializing the volume, meaning that only events in the shielded center of the detector are considered. This also helps to further reduce β- and γ-events originating from the walls. However, if an α-decay takes place inside the liquid xenon itself, a fiducial volume cut does not help. Therefore, the liquid xenon is cleaned before and during detector operation. Apart from that, α-decays can produce neutrons in so-called (α,n) reactions. Neutrons are particularly unwanted in a TPC because they produce nuclear recoil events very similar to the expected WIMP signal. They have, however, a relatively short mean free path of $\mathcal{O}(10\,\mathrm{cm})$ in liquid xenon [102] and hence most often scatter multiple times in big detectors. Most neutron events can thus be rejected in the data analysis by demanding single scattering events as expected for WIMPs. The remaining background, caused by single scattering neutrons that escape the detector after the first interaction, can be further reduced by an active neutron-veto surrounding the detector.

Cosmogenic Background

The other part of the background in a TPC is of cosmic origin and is therefore called cosmogenic background. The majority of it are muons that are produced in the collision of high-energy cosmic rays in the Earth's atmosphere. These muons typically have a high energy of $\mathcal{O}(1\,\mathrm{GeV})$ at the surface of the Earth [103]. This is way above the expected WIMP signals, but if the muons interact near or inside the detector, they can produce other lower energetic particles like neutrons or kaons. To reduce the muon-induced neutron background, rare event searches are conducted in underground facilities like LNGS [104], SNOlab [105] and many others [106]. This drastically reduces the muon flux [107], as for example at LNGS by a factor of 10^6, while shifting their energy distribution to higher energies [103]. Moreover, experiments are often placed in big water tanks featuring an active Cherenkov veto in order to tag the muons and to stop neutrons that are produced in the rock. Apart from muons, also neutrinos and γ-rays are part of the cosmogenic background. In contrast to muons, neutrinos can not be avoided by placing the detector underground because of their low interaction cross section. The neutrino background, sometimes called neutrino floor or fog, therefore puts an unavoidable sensitivity limit for WIMP dark matter searches, shown in figure 7 [108]. On the other hand, neutrinos themselves are an interesting physics channel.

Background Model

Even with all these measures, it is not possible to reduce the background to zero. To still be able to find a hidden signal, a detailed background model has to be developed. For the radiogenic part, this is done by first screening the materials of the detector components and the lab environment. Then Monte Carlo simulations based on physics models are performed to see how this background will propagate into the detector. Similar simulations are done to determine the cosmogenic background. Here, the simulations have to rely on measurements of the muon flux from other experiments as input parameters.

2.2 DARWIN

DARWIN (**DAR**k matter **WI**mp search with liquid xeno**N**) is a proposed next-generation experiment that will primarily be built to reach unprecedented sensitivity to WIMP dark matter above 5 GeV/c^2. In this region, it will probe the spin-independent WIMP-nucleon interactions down to the neutrino fog and increase the current best limit of XENON1T by two-, and the expected sensitivity from XENONnT and LZ by one order of magnitude. The best sensitivity will be reached around 40 GeV/c^2 ($\mathcal{O}(10^{-49}$ cm^2)) [4]. In addition, the DARWIN detector will have other promising physics channels. Due to the amount of ^{136}Xe contained in the TPC (about 3.6 t), DARWIN will have excellent sensitive to the $0\nu\beta\beta$-decay of ^{136}Xe and probe the effective Majorana mass in the range of $\langle m_{ee} \rangle$ = 18-46 meV [109]. Likewise, because of the contained ^{129}Xe it will have high sensitivity to spin-dependent WIMP-nucleon scattering and axial-vector couplings. Finally, DARWIN will also reach excellent sensitivity to solar axions and axion-like particles, and measure super nova- and solar neutrinos with high accuracy [4, 110].

2.2.1 Baseline Design

These goals will be accomplished by increasing the detector's total mass to 50 t (40 t active target) of liquid xenon and reaching an unprecedented low background level. To contain this mass, the DARWIN TPC will have a cylindrical shape of ~2.6 m diameter and height, placed in a double-walled cryostat. Two types of photosensors, PMTs and SiPMs, are considered for the light readout in the top and bottom arrays. Also a combination of the two, for example PMTs at the bottom and SiPMs on top, is possible. The external background will automatically be reduced in such a big detector because of the xenon self-shielding. However, the internal background is still a problem that needs to be addressed. This will be done by continuously removing radioactive Kr and Rn isotopes from the xenon in distillation columns [111] as already done in XENONnT and with a fast xenon purification system. To cope with cosmogenic neutron background, the detector will be placed in an underground facility, probably LNGS, and surrounded by a neutron-veto and a water shield featuring an active Cherenkov veto [4].

2.2.2 Challenges

For building such a large dual-phase xenon TPC, it is not enough to just scale up the current operating detectors. Several new challenges arise for DARWIN that need to be studied, including:

- Generation of a uniform drift field of about 200 V/cm over 2.6 m, requiring very high voltages and rigid meshes with good transparency.
- Efficient large-scale xenon purification system, to assure a long electron lifetime of at least 2 ms and to reduce the internal background. XENONnT already reached an electron lifetime of 7 ms but for a smaller amount of liquid xenon [112].

- Photosensor arrays covering a large area with high light detection efficiency, good position reconstruction, low dark count and crosstalk rates, and low intrinsic background.
- Upscaling of the cryostat and TPC with high stability while keeping low radioactivity levels.

These challenges are addressed in the DARWIN R&D program, for which two prototypes have been built. One of them, a flat detector with the full diameter of DARWIN, called Pancake, was constructed at the University of Freiburg. The other one, a Vertical Demonstrator with DARWIN's full 2.6 m height, called Xenoscope, has been designed and built at the University of Zurich. This detector is the main topic of this work.

2.3 The DARWIN Vertical Demonstrator

The main purpose of the DARWIN Vertical Demonstrator, Xenoscope, is to prove that drifting electrons in liquid xenon over a distance of 2.6 m is possible, which has to be shown before DARWIN is built. It would be the first time to drift electrons over such a long distance in liquid xenon. As already mentioned, this requires highly pure xenon and a uniform vertical drift field. Therefore, also an efficient xenon purification system and a high voltage distribution will be tested. Apart from that, a top array of SiPMs will be installed to examine their performance at cryogenic conditions. After completing its mission, Xenoscope will be available to test other detector components that could be used in DARWIN and to conduct complementary experiments in liquid xenon. For example optical properties of the LXe, such as the Rayleigh scattering length and refraction index, and electron diffusion are planned to being measured [5].

2.3.1 Setup

The DARWIN Vertical Demonstrator was constructed in the high-bay area of the assembly hall of the Department of Physics at the University of Zurich. In this room, a $4\times4\times4\,\mathrm{m}^3$ support structure was built up from aluminum profiles. It consists of three parts, the *inner frame* holding the weight of the xenon-filled cryostat and TPC, the *outer frame* providing lateral support and holding the floor of the top level, and the *stairs* providing access to the top level. The outer frame is closed off by acrylic windows to minimize dust accumulation and can be entered through a door on the front side. Within the outer frame, the *power distribution cabinet* of the high voltage system is placed. It can provide voltages up to 100 kV and is therefore coupled to a multilayer safety system.

The TPC will be placed in the middle of the setup in a pressure-tight double-walled *cryostat* with vacuum insulation. The inner part of the cryostat consists of five tubular sections of 24.8 cm inner diameter and a conical section on top to make more room for the instrumentation, the photosensor array and cables. It can hold a maximum amount of 400 kg of liquid xenon with a targeted amount of 390 kg during operation, and is fully enclosed by the outer cryostat. The top flanges of the inner and outer cryostat are one connected piece. On top,

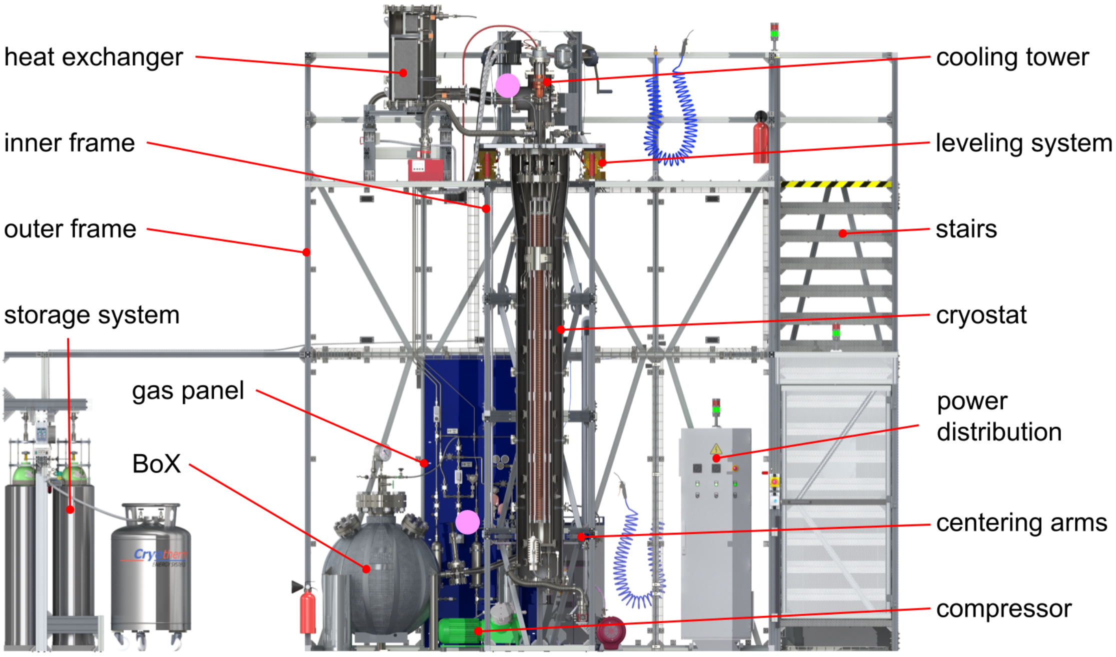

Figure 14: Render of the complete Xenoscope assembly. The important subsystems, written in italic in the text, are marked in the figure. Additionally, the positions of the conducted background measurements, described in the next chapter, are marked by the pink filled circles. Figure adapted from [5].

it is bolted to a triangular plate sitting on the *leveling system* that allows to accurately align the TPC vertically. Additionally, the base of the outer cryostat is held in place from outside by four locked centering arms. On top of the cryostat sits the *cooling tower* in which the gaseous xenon, returning from the gas system, is continuously liquefied on a copper cold head. To reduce energy consumption during operation, the returning gas is precooled in a *heat exchanger* using the cold outgoing gas before entering the cooling tower.
The gas system can be used for filling the cryostat with xenon from the *storage system* and recuperating it back. The storage system is designed for ten 40 l gas cylinders for longtime storage under high pressure. Filling and recuperating can be achieved by cryopumping. For this, the liquid xenon is heated and thus evaporates on one side, while the other volume is cooled such that the xenon gas is recovered in it. For quicker recuperation, an additional liquid recovery system was constructed. Its centerpiece, *BoX* (Ball of Xenon), is a spherical pressure vessel into which the liquid xenon can flow directly from the cryostat by gravity.
During operation, the gas system, mounted on the *gas panel*, allows for efficient cleaning of the xenon. For this, the xenon gas is pumped into the purification cycle by a *compressor* after leaving the heat exchanger. There, electronegative impurities get filtered out of the gaseous xenon by a hot metal getter. Afterwards, the xenon flows back to the heat exchanger and reenters the cryostat [5]. A render of the full setup in which the important subsystems are marked can be seen in figure 14. A picture of the completed Xenoscope detector can be found in the appendix in figure 60.

2.3.2 Purity Monitor and TPC

Xenoscope will pursue its goal of measuring electrons drift over 2.6 m in three stages. In the first phase, a purity monitor (PM), fully immersed in liquid xenon, will measure electrons drifting over 525 mm. This will give a first estimate of the achievable electron lifetime and xenon purity. In the second stage, the PM will be upgraded to a fully functioning 1 m dual-phase TPC, by adding the light readout and gas-phase on top. In the third phase, the Demonstrator will finally reach its full height of 2.6 m. This will require an additional high voltage feed-through at the bottom allowing for a cathode voltage of −50 kV. A render of the TPC setup in which the important components are marked can be seen in figure 15.

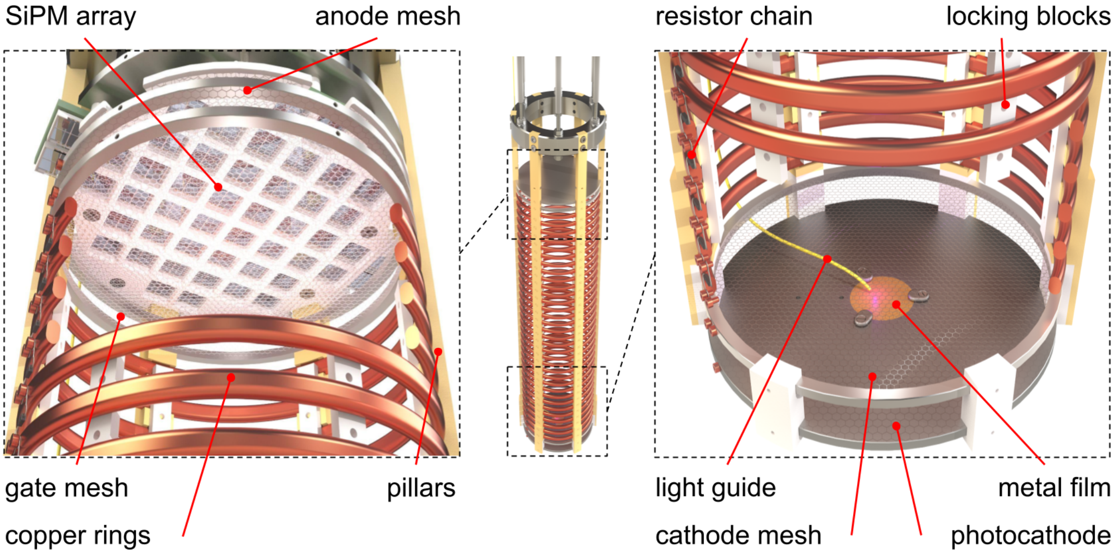

Figure 15: Render of the top (left) and bottom (right) section of the TPC with the SiPM array. For the PM, the anode mesh is replaced with a solid disk as the one of the photocathode. The important components, written in italic in the text, are marked in the figure. Figure adapted from [5].

The PM will measure the electron lifetime using four parallel electrodes. The *photocathode*, placed at the bottom, consists of a quartz substrate coated with a thin *metal film* in the middle. A xenon flash lamp is pointing at its center via an *optical fiber* to produce photoelectrons through the photoelectric effect. On top of the setup, where usually the *anode mesh* sits, a similar disk is placed, but without a flash lamp. In between, two meshes are installed in order to apply the required voltages for the drift field. One of them (*cathode mesh* of the TPC) is mounted just above to the photocathode, the other one (*gate mesh* of the TPC) sits just below the anode disk. The two meshes create an intermediate 525 mm electron drift region that is surrounded by copper *field shaping rings* of 15 cm inner diameter. The copper rings are held in place by six polyamide-imide (torlon) *pillars* and *locking blocks*.

The linear potential drop between the rings, required for the uniformity of the field, is provided by a *chain of resistors*. The electron lifetime, and thus the xenon purity, is measured via electromagnetic induction: The induced current, produced by the drifting electrons, is measured at the bottom between the photocathode and lower mesh and on top between upper mesh and anode. The ratio of the two induced currents is proportional to the fraction of electrons that reach the top and can therefore be used to calculate the electron lifetime and xenon purity.

For the TPC, the drift region will be extended by adding another section of copper field shaping rings for the second stage, and then three more sections for the final stage. In the fully assembled TPC, 172 copper rings will cover the total height of 2.6 m. Additionally, the disk on top will be replaced by the *anode mesh*. The liquid level will be lowered to a level between the gate and anode mesh and monitored by several level meters. Above the anode, an array of 48 Hamamatsu S13371 $12 \times 12\mathrm{mm}^2$ *SiPMs* will be installed to measure the produced S2 signal from the extracted electrons on top. The high dark count rate of the SiPMs is not an issue for Xenoscope because data acquisition will be triggered externally based on the pulsing of the flashlight [5].

3 Background Measurements

The characterization of the expected background is crucial for the calibration of a detector as well as later for the measurements to be conducted, especially in rare event searches. The main background components for a dual-phase TPC have been described in section 2.1.4. Since Xenoscope is neither placed underground nor shielded against radiation, the background level will be very high and therefore needs to be carefully studied.
This work addresses the radiogenic background in the DARWIN Vertical Demonstrator. However, the simulation of the background originating from all the detector components, as described in section 2.1.4, was not possible for this R&D project since not all materials in and around the assembly hall have been screened. Therefore, a different approach was chosen. Because the detector is not shielded, it was assumed that the main radiogenic background comes from the concrete walls of the lab and hits Xenoscope from outside. Using a thallium doped sodium iodide (NaI(Tl)) detector, high-energy photons in the keV to MeV range (γ-rays) from this background were measured in the lab. Knowing the detection efficiency curve of the NaI(Tl) detector and the branching ratios of the investigated decay channels, the activities of the most important background components were calculated. In a second step, described in chapter 4, a Geant4 Monte Carlo simulation was performed to determine the fraction of radiation that makes its way through the steel walls of the detector and deposits energy in the liquid xenon inside the TPC. It has to be noted that also the cosmogenic background will be of great importance for the experiment, especially at high energy from atmospheric muons. Therefore, an independent study of this background is ongoing, but it is not subject of this thesis.
This chapter starts by introducing the basics of radioactivity and radiogenic backgrounds. Then, the working principle of the NaI(Tl) detector is explained. In section three, the test run is described with which the best operating voltage for the NaI(Tl) detector was determined. Afterwards, the actual background run and the data analysis are explained. The chapter concludes with the results of the measurements.

3.1 Basics of Radioactive Decays and Radiogenic Background

Out of more than 3000 known nuclides, only 257 are stable. All others will decay sooner or later by emitting some kind of radiation. There are different mechanisms behind the different kinds of decays but they all have in common that the probability of a single atom to decay remains constant over time. Therefore, the number of radioactive atoms of a certain kind in a given sample decreases exponentially over time:

$$N(t) = N_0 \cdot e^{-\lambda t}. \tag{3.1}$$

Here, N_0 is the initial number of atoms and λ is the decay constant. It directly follows that also the decay rate R shows the same behaviour:

$$R(t) = -\frac{dN(t)}{dt} = \lambda \cdot N_0 \cdot e^{-\lambda t} = R_0 \cdot e^{-\lambda t}, \tag{3.2}$$

where now R_0 is the initial decay rate. One can easily see that the whole decay is dictated by one parameter, λ. This decay constant is linked to the mean lifetime τ and the half-life $t_{1/2}$ by the relations

$$\tau = \frac{1}{\lambda} \quad \text{and} \quad t_{1/2} = \frac{ln(2)}{\lambda}, \tag{3.3}$$

where τ is defined as the average lifetime of all the atoms in a sample and $t_{1/2}$ is the time after which half of the atoms of a sample have decayed away [59].

3.1.1 α-Decays

In an α-decay, the nucleus of the parent atom emits an α-particle which is nothing else than the nucleus of a helium atom ${}^4_2$He. Therefore, the number of neutrons N and protons Z both decrease by 2 while the number of nucleons A decreases by 4. A generic α-decay can hence be written as

$${}^A_Z X \longrightarrow {}^{A-4}_{Z-2} Y + \alpha. \tag{3.4}$$

Because of energetic reasons such decays can only happen if the mass of the radioactive parent nucleus is greater than the sum of the masses of the decay products. Using Einstein's mass-energy equivalence, the total released energy Q (Q-value) can be written as

$$Q = \Big(m({}^A_Z X) - m({}^{A-4}_{Z-2} Y) - m(\alpha) \Big) \cdot c^2, \tag{3.5}$$

where c is the speed of light and the electron mass is neglected because it is much smaller than the mass of the α-particle and the other nuclei. Since the mass of a generic nucleus is

$$m({}^A_Z X) = Zm_p + (A-Z)m_n - \frac{E_B({}^A_Z X)}{c^2}, \tag{3.6}$$

with proton mass m_p, neutron mass m_n, and binding energy E_B, Q can also be written as

$$Q = E_B({}^{A-4}_{Z-2} Y) + E_B(\alpha) - E_B({}^A_Z X). \tag{3.7}$$

The binding energy can be calculated using the semi empirical liquid drop model [113]:

$$\begin{gathered} E_B({}^A_Z X) = a_v A - a_s A^{2/3} - a_c \frac{Z^2}{A^{1/3}} - a_a \frac{(N-Z)^2}{A} + \delta(Z,A), \\ \text{where} \;\; \delta(Z,A) = \begin{cases} +a_p A^{-1/2} & \text{for A even Z, N even} \\ -a_p A^{-1/2} & \text{for A even Z, N odd} \\ 0 & \text{for A odd} \end{cases} \end{gathered} \tag{3.8}$$

Here, all parameters a_i are experimentally determined, $\delta(Z, A)$ is called the pairing energy term. It can be seen that the binding energy decreases for large nuclei, therefore all very heavy nuclei ($Z > 82$) are theoretically unstable to α-decays. However, the α particle only carries the whole decay energy Q for transitions directly to the ground state of the daughter nucleus. The energy spectrum of α-particles emitted by heavy nuclei therefore show several sharp peaks with energies smaller than Q as can be seen in figure 16. The rest of the energy is emitted as a γ-ray during the deexcitation of the daughter nucleus.

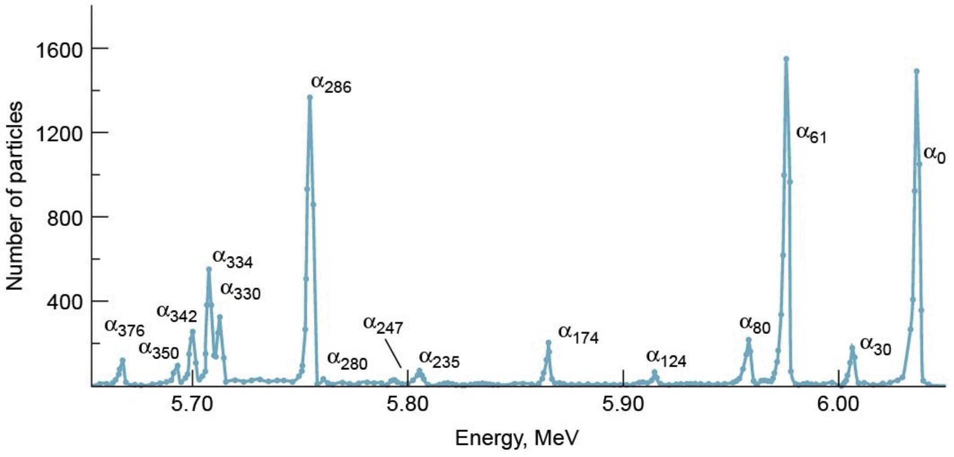

Figure 16: α-particle energy spectrum from ^{227}Th decay. The highest energy α-particle corresponds to a decay directly into the ground state of ^{223}Ra with $Q = 6.04$ MeV. Figure from [59].

Already in 1911 an empiric relation between the maximum released energy Q and the half-life $t_{1/2}$ for α-decays was found, called the Geiger-Nuttall rule:

$$\ln(t_{1/2}) = \frac{k_1}{\sqrt{Q}} + k_2. \tag{3.9}$$

Here k_1 and k_2 are experimentally determined constants. Later, this behavior was explained by treating the α-decay as a barrier-penetration phenomenon, where the α-particle tunnels through the Coulomb potential of its parent. The higher its energy, the narrower the potential barrier through which it has to tunnel and hence the sooner a decay happens [59].

3.1.2 β-Decays

In contrast to the α-decay, in β-decays the number of nucleons A remains constant while Z and N change by ± 1. There are three decays of this kind that can be distinguished: β^--decays, β^+-decays and electron capture. From the liquid drop model, shown in equation 3.8, it can be seen that neutron-rich atoms will tend to decay by β^- emission while proton-rich atoms will tend to decay by β^+ emission or electron capture. This can also be seen in figure 17.

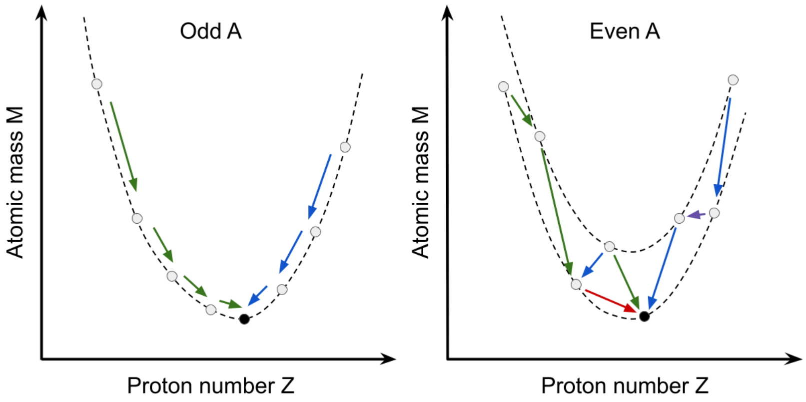

Figure 17: Masses of atoms with constant number of nucleons A plotted against Z, for A odd (left) and even (right). β^--decays are marked with green arrows, β^+- and EC-decays are marked with blue and violet arrows respectively, and double β^- decays are marked with red. It can be seen that for even A, because of the pairing energy term, there are two parabolas for Z even and uneven respectively. Because of this, only nuclei with even A and Z predominantly undergo double β-decay.

β^--Decays

In the β^--decay a neutron changes into a proton by emitting an electron and an anti-electron neutrino. This process can be written as

$$ {}^A_ZX \longrightarrow {}^A_{Z+1}Y^+ + e^- + \bar{\nu}_e. \tag{3.10}$$

Again, it can only take place if the parent atom is heavier than the daughter and the electron and neutrino together. Since neutrinos are almost massless the Q-value reads

$$Q = \Big(m({}^A_ZX) - m({}^A_{Z+1}Y^+) - m_e\Big) \cdot c^2, \tag{3.11}$$

where m_e is the electron mass and c is the speed of light. To obtain the formula in terms of a neutral daughter atom the mass of one electron has to be added because $m({}^A_{Z+1}Y^+) = m({}^A_{Z+1}Y) - m_e$. Therefore

$$Q = \Big(m({}^A_ZX) - m({}^A_{Z+1}Y)\Big) \cdot c^2. \tag{3.12}$$

β^+-Decays

The β^+-decay is pretty much the opposite of the β^--decay. A proton changes into a neutron by emitting a positron and an electron neutrino. This process can be written as

$$ {}^A_ZX \longrightarrow {}^A_{Z-1}Y^- + e^+ + \nu_e. \tag{3.13}$$

The decay energy Q reads

$$Q = \Big(m(^A_ZX) - m(^A_{Z-1}Y^-) - m_e\Big) \cdot c^2, \tag{3.14}$$

where m_e this time is the positron mass, which is the same as the electron mass. Note that here the daughter atom with nuclear charge (Z - 1) has Z electrons. To obtain the formula in terms of a neutral daughter atom the mass of another electron has to be subtracted and one arrives at

$$Q = \Big(m(^A_ZX) - m(^A_{Z-1}Y) - 2m_e\Big) \cdot c^2. \tag{3.15}$$

Thus, β^+-decays can only happen if the energy difference between the parent and daughter nucleus is at least $2m_ec^2 =$ 1.022 MeV.

Electron Capture

Electron capture (EC) is very similar to the β^+-decay but here the proton changes into a neutron by capturing an electron, usually from the innermost shell. This process is typically competing with β^+-decay. It can be written as

$$^A_ZX \longrightarrow ^A_{Z-1} Y + \nu_e. \tag{3.16}$$

and the decay energy Q simply reads

$$Q = \Big(m(^A_ZX) - m(^A_{Z-1}Y)\Big) \cdot c^2. \tag{3.17}$$

Because the captured electron leaves behind a hole in the atomic shell, EC decays are accompanied by a cascade of X-rays from electron rearrangement and Auger-Meitner electrons.

Double β-Decays

Double β-decay ($2\nu\beta\beta$) is a process in which two β^-- or β^+-decays take place at the same time. In case of β^--emission, this process can hence be written as

$$^A_ZX \longrightarrow ^A_{Z+2} Y^{2+} + 2e^- + 2\bar{\nu_e}. \tag{3.18}$$

Because simultaneous β-decays of two neutrons/protons is very unlikely, this process can only be observed in isotopes for which the usual β-decay is energetically forbidden. From the liquid drop model in equation 3.8, also shown in figure 17, it can be seen that this can only be the case for nuclei with even A and even Z.

In contrast to α-decays, in $\beta^{\pm}$-decays not all energy is given to one particle but shared between the electron/positron and anti-neutrino/neutrino. This leads to a continuous energy spectrum of the emitted electrons, where only very few have an energy near the total available energy Q as can be seen in figure 18. Historically, the fact that the energy spectrum is not discrete led to the prediction of a new particle by Wolfgang Pauli in 1930, later it was called the neutrino [59].

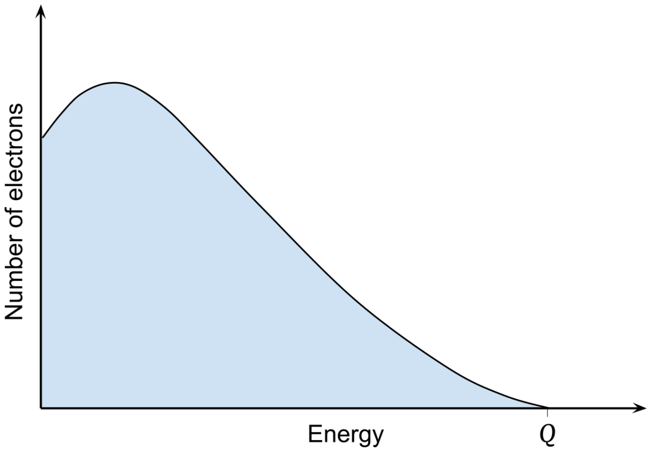

Figure 18: Schematic of the electron energy spectrum in a β-decay. If the electron does not have the total decay energy Q, the missing energy was carried away by a neutrino.

3.1.3 γ-Decays

In a γ-decay, a nucleus in an excited state decays to its ground state or another lower energy state by emission of a photon. Unlike in an α- or β-decay, the isotope does not change. It is the analog of light emission in the deexcitation of excited atoms (X-ray) but in contrast to atoms where the spacing of the energy levels is $\mathcal{O}$(eV), nuclear energy levels are $\mathcal{O}$(MeV). As in atoms, the energy levels are unique for every isotope. Because the nuclear energy levels are discrete also the γ-ray energy spectrum of a particular nucleus shows sharp peaks.

γ-decays typically follow shortly after α- or β-decays because the half-life of the excited states is very short, usually $\mathcal{O}$(ps) [114]. However, there are exceptions called metastable states that can have half-lives of the order of hours or even years. They are the consequence of quantum mechanical selection rules that forbid certain transitions based on conservation laws. An example is ^{83m}Kr, that is often used in the calibration of TPCs and has a half-life of 1.83 h [115, 59].

3.1.4 Most Important Backgrounds and Decay Chains

Natural radioactivity can originate from two kinds of radionuclides. Radionuclides of the first type were generated during the nucleosynthesis or in supernovae billions of years ago, but they did not decay yet because of their long half-life, of at least the order of the age of the Earth (about 4.5×10^9 years). All radionuclides of the second type must continually be produced in the decay of other isotopes or by different nuclear reactions.

Because in an α-decay the number of nucleons, A, changes by four while in β- and γ-decays A does not change, there are in principle four possible decay chains. All isotopes of a given chain have $A = 4n,\ (4n+1),\ (4n+2),\ \text{or}\ (4n+3)$, with $n \in \mathbb{N}$. For each chain, it is sufficient if there is one long-living radionuclide of the first kind such that the whole subsequent

chain can still be found in nature. This is clearly the case for two of the four chains, namely the ones starting at ^{232}Th and ^{238}U which have half-lifes of 1.4×10^{10} years and 4.5×10^{9} years respectively. Because after such a long time almost all other initially present isotopes of the chain with a short lifetime decayed away, the activity of the whole decay chain is dictated by the activity of the long-lived isotope. Other short lived isotopes that also lead to these chains but are not constantly produced, can be assumed to not be present anymore.
Another chain starts with ^{235}U, which has a half-life of about 7×10^{8} years. This chain can still be found on Earth but its abundance is already strongly reduced. Finally, the chain starting at ^{237}Np contains no such long-living isotope. A scheme of the two decay chains of interest for this study, ^{232}Th and ^{238}U, is displayed in figure 19.

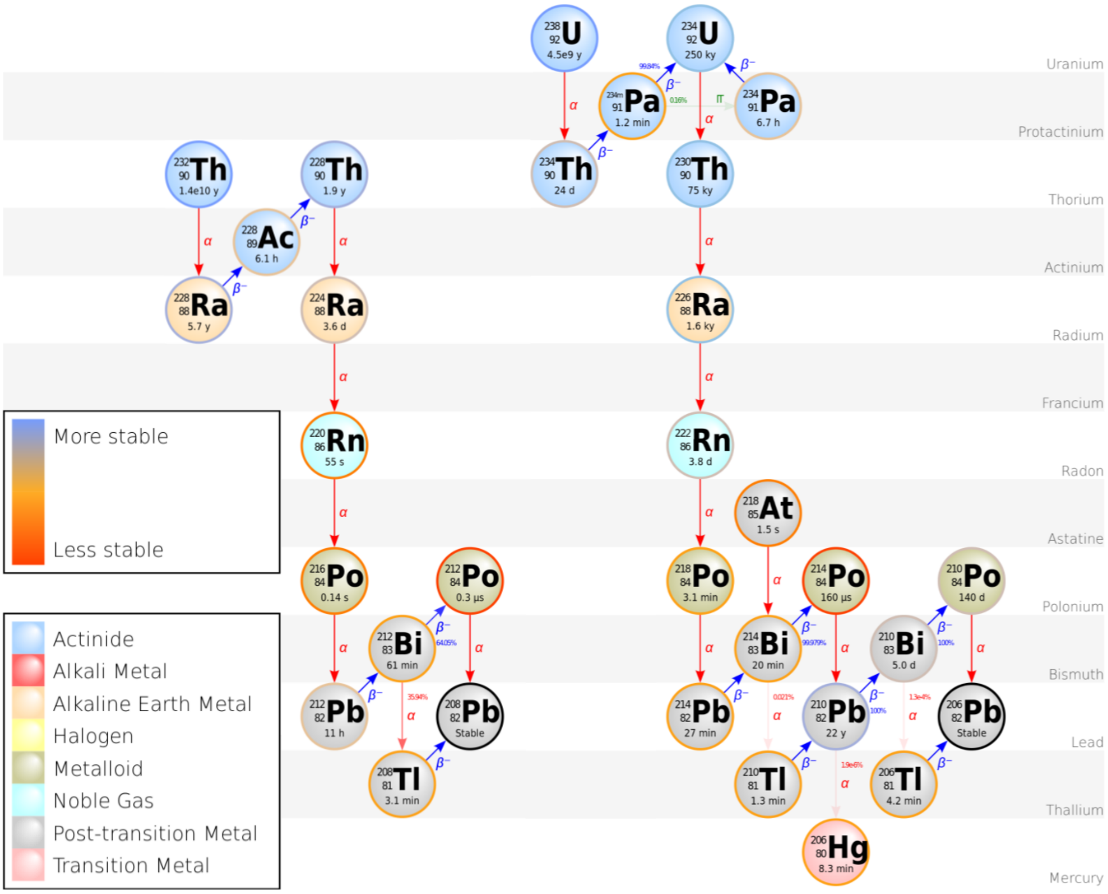

Figure 19: Schematic of the ^{232}Th (left) and ^{238}U (right) decay chains. Figure adapted from [116] and [117], the relevant numbers were crosschecked with the decay plots based on data from [115].

In principle, there could additionally be some other light isotopes that do not belong to a decay chain but are long-lived enough to be still present today. Indeed there is one such isotope with a high abundance, namely ^{40}K with a half-life of 1.2×10^{9} years. As can be seen in figure 20, ^{40}K together with the two decay chains from above give the biggest contribution to the radiogenic background on Earth. These isotopes can be found in all kinds of rocks and everything that is made out of it, as for example concrete [118].

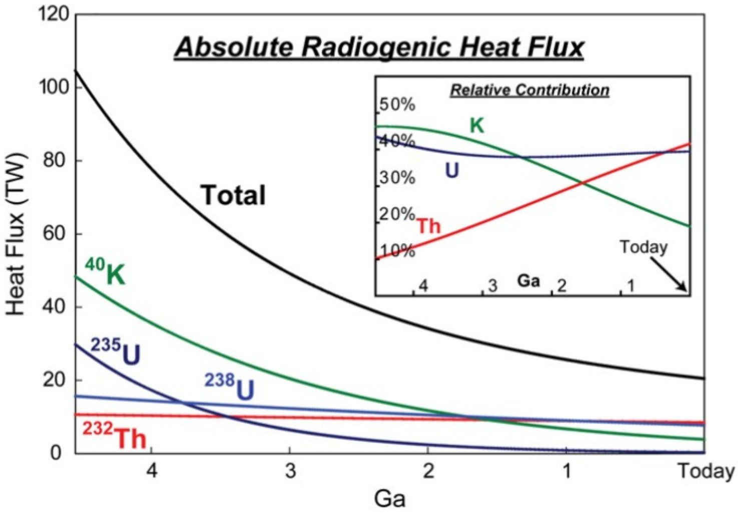

Figure 20: Erth's radiogenic heat production from its creation about 4.5×10^{9} years ago until today. At this day and age, the main contribution comes from ^{232}Th and ^{238}U. Figure from [119].

3.2 Working Principle of an NaI(Tl) Detector

For the measurement of the radiogenic background in the assembly hall where Xenoscope is located, an NaI(Tl) detector of the company Saint Gobain, model 3M3/3, was used. A picture of it can be seen in figure 21.

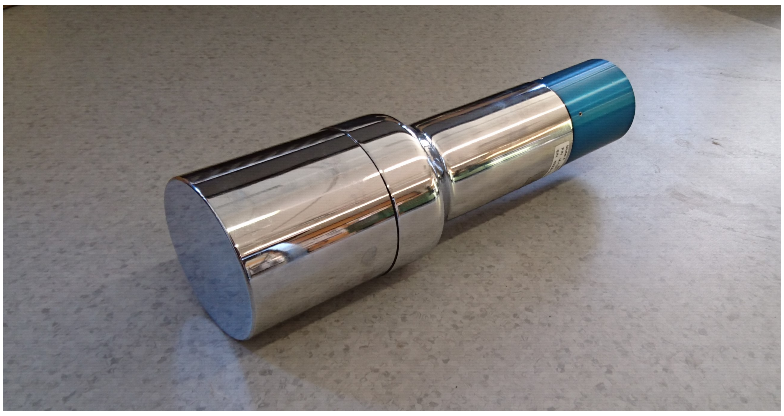

Figure 21: Picture of the NaI(Tl) detector used for the background measurements in this work. The whole detector is coated with aluminum to shield it against α- and β-radiation and to protect the NaI(Tl) crystal and PMT.

An NaI(TI) detector consists of two main building blocks, a cylindrical NaI(TI) crystal of 7.62 cm diameter and height mounted on a 3" PMT. The NaI(TI) acts as a scintillator: It produces light when a γ-ray hits it and deposits energy inside of it. The amount of light produced is proportional to the amount of deposited energy. This light travels through the crystal and some of it falls onto the photocathode of the PMT. The PMT then converts the light into a voltage signal. See section 2.1.3 and figure 12 for details about PMTs. Because of the working principle of the PMT, the voltage signal is still proportional to the amount of energy deposited in the NaI(TI) crystal. The signal is then digitized by a DAQ module and stored in root files that can be processed and analyzed.

3.2.1 γ-Ray Detection With a Scintillator

The detection of γ-rays is based on their interaction with electrons in the scintillator material. In this interaction, the photon transfers its energy to electrons, which thereon lose their energy through ionization, excitation of atoms, or Bremsstrahlung. Ideally, in the end, the whole energy of the γ-ray is transformed into visible light. One can distinguish three types of interactions of γ-rays with electrons in matter: the photoelectric effect, the Compton effect, and pair production. Each of these interactions is dominant in a different energy window as can be seen in figure 22. This section follows the book by G. Knoll [114].

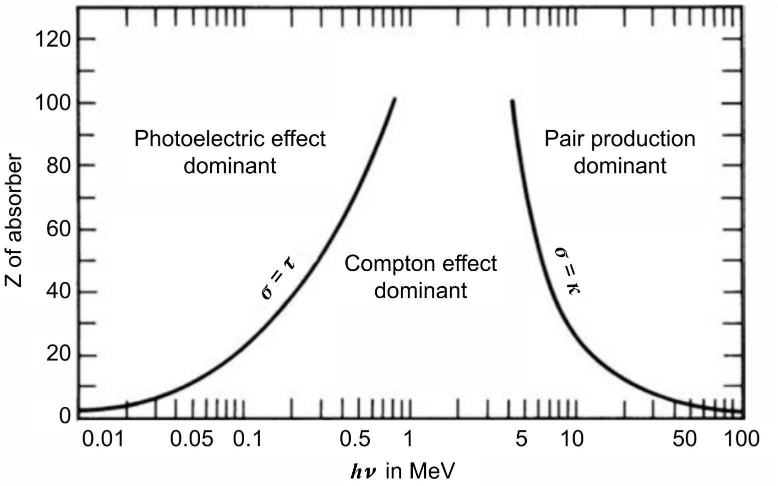

Figure 22: (a): Relative importance of the three main interaction types in a scintillator depending on the radiation energy and the atomic number Z. Figure from [114].

Photoelectric Effect and the NaI Escape Peak

The photoelectric effect is an inelastic process in which a photon is absorbed completely by an atom which releases a so-called photoelectron. This is an electron that was knocked out of one of the atomic shells and carries the γ-rays energy minus its previous binding energy. A scheme of this process can be found in figure 23 (a). If the electron originated from a

lower shell, the hole is quickly filled by electron rearrangement. In this process, the previous binding energy gets liberated in the form of characteristic X-rays (similar to nuclear γ-rays but with lower energy in the eV to keV range) or Auger electrons. The photoelectric effect is strongly enhanced for absorber materials with high atomic numbers. The probability is proportional to Z^n with n between 4 and 5 depending on the energy region.
A typical feature of spectra taken with NaI and NaI(Tl) detectors is the double peak structure of low-energy peaks. Sometimes when a γ-ray hits the NaI(Tl) crystal its energy gets absorbed by a K-shell electron of the iodine which leaves behind a hole. When this hole is then occupied by an L-shell electron, a characteristic X-ray of about 30 keV is released. Sometimes this photon escapes the crystal without getting reabsorbed. Therefore a second (smaller) peak can be found about 30 keV below the main peak at low energies. At high energies, the detector resolution is not good enough to resolve the escape peak. An example of this can be found in figure 25 (a).

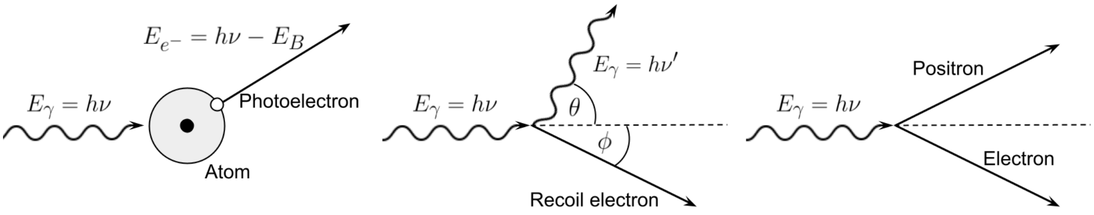

(a) (b) (c)

Figure 23: Illustrations of (a): The photoelectric effect, (b): Compton scattering, and (c): pair production. Figures inspired by [114].

Compton Scattering

In this interaction process, the γ-ray scatters elastically on a shell electron. Thereby the incoming photon gets deflected by an angle θ and transfers a fraction of its energy to the electron. A diagram of the process can be found in figure 23 (b). For small angles θ only little energy is transferred, while the maximum energy is transferred if the photon is scattered back at an angle $\theta = \pi$. Because all scattering angles are possible the electron energy distribution has a flat shape, called the Compton continuum, until at $\theta = \pi$ the maximum energy is reached, called the Compton edge. The probability of Compton scattering depends on the number of electrons available and therefore scales linearly with Z.

Pair Production

The last significant γ-ray interaction is pair production. A schematic of the process can be found in figure 23 (c). It takes place in the Coulomb field of a nucleus in the absorbing material, where an electron-positron pair is created. For this to happen, the γ-ray needs at least an energy of $2m_ec^2$ (1.022 MeV), where m_e is the electron mass and c is the speed of light. This process is most often followed by the annihilation of the positron with another electron in the absorbing medium, where they are replaced by two annihilation photons of energy $m_e c^2$ each.

Scintillation process

The scintillation process in NaI(Tl) is fundamentally different from the one in liquid xenon because the used NaI is a solid crystal. Its energy band structure features a valence band in which the electrons are bound to their atoms and a conduction band, separated from the valance band by a band gap. The energy, absorbed through one of the processes described above, can lead to the elevation of an electron into the conduction band, leaving a hole in the valence band. In a pure NaI crystal, the return of an electron into the valence band by photon emission is very inefficient. For this reason the crystal is activated (doped) with thallium, modifying the band structure and creating states in the forbidden band gap. If an electron-hole pair encounters such a modified site, the electron can deexcite back into the valance band producing a photon in the visible range around 415 nm.

3.2.2 Intrinsic Background

Every material suffers from a small amount of impurities. In an NaI(Tl) detector this can lead to an intrinsic background originating from the NaI(Tl) crystal itself and the PMT. The activity of the used detector was determined in [120] for ^{40}K and the ^{238}U and ^{232}Th decay chains. It was measured by putting the NaI(Tl) detector in a box of archaeological lead with a minimal wall thickness of 15 cm. The box was flushed with nitrogen in order to get rid of the airborne radon contamination. The lead was screened before in the germanium detector Gator [121] at LNGS. Then the rate was measured with the NaI(Tl) detector and compared to a Geant4 Monte Carlo simulation of the background originating from the lead shield itself [122]. The observed difference was attributed to the intrinsic contamination of the NaI(Tl) detector. The numbers thus determined are summarized in table 1.

Isotope	^{40}**K**	^{238}**U**	^{232}**Th**
Intrinsic activity [Bq/kg]	1.6 ± 0.3	0.25 ± 0.08	0.8 ± 0.2

Table 1: Intrinsic activity of the 3" NaI(Tl) detector which has to be subtracted from the measured values. The total weight of the detector is 2.08 kg. Values from [120].

3.3 Test Data: Processing and Operating Voltage

3.3.1 Measurement Procedure

Before measuring the radiogenic background in the lab, a series of test data-sets was taken. This was mainly done in order to determine the best operating voltage for the NaI(Tl) detector. For this purpose, the NaI(Tl) detector was shielded from external radiation using lead bricks. Then a ^{137}Cs and a ^{57}Co source were attached on the front of the detector. The energies and intensities of their main peaks can be found in table 2. Six datasets with positive operating voltages from 800 V to 1300 V were taken with a statistic of 10^5 events each. The signal of the detector was digitized using a CAEN V1730 analog to digital converter board (ADC) . For triggering an event, the threshold dependent internal trigger of the ADC was used. Further a data acquisition framework (DAQ) developed by Julian Wulf was employed [93] to store the data. It was set to save for every event a window of 10 μs length, with the peak placed in the middle, in a ROOT file.

Isotope	^{57}**Co**	^{137}**Cs**
Energy E_γ	122.1 keV	661.7 keV
Intensity I_γ [%]	85.6 ± 0.2	85.1 ± 0.2

Table 2: Energies and intensities of the γ-lines of the sources used for the determination of the best operating voltage. The energies are given without uncertainties because they are known up to at least five digits. Values from [115].

3.3.2 Processing

The goal of processing is to simplify the subsequent analysis. A convenient side effect is that the amount of storage needed for the data files is strongly reduced. This is because instead of the whole digitized waveform, after processing for each event only the relevant information like time, amplitude, position, width, and integrated area of the peaks is stored in a root file. Additionally, every event is assigned an event number. The most important information is the integral of the peak, which is proportional to the charge Q produced in the PMT and therefore also proportional to the energy of the event. This can be seen by recalling the definition of the current I and Ohm's law:

$$I = \frac{dQ}{dt} \text{ and } U = R \cdot I. \tag{3.19}$$

Here U is the measured voltage and R is the resistance over which the voltage was measured, in this case the input impedance of the ADC. Combining the two equations leads to

$$Q = \int I dt = \frac{1}{R} \int U dt. \tag{3.20}$$

For this work, WARP was used, a processor also written by Julian Wulf and available on Github[1]. The code first flips the waveform according to the polarity of the signal and puts the baseline to zero. Then it takes a sample of noise and calculates its root mean square (RMS). The size of the noise sample and whether it is taken from the left or right end of the waveform can be set by the user. Next it starts scanning through the wavefrom. If the signal exceeds a certain threshold an event starts. It integrates the peak by summing up the measured voltages in all bins until the signal falls back under the threshold. The event is only stored if the signal in the meantime exceeded another, higher threshold. In this way, the front and especially the long tail of the waveform are also integrated while high noise peaks are avoided. The algorithm then continues scanning through the waveform to look for

---

[1] https://github.com/Physik-Institut-UZH/WARP, Accessed: 03.11.2021

other peaks. The thresholds can be set by the user in units of the RMS calculated before and is therefore dynamically adjusted. An example of waveform processed by WARP can be seen in figure 24.

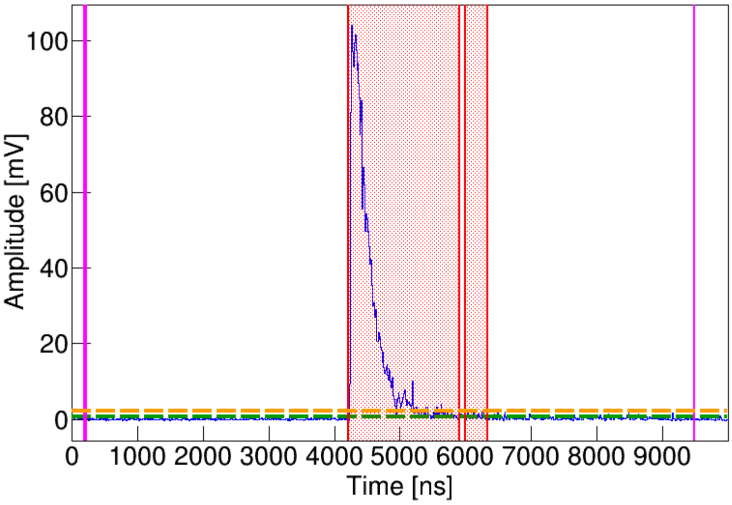

Figure 24: Example of a waveform processed with WARP. The waveform is plotted in blue while the areas over which the algorithm integrated are shaded in red. The region from which the RMS is calculated is marked by the pink line and the resulting high and low threshold are shown by the orange and green dashed lines respectively.

3.3.3 Determination of Operating Voltage

The optimal operating voltage was set by looking for the best energy resolution achieved in the different files. The resolution, R, was defined as

$$R = \frac{FWHM}{H_0} = \frac{2.355 \cdot \sigma}{H_0}, \tag{3.21}$$

where H_0 is the center of a peak an $FWHM$ its full with at half maximum. Under the assumption of a Gaussian shaped peak, the $FWHM$ can easily be calculated form the standard deviation σ. In order to find R, first, the total charge of all events in the processed datasets was histogrammed, such that the 661 keV peak of ^{137}Cs and the 122 keV peak of ^{57}Co become visible. The two peaks were then fitted with a Gaussian function, as in figure 25 (a), in all datasets. Finally, the energy resolution R was calculated for each peak and plotted as a function of the operating voltage as can be seen in figure 25 (b). For the 800 V and 900 V datasets, this was not possible because the low energy ^{57}Co peak at 122 keV vanished in the background. It can be seen that the detector resolution increases at higher operating voltages but then starts getting worse above 1200 V. Therefore, 1200 V was identified as the optimal voltage and all the following measurements were taken at this operating voltage.

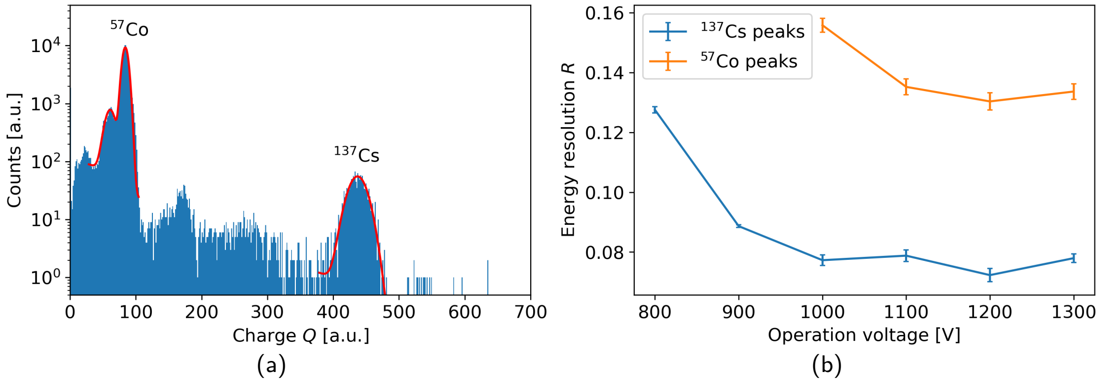

Figure 25: (a): Gaussian fit to the ^{57}Co and ^{137}Cs peak in the 1200 V dataset. Because the energy calibration was not performed yet, the x-axis is in arbitrary units. The ^{57}Co peak on the left has a double peak structure due to escaping photons. Also at twice the ^{57}Co peak charge, a small pileup peak can be seen. Due to the high ^{57}Co activity, some events follow each other to quickly for the processor to differentiate them. For the background data where the rate is much lower this is not a problem. (b): Energy resolution R of the ^{137}Cs and ^{57}Co peaks plotted against the corresponding operating voltage. The best energy resolution was observed at 1200 V.

3.4 Background Data: Measurement and Analysis

3.4.1 Measurement Procedure

The background measurement was conducted at two different locations in the assembly hall, where the DARWIN Demonstrator is located: One on top of the platform, and one beside the bottom part of the detector. The locations of the measurement are marked in figure 14 and can also be seen in figure 31. The data acquisition was performed in the same way as described in section 3.3.1 but with a CAEN V1724 ADC. For this run, the previously determined optimal operating voltage of 1200 V for the NaI(Tl) detector was set. At both locations, 20 data-sets containing 5×10^5 events each were taken during about 12 hours.

3.4.2 Energy Calibration

First, the collected data was processed as described in section 3.3.2. Then, the datasets were calibrated using the well-known energies of certain γ-peaks in the background spectrum. The considered peaks along with their energies and intensities can be found in table 3. Each of those peaks was fitted with a Gaussian function. Then, the peak energies were plotted against their position and a linear fit was performed through the data points in order to find the linear ADC units to energy conversion factor. The procedure is displayed in figure 26.

Isotope	^{40}**K**	^{214}**Bi**	^{208}**Tl**
Energy E_γ	1.46 MeV	1.76 MeV	2.61 MeV
Intensity I_γ [%]	10.66 ± 0.13	15.30 ± 0.03	99.754 ± 0.004

Table 3: Energies and intensities of the γ-lines used for the determination of the background rates. The energies are given without uncertainties because they are known up to at least five digits. Values from [115].

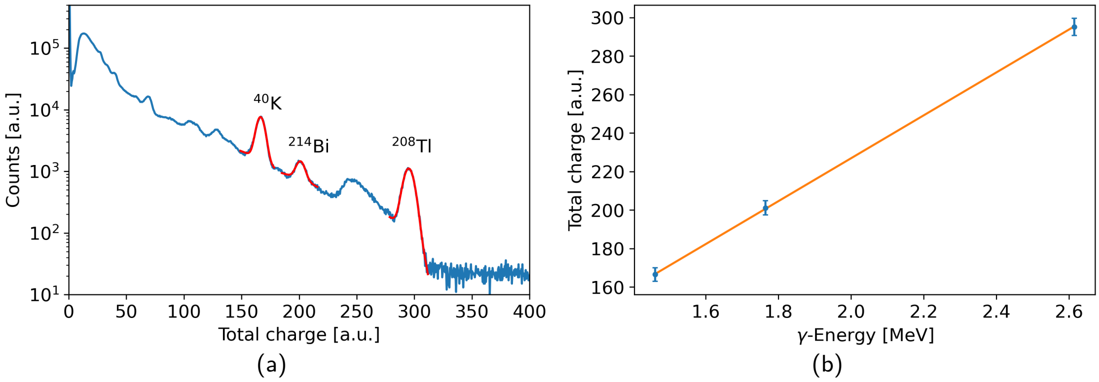

Figure 26: (a): Gaussian fit to the ^{40}K, ^{214}Bi and ^{208}Tl peak from left to right on the example of the bottom data-set. The different binning of the charge, compared to the test data, is due to the use of a different ADC model. (b): ADC bin position of the peaks plotted against their energy with a linear fit that can be used for the bin number to energy conversion. The error bars represent the σ of the fitted Gaussian.

3.4.3 Measurement of the Background Rate

To obtain the full background rate spectrum in a binning independent way, the following procedure was applied: First, the data was corrected according to the NaI(Tl) detector efficiency curve that is displayed in figure 27 (a). For each energy bin, the number of entries was divided by the detector efficiency at the corresponding energy to get the number of events that really hit the detector. Then the number of counts was divided by the total measurement time to get the rate, and by the bin width of the histogram in order to make the curve independent of the binning. The result of this procedure for the datasets taken at the top and bottom of the detector can be found in figure 27 (b). It can be seen that the background rate on top of the platform is about 1.4 times as high as at the bottom. The reason for this is not entirely clear. A possible explanation is that the walls in the lower part of the hall, which are made of bricks, are less radioactive than the concrete walls on top. Another explanation could be another radioactive object near the measurement on top. However, no such object could be identified with a Geiger counter.

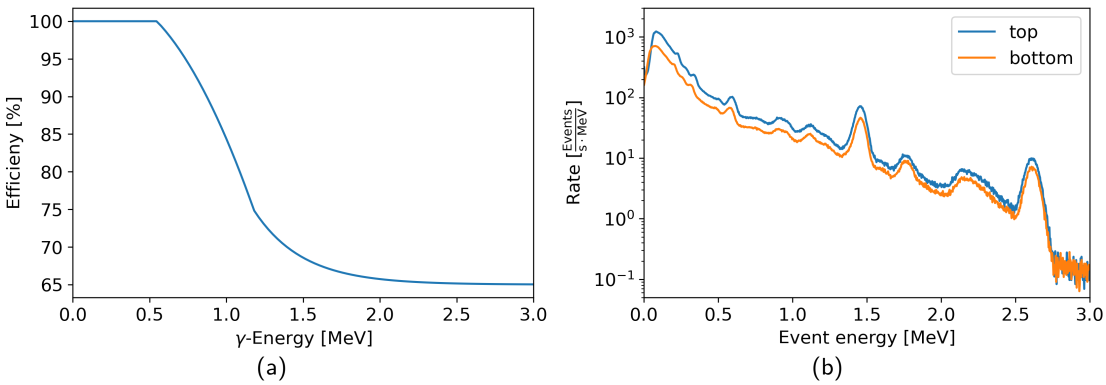

Figure 27: (a): Efficiency curve of the NaI(Tl) detector, values taken from [122]. (b): Background rate after calibration and efficiency corrections for the data taken on top and bottom of the Demonstrator.

3.5 Results

The goal is now to obtain the activity of the most important radioactive background components in the lab from the background rates calculated above. In order to achieve this, first, the relevant peaks were fitted with a Gaussian curve including a linear background. Integration over a peak gives the rate of the decay channel of the underlying γ-line. This corresponds to the green shaded areas in figure 28. The area can easily be calculated from the fit parameters since the total area under a Gaussian curve is

$$A = a \cdot \sigma \cdot \sqrt{2\pi}, \tag{3.22}$$

where a is the height of the peak and σ is the standard deviation. The total rate measured in the NaI(Tl) detector can then be calculated for each decay by dividing the area A by the intensity of the corresponding γ-line of the decay, listed in table 3. The resulting numbers can be found in table 4.

position	^{40}**K rate** [Hz]	^{214}**Bi rate** [Hz]	^{208}**Tl rate** [Hz]
top	48.7 ± 0.5	3.59 ± 0.11	0.94 ± 0.01
bottom	27.5 ± 0.4	2.73 ± 0.08	0.646 ± 0.007

Table 4: Measured decay rates of background components from which γ-rays hit the NaI(Tl) detector. The ratio of the values on top and bottom matches very well the trigger rate during data taking, where on top a rate of 250 Hz was observed, compared to 170 Hz at the bottom.

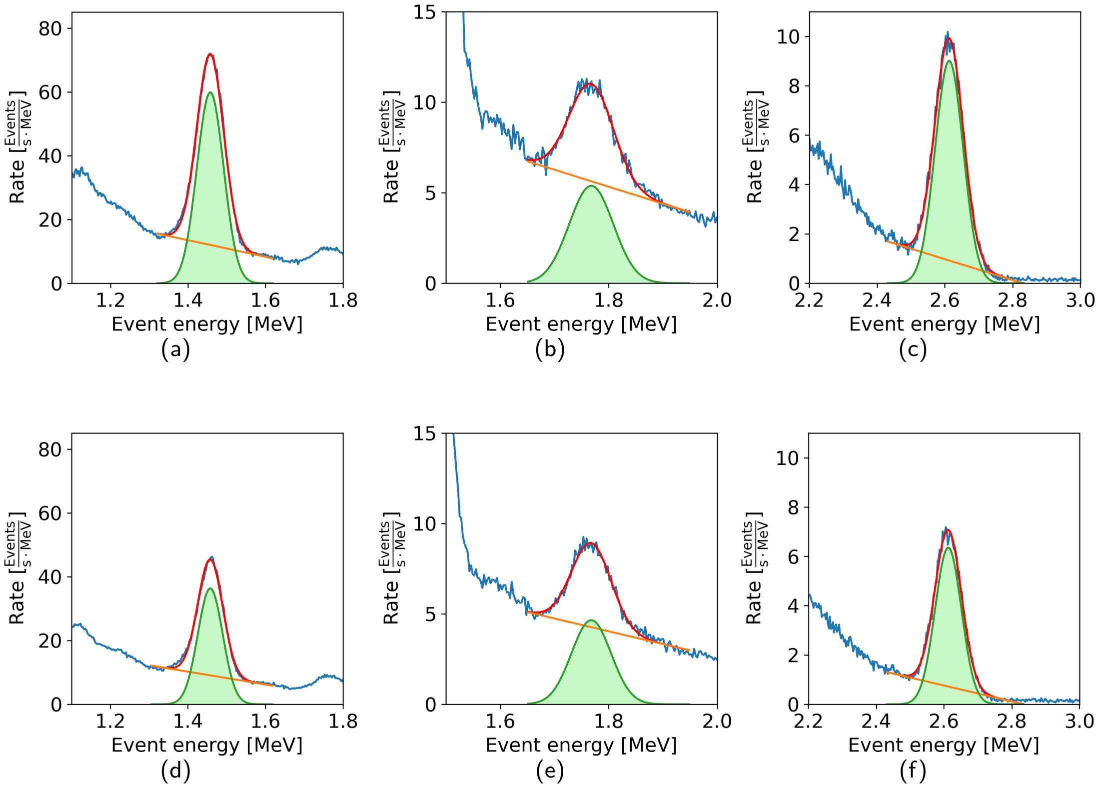

Figure 28: Gaussian fits to the ^{40}K, ^{214}Bi and ^{208}Tl peak from left to right in the background data. The plots (a), (b), and (c) are from the data taken on top, plots (d), (e), and (f) belong to the data taken at the bottom. The difference between the rates on top and bottom can clearly be seen.

From these numbers also the rates of the corresponding decay chains can be calculated. In case of ^{214}Bi this is trivial. All isotopes in the ^{238}U decay chain are assumed to have the same activity as ^{214}Bi because the long lived ^{238}U dictates the activity of the whole chain. In case of ^{208}Tl the branching ratio Br(^{212}Bi $\rightarrow$ ^{208}Tl) $= 35.94\,\%$ has to be taken into account [115]. This directly gives the measured background rates shown in table 5. To finally arrive at the actual rate R_{NaI} with which the detector is hit from outside, the intrinsic background of the NaI(Tl) detector, described in the section 3.2.2, has to be subtracted from these numbers.

In some experiments an imbalance of the activities of the first part of the decay chain (from ^{238}U to ^{230}Th) compared to the second part (from ^{226}Ra on) was observed [123]. Therefore, often the two parts of the chain are simulated separately. However, with this measurement no distinct rate for the first part of the decay chain can be calculated because only the three high energy γ-peaks treated above are clearly visible in the spectrum. Therefore, as a best guess, it was assumed that the whole decay chain is in equilibrium and thus has the same activity. The same holds for the ^{232}Th chain that is often split between ^{228}Ac and ^{228}Th.

	position	^{40}K rate [Hz]	^{238}U rate [Hz]	^{232}Th rate [Hz]
	top	48.7 ± 0.5	3.59 ± 0.11	2.61 ± 0.03
Measured	**bottom**	27.5 ± 0.4	2.73 ± 0.08	1.80 ± 0.02
	top	45.3 ± 0.8	3.1 ± 0.2	0.9 ± 0.4
$\mathbf{R_{NaI}}$	**bottom**	24.1 ± 0.7	2.1 ± 0.2	0.1 ± 0.4

Table 5: Calculated rates of ^{40}K as well as of the two decay chains without (first row) and with (second row) subtraction of the intrinsic background of the NaI(Tl) detector. It can be seen that the correction is small for ^{40}K and ^{238}U, while for ^{232}Th a big fraction of the events are coming from internal background.

Error Estimation

The uncertainty on the measured rates was calculated from the fitting parameters' covariance matrix returned by the fitting algorithm (scipy.optimize.curve_fit [2]). By diagonalizing this matrix one can get the uncertainties on the individual fitting parameters assuming no correlation between them. Then the uncertainty on the area can easily be calculated using Gaussian error propagation on the formula 3.22. However, the uncertainties on the final background rates R_{NaI}, shown in table 5, are dominated by the uncertainties on the internal background, listed in table 1.

---

[2] https://github.com/scipy/scipy/blob/master/scipy/optimize/_minpack_py.py#L533-L839, Accessed: 23.11.2021

4 Simulations

In this chapter, the simulations of different calibration sources and the expected radiogenic backgrounds in the DARWIN Vertical Demonstrator are described. The simulations were performed with Geant4 version 10.5 [6], a toolkit for the simulation of the passage of particles through matter.
After a short introduction to Geant4, this chapter follows the work flow of a simulation. It starts with the implementation and visualization of the detector geometry and then describes the simulation runs for the backgrounds and different calibration sources. For the external sources, additionally, a calibration setup is proposed which was also implemented in the simulation geometry.

4.1 Simulation With Geant4

Geant4 (**GE**ometry **AN**d **T**racking) is a C++ based object-oriented simulation toolkit for Monte Carlo simulations of the passage of particles through matter. It has applications in (astro-/)particle physics, nuclear physics, accelerator design, space engineering and medical physics. Geant4 was initialized at CERN as the followup of Geant3 in 1994. It was developed by a worldwide collaboration of scientist and engineers called RD44, and completed in 1998. A key requirement for Geant4 was its flexibility for different applications. Therefore, it was designed as a modular toolkit that offers class categories with coherent interfaces such that every user can assemble his/her program at compile time. On the one hand, it provides predefined modules for the implementation of the detector geometry, user interfaces, particle tracking, and visualization. On the other hand it also features libraries containing physical models and processes as well as experimentally determined data of particles and atoms. For the simulation of radioactive decays, Geant4 provides a decay module that contains all decays of the decay chains with their α-, β-, and γ-particle energy spectra [6].

4.1.1 General Working Principle

For a simulation, first, the geometry of the detector has to be implemented in the Geant4 framework. The geometry has to contain information about the materials from which the components are made of. This process for the Xenoscope is described in section 4.1.2. Once this part of the code is set up, it can be compiled and not modified again. One can then use macros to still communicate with the code and to specify, for example, the type, direction, and energy of the radiation Geant4 should simulate. A simulation run is stored in a ROOT file that contains for every simulated event its event number, the deposited energy of every step inside the active volume with its position and time, as well as information about the type of interaction and involved particles.

4.1.2 Implementation of Geometries

For the implementation of the geometry, first, a *world volume* has to be defined. This is the largest volume and the only one that does not have a *mother volume*, that is, a volume in which it is placed. The lab and detector parts first have to be designed, and then assembled in that volume. This is done in three steps:

- First, a so called *solid* has to be defined which is just a geometrical object. Geant4 provides different objects to choose from to create *solids*, for example boxes, cylinders, tubes, or polygons. The dimensions of all those shapes have to be adjusted manually. More complex shapes can be built by cutting out one object from another, or by joining them.

- Then, every *solid* has to be turned into a *logical volume* by assigning a material to it. A material can be defined by specifying its name, density, and the atomic components it consist of. The elements can be imported from a library or defined by hand.

- Finally, the *logical volume* has to be placed in a *mother volume* in order to become a fully defined *physical volume*. The *mother volume* can be the *world volume* or every other *logical volume*, but at least one *logical volume* needs to have the *world volume* as its *mother volume*. The volume that needs to be placed has to completely overlap with its *mother volume*, but must not overlap with any other volume that was placed in the assembly so far. To check this, Geant4 has a built-in test that raises an error if an overlap is detected. In the end, all volumes must be *physical volumes* except for the *world volume*.

4.1.3 Visualization Using Geantino Simulations

Because the whole geometry is implemented in code only, without a graphic interface, it is very hard to spot mistakes. For this purpose visualization with geantinos is very useful. Geantinos are a virtual particle species invented by Geant4. They emerge evenly distributed in a defined physical volume and then travel in a straight line to a random direction without any interaction. Plotting the points of origin of all geantinos, selected volumes can be visualized, as it was done in figure 30.

4.2 Implementation of the Xenoscope Geometry

The used Geant4 code is a customized version of the DARWIN simulation code developed by the collaboration, adapted to the Demonstrator project needs. It has two major differences to the DARWIN code. One of them is that the particle tracking information gets recorded not only in the liquid xenon, but inside the whole mother volume. This makes it easier to understand external calibration sources and allows to check the radiation load in the surroundings of the detector. The other difference is, of course, the detector geometry, which was reimplemented from the ground up. This part of the code was broken down into four parts that are stored in separate files, which makes the code easier to read and edit. A diagram of the code structure can be found in figure 29.

- In the file *Construct Lab*, the mother volume, made out of vacuum, is defined. Then, a concrete box of the size of the lab, including walls, ceiling, and floor is placed in it. The actual lab is then inserted as a box of air inside the concrete. Finally the windows are added as air boxes in the concrete walls.

- In the file *Construct Cryostat*, the outer cryostat, made of steel, is defined. Inside, a volume of vacuum is placed that itself contains the volume of the inner cryostat, which again is made of steel.

- In the file *Construct TPC*, first, the liquid xenon volume is defined, filling up the whole cavity of the inner cryostat. Afterwards, in the top section, the liquid xenon is replaced by gaseous xenon. Then the six polyamide-imide pillars and 172 field shaping rings made out of copper are placed in the liquid xenon. Here, holes for the copper rings had to be cut out of the pillars, and the uppermost part of the pillars had to be cut out of the gaseous xenon in order to prevent overlap errors.

- In the file *Detector construction* everything comes together. The cryostat is positioned in the lab, and the liquid xenon with the TPC is placed in the inner cryostat.

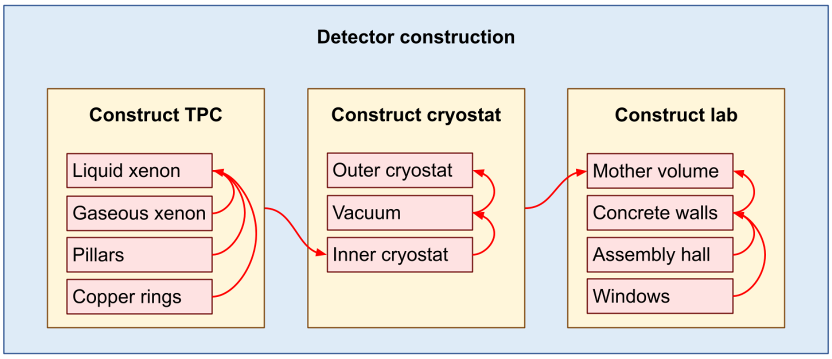

Figure 29: Structure of the Geant4 code for the implementation of the Xenoscope geometry.

The dimensions of all the relevant detector components were measured in the 3D model of Xenoscope designed by Frédéric Girard, Kevin Thieme and Yanina Biondi in SolidWorks [124]. The code of the final geometry is accessible on Github[1] and can be used for additional simulations in the future. It can be seen in the geantino visualization in figure 30. For this, in every volume 10^5 geantinos were simulated and their initial positions were marked in a scatter plot.

---

[1] https://github.com/Physik-Institut-UZH/DemonstratorXenonscope, Accessed: 02.11.2021

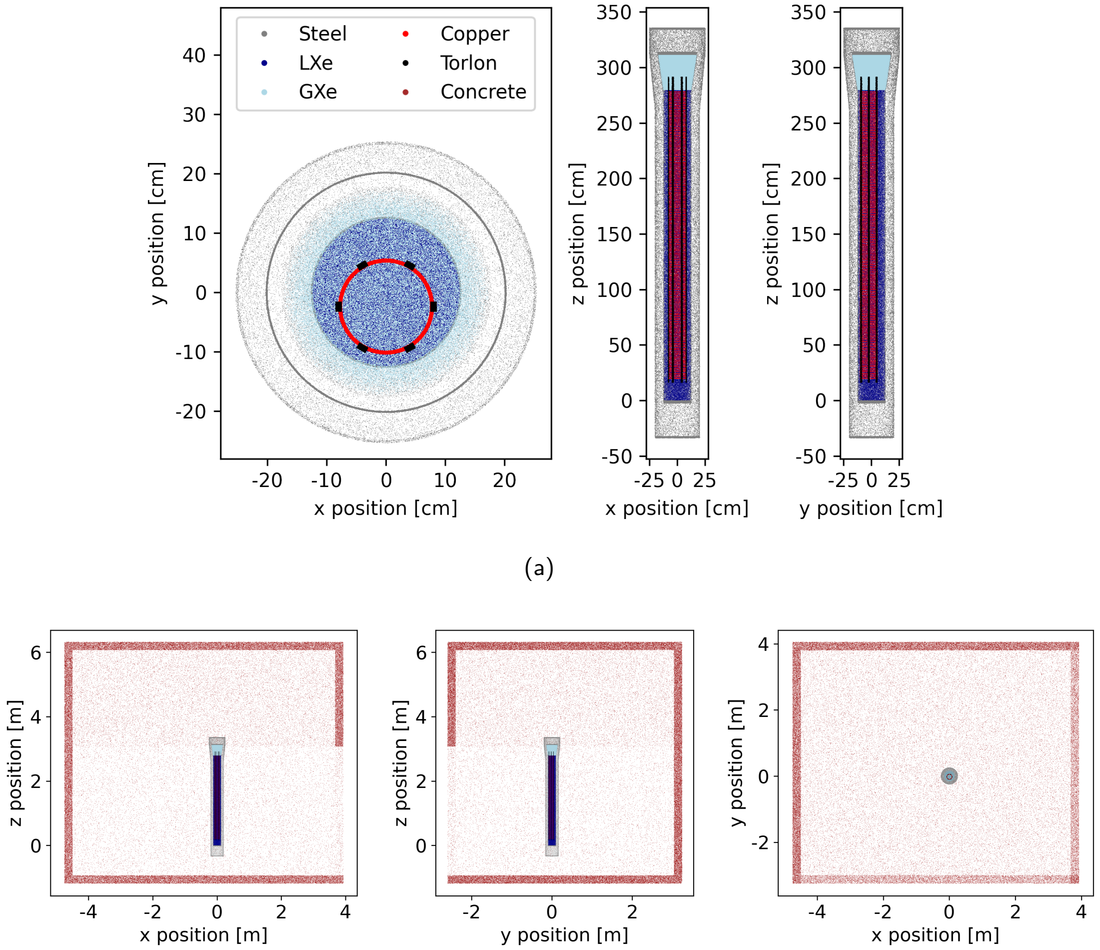

(a)

(b) (c) (d)

Figure 30: (a): Visualization of Xenoscope using geantino simulations. The detector can be seen from top, front, and side. The outer and inner cryostat are grey, the liquid and gaseous xenon dark- and light-blue respectively, the polyamide-imide pillars black and the copper rings red. Lower figures: Position of the Demonstrator in the assembly hall as seen from (b): the front, (c): the side, and (d): top. The colours are the same as in figure (a). Additionally, the concrete walls are shown in brown.

4.3 Background Simulation

The idea of the background simulation was to simulate a certain number of events that hit the demonstrator from outside. The simulation then shows how much energy was deposited inside the TPC in each energy bin for the entire number of events. The spectrum of the deposited energies can afterwards be scaled according to the measured activity values of the different background components, listed in section 3.5. This will be done in the analysis of the background simulation data, described in the section 5.1.1.

The simulation is more efficient in terms of computational time if the events are simulated as close as possible to the detector, instead of inside the thick concrete walls. Therefore, a cylinder was defined that just encloses the whole Demonstrator. It was chosen to have a radius 1 mm larger than the outer cryostat at its widest extent on top, and to be larger than the detector by 1 mm on the top and bottom. The virtual cylinder is shown in figure 31.

The background events were then simulated originating from the surface of the cylinder. This led to the question of how the measured background rates can be scaled up to the expected rates of particles hitting the cylinder. This was solved with a geantino simulation, described in the next subsection.

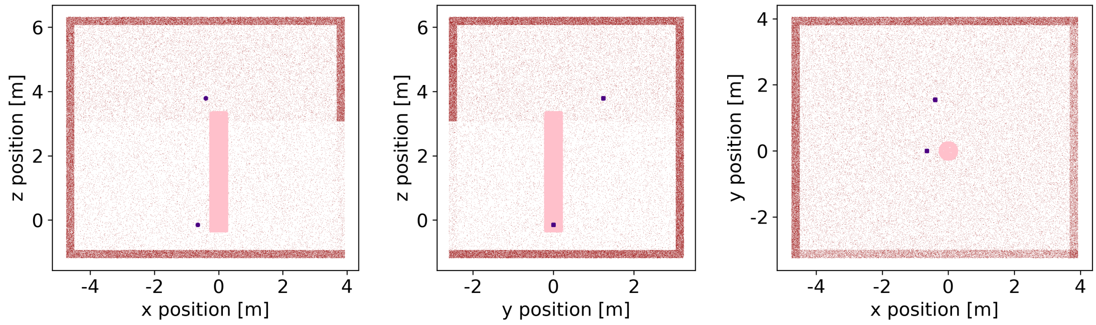

(a) (b) (c)

Figure 31: Position of the defined cylinder around the Demonstrator and the NaI(Tl) detector at its two measurement positions in the lab. Again with (a): from the front, (b): from the side, and (c): from top. The cylinder is shown in pink while the NaI(Tl) detector is coloured in indigo.

4.3.1 Upscaling With Geantino Simulation

The upscaling of the measured rate in the NaI(Tl) detector to the volume of the Demonstrator is very hard to calculate. One would have to integrate over the solid angles covered by the NaI(Tl) detector from every point in the concrete walls and ceiling, and then compare this number to the analogously integrated solid angle covered by the cylinder around the Demonstrator. Therefore, another simulation was used for this purpose. Because the main background is assumed to originate from the concrete walls and because radiation travels more or less in a straight line in air, in a first step 10^8 geantinos were simulated in the concrete. Then, it was counted how many of them passed through the volume of the NaI(Tl) detector at its two measurement positions, which was defined as a hit. For this purpose, the NaI(Tl) crystal of the detector also had to be placed in the Geant4 geometry, as shown in the geantino visualization of figure 31. By comparing this number to the amount of geantinos that hit the Demonstrator cylinder, the relative geometrical acceptance of the Demonstrator with respect to the NaI(Tl) detector, at its two measurement positions, could be calculated. The relative acceptance A_r was simply defined as the number of hits in the Demonstrator cylinder divided by the number of hits in the NaI(Tl) crystal:

$$A_r^{top(bottom)} = N_{hits,D}/N_{hits,NaI}^{top(bottom)} \tag{4.1}$$

The corresponding numbers are shown in table 6. This leads to a relative acceptances for the two measurement positions of

$$A_r^{top} = 205.3 \text{ and } A_r^{bottom} = 176.2. \tag{4.2}$$

This means that the rate of particles hitting the cylinder around the Demonstrator from outside, R_D, is

$$R_D = A_r \cdot R_{NaI}, \tag{4.3}$$

where R_{NaI} are the rates from section 3.5 with which the background hits the NaI(Tl) crystal from outside.

Total	**Demonstrator hits**	**NaI(Tl) hits** (top)	**NaI(Tl) hits** (bottom)
10^8	$N_{hits,D} = 568096$	$N_{hits,NaI}^{top} = 2767$	$N_{hits,NaI}^{bottom} = 3224$

Table 6: Total number of simulated events in comparison to the amount of events that hit the Demonstrator or the NaI(Tl) detector respectively.

4.3.2 Crosscheck Concrete Activity

In principle, the radioactive decays leading to a background in Xenoscope could also directly be simulated in the concrete surrounding the detector. The background rate from the concrete would even be easier to find out than the rate on the cylinder around the Demonstrator. However, one would need to simulate an enormous amount of decays in the concrete such that some of the decay products reach the Demonstrator. Even fewer would then make their way into the TPC and deposit energy in the liquid xenon. Therefore, the approach described before was chosen for the background simulations.

Nevertheless, the activity of the concrete was estimated in order to check whether the resulting values are reasonable and comparable with existing measurements of concrete samples. For this, 10^7 decays of ^{40}K, ^{214}Bi, and ^{208}Tl were simulated directly in the concrete, while leaving the NaI(Tl) detector in the Geant4 geometry. Then, the number of hits in the NaI(Tl) detector, N_{NaI}, were counted in order to calculate the fraction of γ-particles that were detected, compared to the total amount of decaying particles in the concrete, $N_{Concrete}$. Using this fraction, the measured rates, R_{NaI}, were scaled up to the absolute decay rates originating from the concrete. Finally, the number was divided by the total mass of the concrete $m_{Concrete}$, in order to get a value of the concrete activity, $A_{Concrete}$, in units of Bq/kg. The full formula reads:

$$A_{Concrete} = R_{NaI} \cdot \frac{N_{Concrete}}{N_{NaI}} \cdot \frac{1}{m_{Concrete}}. \tag{4.4}$$

The procedure was applied to the measured rates in the NaI(Tl) detector on top and at the bottom independently. The resulting numbers can be found in table 7, together with a comparison of activity values found in the literature. Only for ^{40}K the calculated values lay within the expected range, while for ^{214}Bi and ^{208}Tl the numbers are too low. However, it has to be noted that these numbers have to be taken as a very rough estimate for numerous reasons, the first of them being that the statistics are very low. Even though 10^7 decays of each type were simulated, only a handful of them hit the NaI(Tl) detector. Another reason is that the amount of the concrete was only estimated, its thickness of 25 cm was just measured at one wall where it was visible. Then it was assumed that all other walls, the ceiling and the floor have the same thickness. Further, parts of the walls consist of bricks instead of concrete. Lastly, also the concrete activity itself can vary greatly depending on where it was produced.

Activity [Bq/kg]	^{40}**K**	^{214}**Bi**	^{208}**Tl**
Calculated value	64-109	0.46-0.48	0.004-0.037
Literature value	50-1300	7-92	4-71

Table 7: Calculated values of the concrete activity according to the measurements at the bottom (lower value) and on top (higher value), compared to a range of values from the literature, taken from [118]. A German source was used because concrete activities strongly vary geographically.

4.3.3 Simulation of Radiogenic Background Spectrum

The background was simulated uniformly distributed on the surface of the geometrical cylinder around the Demonstrator shown in figure 31 and described in section 4.3.1. The events were generated isotropically, therefore one can assume that only half of them made their way into the cylinder. This factor of two has to be taken into account, because in equation 4.3 the rate R_D refers to events hitting the cylinder from outside.
For ^{40}K, 10^6 events were simulated. For ^{214}Bi, 10^7 events of the ^{238}U decay chain were simulated. Therefore, only one out of ten of those events are ^{214}Bi decays. Similarly for ^{208}Tl, 10^7 events of the ^{232}Th decay chain were simulated which includes fourteen steps. The formula for the number of generated events N_{hit} that hit the detector from outside reads

$$N_{hit}(^{40}\mathrm{K}/^{214}\mathrm{Bi}/^{208}\mathrm{Tl}) = \frac{N_{Simulated}}{2 \cdot N_d}, \tag{4.5}$$

where N_d is the number of decays in the corresponding decay chain, and $N_{Simulated}$ is the total number of events generated in the simulation.

4.4 Simulation of Calibration Sources

In general, particle detectors need to be calibrated in order to correctly reconstruct the energy of an event. The calibration also reveals the energy resolution of the detector, that is, how well the energy of an interaction can be reconstructed. Most particle detectors, including TPCs, can in principle be calibrated in two different ways. The first method makes use of the permanent radiogenic background of the experiment. The detector is calibrated using the well known energies of mono energetic γ-lines in the background spectrum. This method is convenient because no additional radiation is introduced into the lab. The downside is that this method is limited to the γ-lines that are visible above the unknown background. Typically, this is only the case at the highest energies, as for example the ^{40}K, ^{214}Bi, and ^{208}Tl peaks used for the NaI(Tl) detector calibration described in the section 3.4.2. However, this energy region is not always the target region of the different experiments. In addition, given that radiogenic background is attenuated differently depending on the materials it goes through, a calibration in different parts of the detector is not always possible which might be useful to test the detector response at different locations in the active volume.

The second method is more robust and versatile. It uses calibration sources whose decay properties are well understood. The peak(s) of their decay spectra are then used for the calibration. The sources can be chosen as strong as necessary in order to be clearly visible above the background. To make sure that the calibration source does not introduce an unwanted additional background there are different possibilities. The first one is to remove the source after the calibration, which is sometimes not possible if it is introduced inside the detector. The other possibility is to carefully choose a source that has a short half-life and decays fast enough such that it does not interfere with the experiment.

The background model obtained from the simulation which will be shown in section 5.1.1, reveals that in principle a calibration of the DARWIN Demonstrator using the ^{40}K, ^{214}Bi, and ^{208}Tl peaks is possible in the low MeV range. However, using different calibration sources, the calibration can cover the whole energy range from few keV to several MeV. Further, it allows for testing the detector response at different heights in the TPC, which will be of great interest in order to find out the electron lifetime, whether drifting electrons over 2.6 m is even possible. Therefore, six different calibration sources are considered in this study. The goal was to find out how strong they have to be for the calibration and if they are available at the Physics Institute of the University of Zurich or could be bought. The calibration sources can be divided into two subgroups that are fundamentally different regarding the calibration- and therefore also the simulation process. They are referred to as internal or external calibration sources and they are treated separately in the sections below.

4.4.1 Internal Sources

Internal calibration sources are introduced into the detector and decay homogeneously distributed inside the liquid xenon as illustrated in figure 32. For that, they have to be dissolved in the gaseous xenon and flushed into the TPC. This is often done with a solid source that is placed in the xenon gas flow. The decay product can then pass through a filter that holds back the solid source. By controlling the gas flow, the amount of radiation in the TPC can be precisely adjusted. To remove additional radiation after the calibration, the radioisotope must either decay or it has to be filtered out of the liquid xenon. The latter can be done using a hot metal getter, as for other impurities, if the isotope is not a noble gas [125], or by distillation otherwise [111]. The three calibration sources considered for this study are individually presented in more detail below.

For the internal sources $2{\times}10^7$ decays were simulated. This is sufficient since the events are evenly distributed inside the liquid xenon and deposit almost all their energy in the detector.

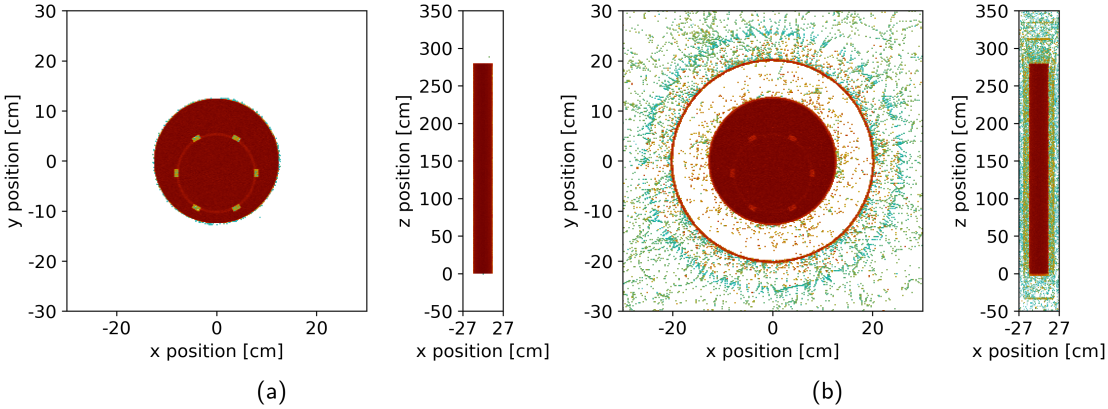

Figure 32: Energy deposition heat map of the internal calibration sources (a): ^{83m}Kr and (b): ^{220}Rn. One can see that for ^{220}Rn more radiation can escape the detector because the decay contains higher energy γ-rays. Therefore, in this case it has to be checked whether the level of radiation is low enough in the close vicinity of the detector.

^{83m}Kr

The metastable ^{83m}Kr is produced in the decay of a rubidium source that can be placed in the xenon gas flow. The ^{83}Rb isotope decays through electron capture into an excited state of ^{83}Kr with a total Q value of 919.4 keV. Normally, the excited state quickly decays into the ground state, but sometimes the metastable intermediate state ^{83m}Kr is reached. It has an energy of 41.5 keV above the ground state and a half-life of $t_{1/2} = 1.83\,\mathrm{h}$. This is enough time for the emerged krypton gas to dissipate in the xenon and flow into the detector. In the detector, the ^{83m}Kr decays in two steps of energy 32.1 keV and 9.4 keV into its ground state, emitting mostly internal conversion electrons accompanied by X-rays or Auger-Meitner electrons. The intermediate state is metastable as well, but with a shorter half-life of 155 ns [115]. The decay scheme can be found in figure 33.

Usually, TPCs have a sufficient time resolution to distinguish these two lines. In that case, ^{83m}Kr events can efficiently be selected by demanding two S1 signals followed by two S2 signals with the same time difference. The event selection has the advantage that a low activity, even below the background level, is sufficient for the calibration. All three peaks, at 9.4 keV, 32.1 keV, and the combined at 41.5 keV, can be used for the calibration. The produced krypton is, like xenon, a noble gas and therefore does not disturb the detector operation. All of this makes ^{83m}Kr a very popular calibration source for xenon TPCs, as used for example in XENON100 [126] or LUX [127]. Also at the University of Zurich, a TPC was calibrated with krypton [96]. However, for the DARWIN Demonstrator it will not be possible to resolve the short time difference between the two lines, because the S1 signals will not be detected and the S2 signals will be spread out due to the long drift time. Therefore, the ^{83m}Kr decay energy spectrum in the Demonstrator will show a single peak at 41.5 keV. The simulated decay energy spectrum is shown in figure 34 (a).

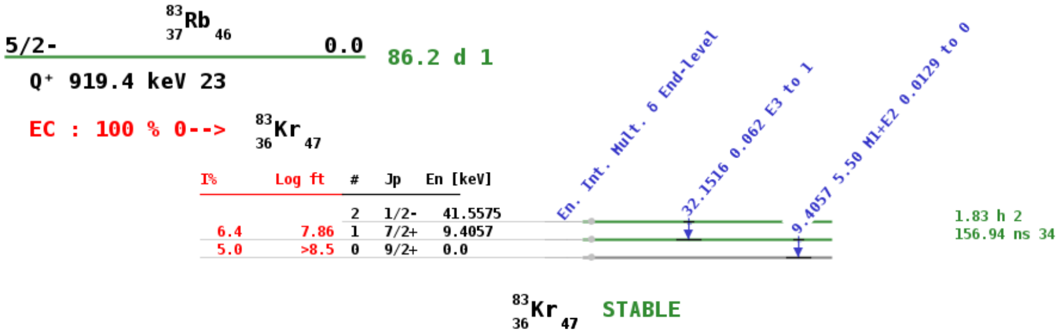

Figure 33: Decay plot of ^{83}Rb to ^{83}Kr with the metastable intermediate states important for the calibration. Figure plotted with [128] based on data from [115].

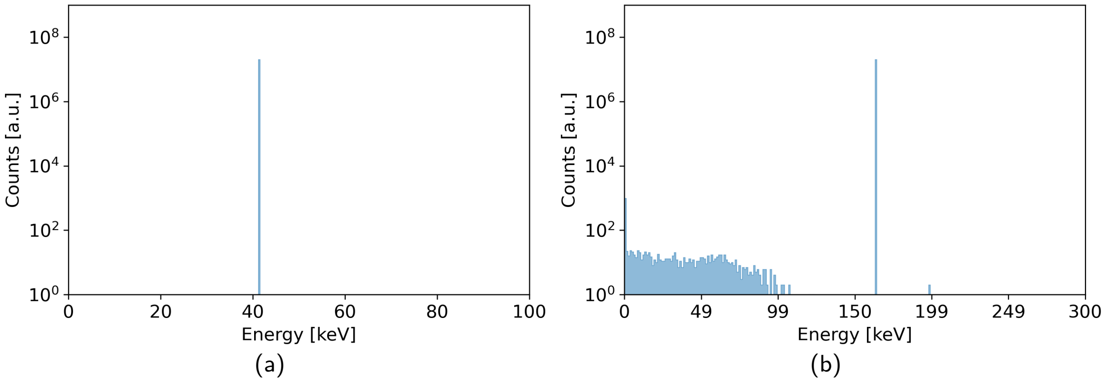

(a) (b)

Figure 34: (a): Histogrammed total decay energy in the entire Geant4 geometry of all simulated ^{83m}Kr events. Only the combined peak at 41.5 keV is visible. (b): Histogrammed total decay energy in the entire Geant4 geometry of all simulated ^{131m}Xe events. Besides the peak at 163.9 keV, single events that happened close to the edge of the TPC can be seen, that made their way through the steel walls of the cryostat and escape the lab through the window in the concrete walls. Because not the entire energy of these decays is deposited in the Geant4 geometry, they show up as a flat component below approximately 100 keV.

^{131m}Xe

The concept of a calibration with ^{131m}Xe is very similar to ^{83m}Kr. It is produced in the β^--decay of ^{131}I with a Q value of 970.8 keV. ^{131m}Xe has a half-life of $t_{1/2} = 11.84$ d and decays directly into the ground state releasing 163.9 keV by emitting mostly internal conversion electrons accompanied by X-rays or Auger-Meitner electrons. The full decay scheme can be found in figure 35 and the energies of the simulated events in figure 34 (b). ^{131}I is solid at room temperature and can thus be handled similarly to ^{83}Rb. The advantage of calibrating a liquid xenon TPC with ^{131m}Xe is that the decay product is not an impurity in the detector and does not have to be filtered out. ^{131m}Xe is a relatively novel calibration source that was used in LUX [129].

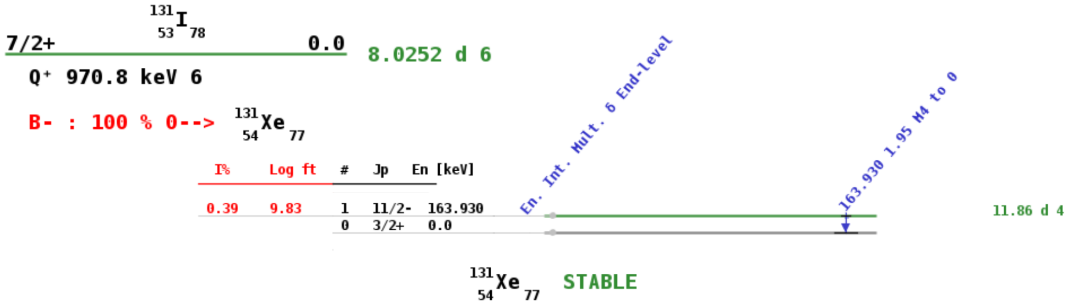

Figure 35: Decay plot of ^{131}I to ^{131}Xe with the metastable intermediate state ^{131m}Xe important for the calibration. Figure plotted with [128] based on data from [115].

^{220}Rn

In contrast to ^{83}Kr and ^{131}Xe, the noble gas ^{220}Rn is radioactive and part of the ^{232}Th decay chain. As described in chapter 3.1.4, this is one of the considered backgrounds of the experiment, although it is subdominant compared to ^{222}Rn which is part of the more active ^{238}U decay chain. The decay schemes of ^{220}Rn and its follow up decays in the chain can be found in figure 60 in the appendix. The full simulated energy spectrum of ^{220}Rn, including all following decays, is shown in figure 36. Event though the properties of the decay(s) are very different, the concept of a calibration with ^{220}Rn is similar to the ^{83m}Kr and ^{131m}Xe sources above. The solid source that can be placed in the gas flow is in this case a stainless steel disc electroplated with thorium nitrate Th(NO$_3$)$_4$. The contained ^{228}Th decays through an α-decay into ^{224}Ra which decays through another α-decay into the ^{220}Rn wanted for the calibration. The noble gas ^{220}Rn dissipates in the xenon gas and gets transported into the detector. The two described alpha decays have long half lives ($t_{1/2} = 1.9$ years and 3.6 days respectively) while the longest lived isotope following ^{220}Rn in the chain is ^{212}Pb ($t_{1/2}$ =10.6 hours). Therefore the calibration source signal sufficiently decays in a few days if one can avoid contaminating the detector with ^{228}Th or ^{224}Ra. Also contamination of the ^{228}Th source with ^{230}Th has to be avoided because this would lead to the emanation of ^{222}Rn ($t_{1/2} = 3.6$ days). The proof of principle of a calibration with ^{220}Rn was shown in [125] and applied in the XENON100 and XENON1T experiments [130, 131].

Using a whole decay chain means more possibilities for the calibration. First of all, a calibration can be performed at high energies using the alpha decays of the chain above 6 MeV. Another useful feature of this chain is the ^{220}Rn-^{216}Po coincidence, which allows to select those events efficiently, as described for ^{83m}Kr above. However, unlike for ^{83m}Kr, the ^{216}Po half-life ($t_{1/2} = 144\,\mathrm{ms}$) is long enough for the radioisotope to travel a short distance with the liquid xenon flow. This allows to map convection in the detector and for example detect regions with a low recirculation flow. On the downside, the β-spectra introduce a large additional background below 5 MeV which is, however, not relevant during the energy calibration.

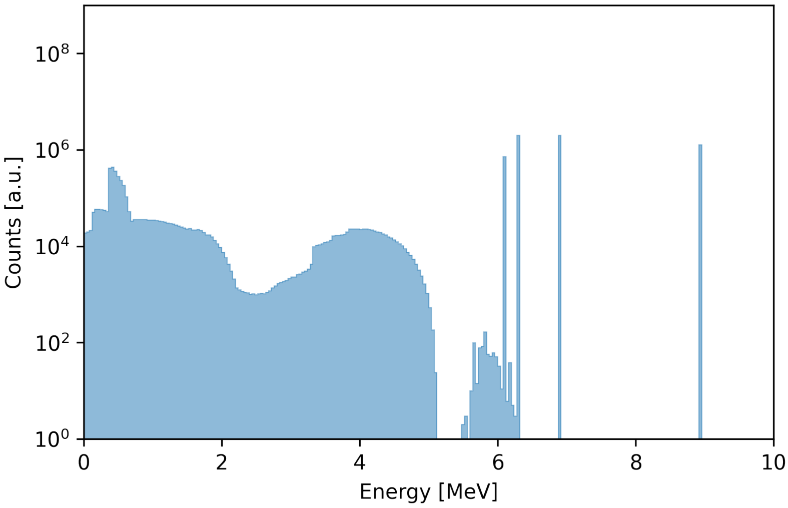

Figure 36: Total energy deposition of the simulated ^{220}Rn source, with all the follow-up decays of the chain, in the entire Geant4 geometry. The four high peaks above 6 MeV are from the four dominant α-decays of the chain. The spectrum below 5 MeV is due to β^--emission and the step feature around 0.2 MeV is due to a β^--decay in coincidence with an associated γ-ray. Around 6 MeV some events can be seen that come from α-decays of ^{220}Rn and ^{212}Bi with lower branching ratios.

4.4.2 External Sources

External calibration sources are placed outside the detector. The radiation then has to travel through the outer part of the detector like the radiogenic background. Because steel and the layer of LXe outside the TPC efficiently absorb α- and β-radiation, only the energetic enough γ-peaks of the decays can be used for the calibration. At the same time, a much broader range of sources can be used because external calibration sources do not need to be soluble in liquid xenon. In order to shield the lab from the radiation of the calibration source, the source needs to be collimated. During this work it was found that the details of the collimator setup have a big influence on the rate of detected events, as shown in figure 37. Therefore, a setup that can realistically be built was designed for this purpose. This is detailed in section 4.4.3.

For the external sources 2×10^8 decays were simulated. The statistics needed to be higher than for the internal calibration sources because a large fraction of the events are absorbed by the collimator or the steel walls of the outer and inner cryostat.

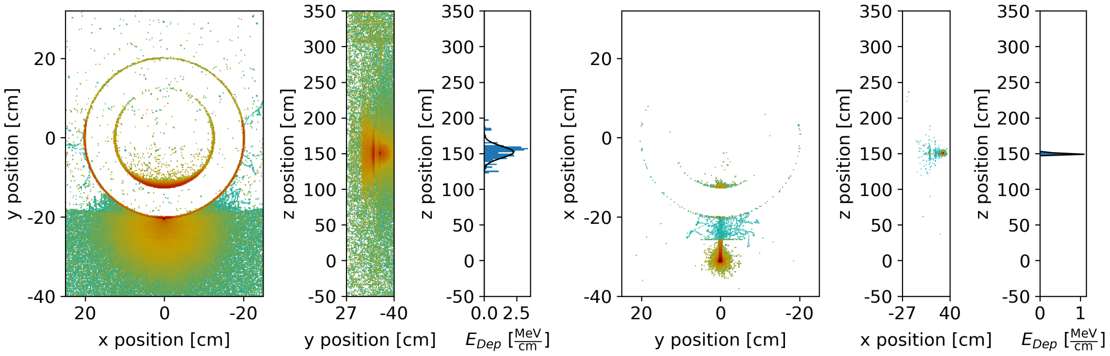

(a)

(b)

Figure 37: Energy deposition heat map of an external ^{57}Co calibration source (a): without and (b): with the designed collimator setup. The source position was rotated by 90° for the collimator setup but the general observation remains: A collimator can efficiently shield the lab from radiation and restrict the energy deposition inside the TPC, E_{Dep}, to a well defined height. This is required for a calibration at different z positions and can be used to calculate the electron lifetime. The standard deviation of the energy deposition height was $\sigma = 6$ mm for the collimator setup compared to over 8 cm without collimator.

^{137}Cs

^{137}Cs decays with a half-life $t_{1/2} = 30.08$ years through β^--emission into ^{137}Ba with a Q value of 1175.6 keV. It has only one γ-peak at 661.7 keV with a high branching ratio that can be used for the calibration. The full decay scheme of ^{137}Cs is shown in figure 38, while the histogrammed decay energy simulated with Geant4 is shown in figure 39 (a).

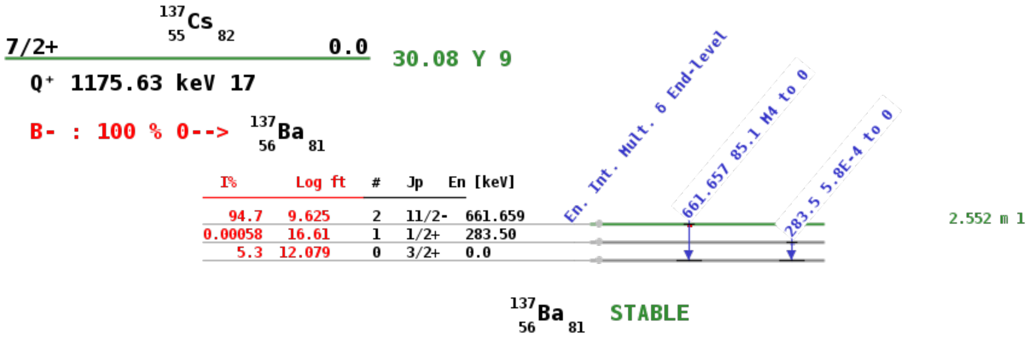

Figure 38: Decay plot of the β^--decay of ^{137}Cs to ^{137}Ba. Figure plotted with [128] based on data from [115].

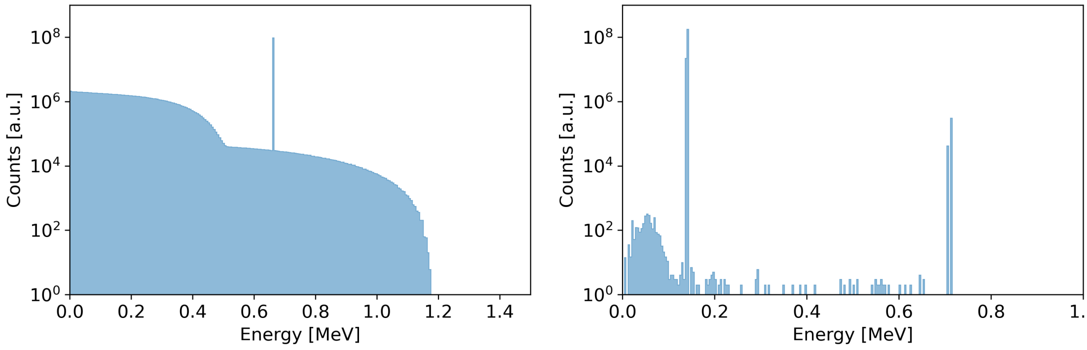

(a) (b)

Figure 39: (a): Histogrammed total decay energy of all simulated ^{137}Cs source events in the entire Geant4 geometry. The β^--spectrum is clearly visible along with the dominant γ-peak at 661.7 keV. (b): Histogrammed total decay energy of all simulated ^{57}Co source events in the entire Geant4 geometry. The dominant γ-peaks at 136.4 keV and 692.4 keV can be seen clearly. The double peak structure is due to coinciding X-rays from electron rearrangement, typical for EC-decays. The events besides the peaks again escaped the Geant4 geometry through one of the windows.

^{57}Co

^{57}Co decays through electron capture with a half-life of $t_{1/2} = 271.7$ days into ^{57}Fe with a Q value of 836.0 keV. It has several low energy γ-peaks with high branching ratios at 122.1 keV, 14.4 keV and 136.4 keV. Additionally it has a higher energy peak at 692.4 keV which has a lower but still sufficient branching ratio in order to be used. All other γ-lines have very low intensities for a calibration. The full decay scheme of ^{57}Co is shown in figure 40, while the histogrammed decay energy simulated with Geant4 is shown in figure 39 (b).

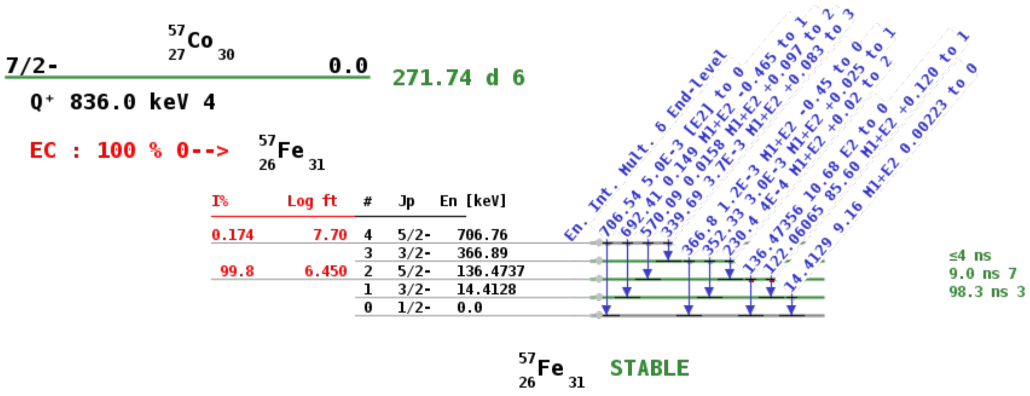

Figure 40: Decay plot of the electron capture of ^{57}Co to ^{57}Fe. Figure plotted with [128] based on data from [115].

^{133}Ba

^{133}Ba decays through electron capture with a half-life of $t_{1/2} = 10.5$ years into ^{133}Cs with a Q value of 517.5 keV. The decay features γ-lines at 356.0 keV, 81.0 keV, 302.9 keV and 383.8 keV starting with the highest intensity. All other γ-lines have very low intensities for a calibration. The full decay scheme of ^{133}Ba is shown in figure 41, while the histogrammed decay energy simulated with Geant4 is shown in figure 42.

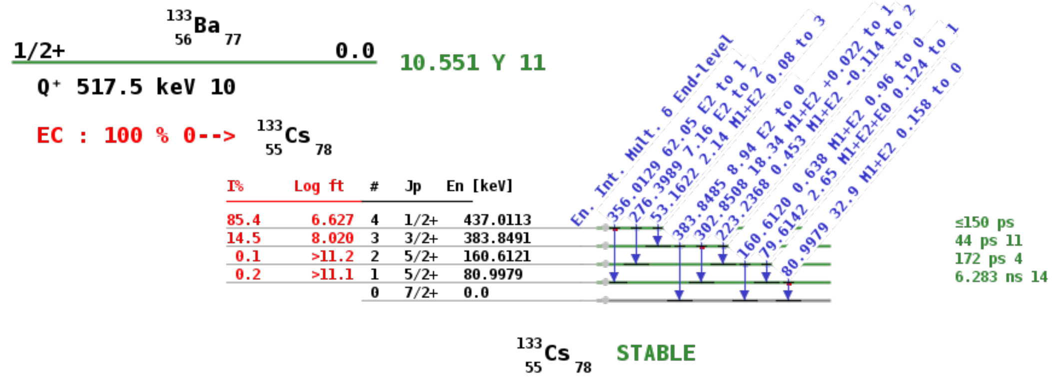

Figure 41: Decay plot of the electron capture of ^{133}Ba to ^{133}Cs. Figure plotted with [128] based on data from [115].

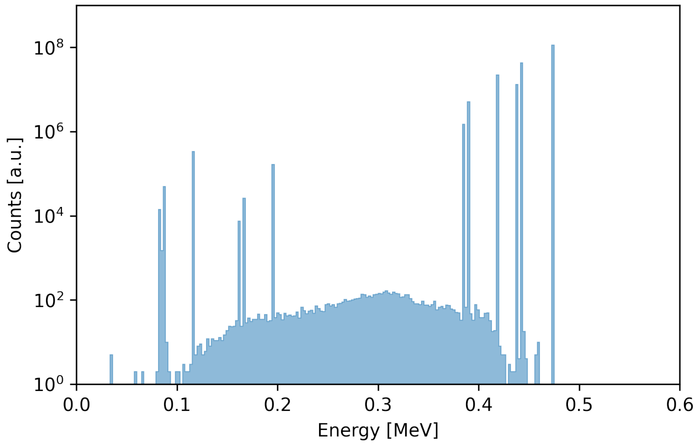

Figure 42: Histogrammed total decay energy of all simulated ^{133}Ba source events in the entire Geant4 geometry. Again, the main γ-peaks are split and shifted due to coinciding X-rays from electron rearrangement. The continuous spectrum between the peaks is once more from events that escaped the Geant4 geometry.

4.4.3 Collimator Setup

As stated above, the result of the simulation for the external calibration sources strongly depends on the details of where the sources are placed and how they are collimated. It was tried out to place the source directly on top and below the outer cryostat, as well as on its side. The simulations on top and below showed almost no events hitting the liquid xenon inside the TPC because the radiation gets absorbed in the large amount of steel and liquid xenon it has to cross. Also, because the radiation travels in z-direction, the energy deposition would be less localized in height which is not ideal for testing the detector response at different z positions. Thus, the only remaining option was to place the collimator on the side.

In order to obtain a meaningful and useful result, a calibration setup for the DARWIN Demonstrator was designed using SolidWorks [124]. The requirements for the structure were, besides a good shielding from radiation, affordable parts, stability, safety and easy feasibility. Additionally, the calibration should be possible at different heights. To safely satisfy the first requirement a collimator from the institute was employed, shown in figure 43 (a). This collimator can shield a source with an activity of $\mathcal{O}$(MBq). It is made out of a lead cylinder of 13.1 cm diameter and 10.0 cm height. On the front it has a hole of 6.4 mm in diameter where the radiation escapes, that can be closed with a lead plug when no radiation is needed. At the bottom it has another, larger lead plug through which the source in the collimator can be accessed and exchanged. The whole lead cylinder is situated in an aluminum case with a handle, which can be used as a suspension device. In the proposed design, the collimator hangs on a steel cable and is attached to a sled that guides it along a vertical Bosch-profile. On top, the cable runs over a pulley wheel and then is attached to a hand winch that is mounted on a small table. By turning the crank, the height of the collimator can be adjusted. Once the height is decided, the collimator is fixed to the profile. The setup is displayed in figure 43 (b).

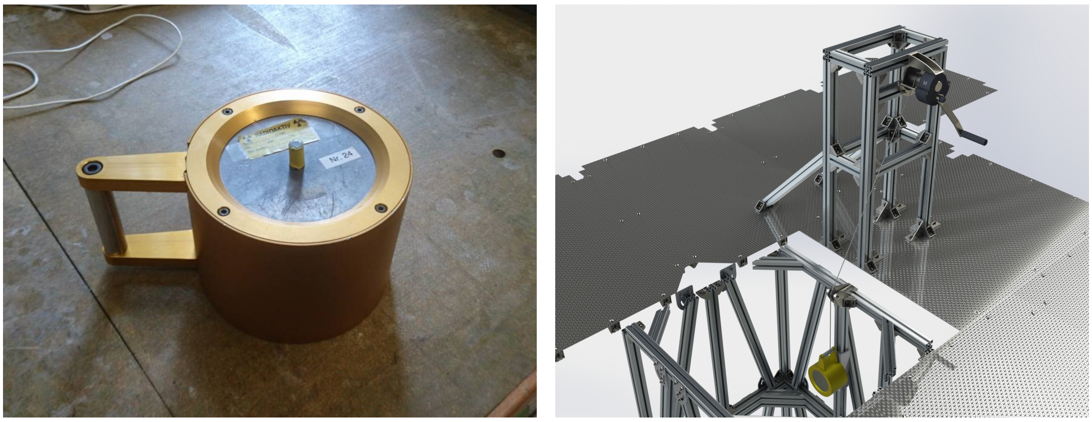

(a) (b)

Figure 43: (a): Picture of the collimator used for this project. (b): Render of the top part of the collimation setup designed with SolidWorks. In the proposed but not yet built setup, the Xenoscope cryostat would sit in front of the collimator and was hidden in the render for a better view.

After designing, the setup was implemented in the Geant4 framework in order to obtain a realistic simulation, as shown in figure 44. With this setup, the energy deposition takes place in a narrow z position window with a standard deviation of $\sigma = 6\,\mathrm{mm}$ as can be seen in figure 37. The simulations were made with the collimator hanging at medium height. It was assumed that the amount of deposited energy does not depend on the z position because the amount of material the radiation has to cross does not substantially vary over the range of the TPC height.

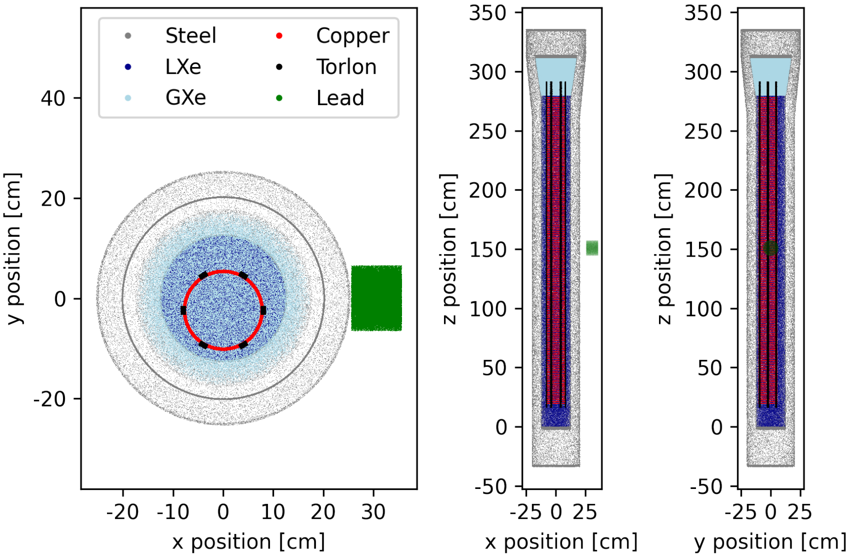

Figure 44: Geantino visualization of the TPC with the collimator in green. The collimator is placed according to the designed setup above and is fixed at medium height.

5 Analysis and Results

The goal of the analysis was to determine the background rate in the detector and to find out which of the potential calibration sources, described in the previous chapter, can be used in the DARWIN Demonstrator. This means that for all calibration sources it has to be calculated which activity would be needed to obtain a significant signal over the background in a reasonable amount of time.

In this chapter, first, it is described how the simulated events of the background and calibration sources were analyzed. Then the results of this procedure are shown for all considered calibration sources.

5.1 Analysis of Simulated Events

All simulated files of the background and the calibration source events were processed in the same way. First, for every event, it was checked if an interaction in the liquid xenon took place. If that was the case, it was further investigated if the energy deposition was located inside the active volume of the detector. The active volume was defined as the volume inside the field shaping rings between the lowest ring and the liquid xenon level as shown in figure 45.

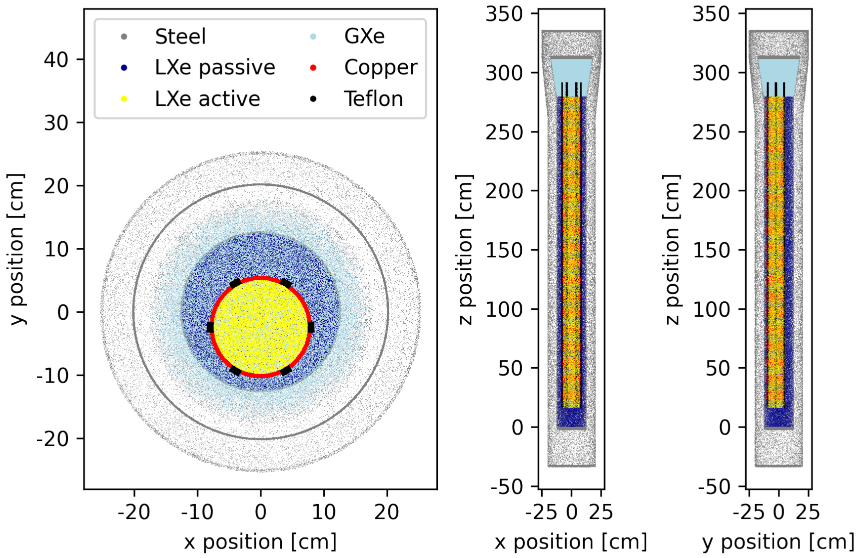

Figure 45: Geantino visualization of the detector with the selected active volume shown in yellow. It is defined as the entire volume inside the field cage. In the data analysis most likely a smaller fiducial volume will be selected. However, its exact shape is usually determined by background data and is therefore not known yet.

If the energy depositions happened within 1 μs, the energy was summed up because the detector will not be able to resolve such short time differences. This is because in Xenoscope only the S2 charge signals will be measured, which broaden with increasing drift time due to the diffusion of the electron clouds. The with of the S2 signal, σ, can be estimated from the diffusion model [132]:

$$\sigma = \sqrt{\frac{D_L 2t}{v_d^2} + \sigma_0}. \tag{5.1}$$

Here D_L is the longitudinal diffusion coefficient, t is the drift time, and v_d is the drift velocity. σ_0 is the initial spread of the signal ($\mathcal{O}$(100 ns) [133]) which is negligible for long drift times. $D_L \simeq$ 50 cm^2/s depends on the xenon temperature and pressure as well as on the drift field [132]. Taking the nominal values for Xenoscope, $t =$ 1.75 ms and $v_d =$ 1.5 mm/μs for a drift field of 200 V/cm [5], equation 5.1 yields an S2 with of $\mathcal{O}$(1 μs). No spatial resolution in the x-y plane was taken into account because this parameter of the detector is still unknown. After this clustering process, the deposited energies of the background components and calibration sources were histogrammed. The result of this procedure can be found in figure 46. The spectra are in arbitrary units because the normalization will be done in a following step.

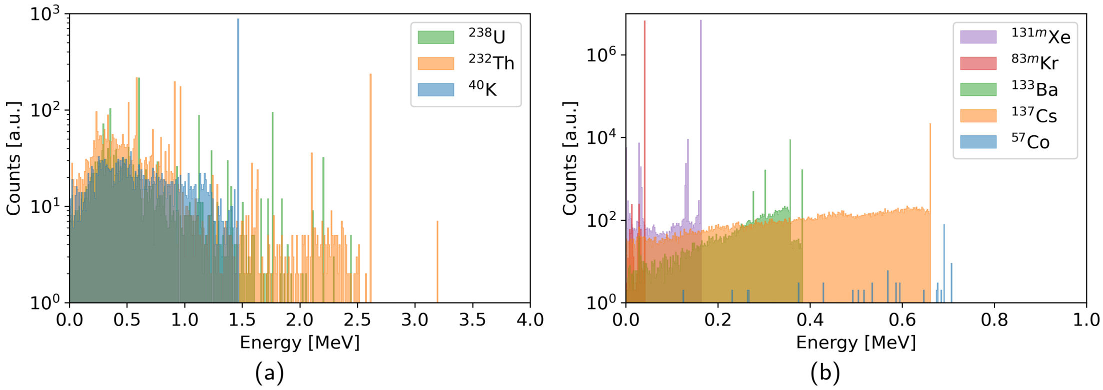

Figure 46: (a): Histogrammed energy deposition inside the TPC for 10^6 simulated events of each of the three considered background components. (b): Histogrammed energy deposition in the TPC for 2×10^8 simulated events of each of the three external calibration sources and 2×10^7 events of the internal calibration sources ^{83m}Kr and ^{131m}Xe. ^{220}Rn is not shown in this plot because the energy deposition goes up to 9 MeV. For the internal sources it can be seen that there are events to the left of the peaks. They typically originated near the edge of the active volume and did not deposit their whole energy inside of it. For the external sources a similar feature can be observed. Here the events have lost part of their energy before reaching the active volume and therefore only deposit a fraction of the total decay energy inside of it.

So far, the analysis assumed an infinitely good energy resolution which is of course not the case in reality. Unfortunately, the attainable energy resolution is still unknown. Therefore, as an estimate, the combined energy scale of the XENON1T experiment was taken [134], shown in figure 47 (a). This energy resolution as function of recoil energy E_r can also be written as

$$\sigma(E_r)/\mu(E_r) = a/\sqrt{E_r} + b, \tag{5.2}$$

where $a = 31.3 \pm 0.7$ and $b = 0.17 \pm 0.02$. Every bin of the histogram was then smeared out to a Gaussian function according to the energy resolution at that energy, to get a realistic spectrum. This is shown in figure 47 (b) on the example of the ^{232}Th background.

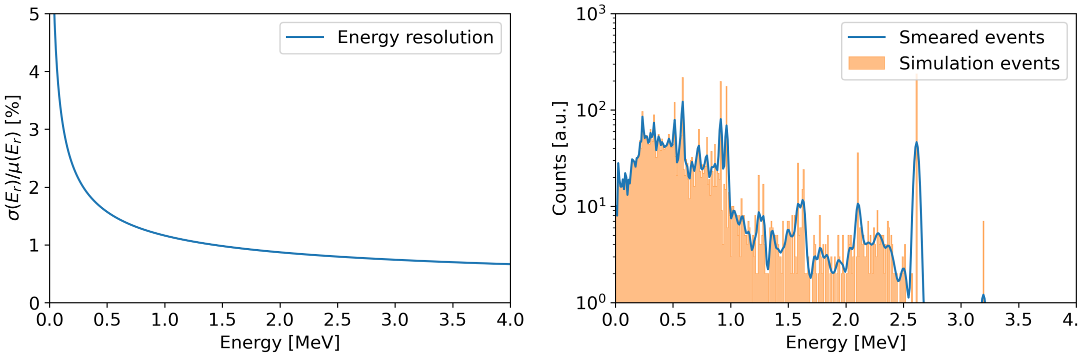

(a) (b)

Figure 47: (a): Energy resolution of the XENON1T experiment, figure based on [134]. (b): Smearing of the energy depositions in the TPC according to the energy resolution on the example of the ^{232}Th chain events. The smeared-out curve is plotted in blue while the initial energy deposition histogram is shown in orange. It can be seen that even though the relative energy resolution improves at higher energies, the absolute width of the peaks increases.

5.1.1 Background Events

In the case of the simulated background events, the energy spectra of the three background components had to be scaled according to the corresponding measured rates. This was done by first dividing the counts at each energy $N_{Counts}(E)$ of the spectrum by the total amount of simulated decays N_{hit} of the respective isotope, defined in section 4.3.3, such that the energy deposition was normalized per event. Now the spectrum could be scaled up to the rate of particles, R_D, hitting the cylinder around the Demonstrator. R_D was calculated in section 4.3.1 from the measured rates using a geantino simulation, and accounts for the geometrical acceptance of the cylinder. Finally, the background rate was divided by the mass of the active liquid xenon, m_{Xe} = 145.8 kg (total 371.4 kg in the Geant4 simulation), and the width of the used bins, d_{bin} = 1 keV, in the histogram. This was done in order to turn it independent of the amount of xenon and the used binning, and thus make it comparable to background rates of other experiments. The whole formula for the background rate $R_{Background}(E)$ in each energy bin reads

$$R_{Background}(E) = N_{Counts}(E) \cdot \frac{R_D}{N_{hit}} \cdot \frac{1}{m_{Xe} \cdot d_{bin}}. \tag{5.3}$$

The result of the whole procedure together with the contributions from the individual background components for the top measurement is shown in figure 48 (a). The full resulting background spectra scaled according to the two measurements on the top and at the bottom can be compared in figure 48 (b). The average integrated background rate of the two measurements in the entire energy range is (90 ± 30) Hz.

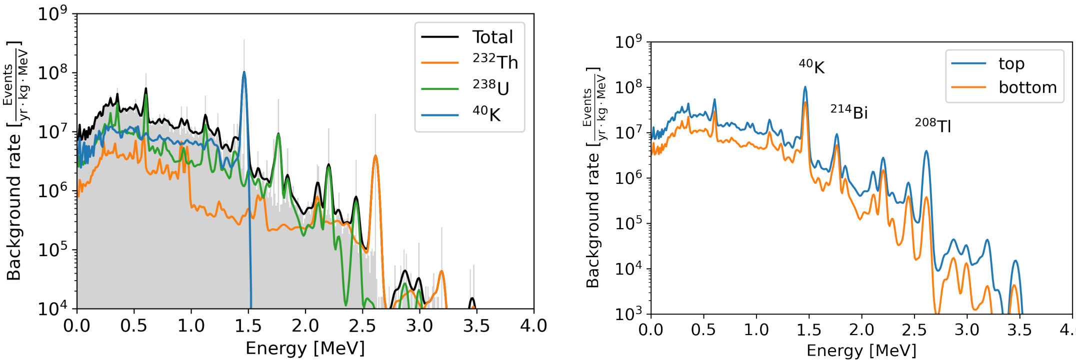

(a) (b)

Figure 48: (a): The full background rate scaled according to the measurement on top of the Demonstrator is shown in black, with the underlying histogram before the smearing in grey. The contributions of the individual background components are shown by the colored lines. (b): Comparison of the background rates resulting from scaling according to the top and bottom measurement. The discrepancy originates from the different measured rates of the background components on top and bottom.

5.1.2 Calibration Source Events

In the case of the simulated calibration source events, the smeared out histogrammed energy deposition in the active liquid xenon, $N_{Counts}(E)$, had to be scaled according to the source activity A. However, the needed activity for the calibration was not yet known. Therefore, the scaling was performed according to 200 different source activities, evenly distributed over a wide range such that later, the minimal required activity could be identified. Apart from that, the scaling was performed analogous to the background simulation data, according to the formula

$$R_{Source}(E) = N_{Counts}(E) \cdot \frac{A}{N_{hit}} \cdot \frac{1}{d_{bin}}. \tag{5.4}$$

Here N_{hit} is the number of simulated events of the respective isotope. Note that the rate was not normalized to the liquid xenon mass because there is no point in comparing these values to other experiments. Finally, the peaks that can be used for the calibration were selected and fitted with a Gaussian function to know their position and width. The result of this procedure is shown on the example of the ^{137}Cs source in figure 49 (a).

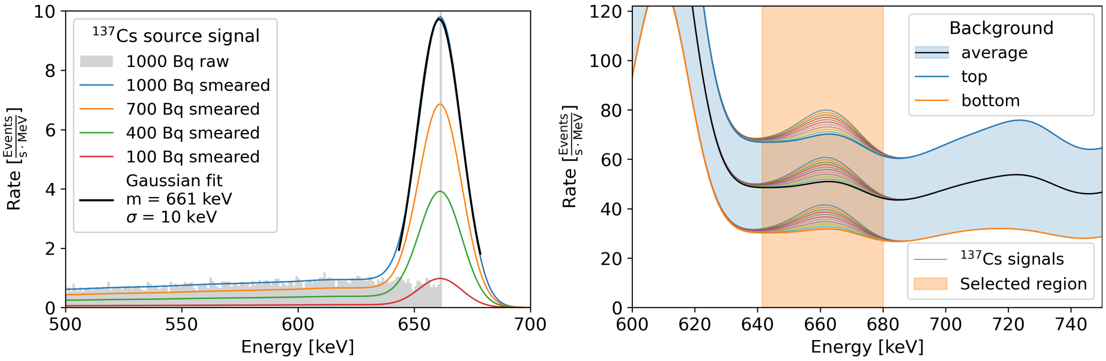

(a) (b)

Figure 49: (a): Smeared out energy deposition curves for different ^{137}Cs source activities. For clarity, only four of the 200 activities are shown. Additionally, the histogrammed energy deposition of the 1 kBq source is displayed in grey. The 661.7 keV peak was fitted with a Gaussian for the following analysis. (b): ^{137}Cs source signal for 10 source activities from 100 Bq to 1000 kBq, combined with the simulated background scaled according to the measurements on top and bottom of the Demonstrator as well as their average. The selected 2σ region where the events are counted is shaded in orange.

5.1.3 Combined Analysis

Next, the calibration source signal had to be compared to the background spectrum. To this end, the background spectrum was integrated over the total mass of the active liquid xenon in order to match the units. Then, a region of two σ around the mean of the calibration γ-line was selected based on the Gaussian fit. Afterwards, the number of background events per second in this region, N_{B_0}, was counted for the background scaled according to the top and bottom measurements as well as for their average. Also, the number of calibration source events per second in the same region, N_{S_0}, was counted for all considered source activities. The procedure is illustrated in figure 49 (b) again using as an example the ^{137}Cs source. Then, N_{B_0} and N_{S_0} were multiplied by the exposure time, t_{exp}, to arrive at the absolute number of background events, N_B, and calibration source events, N_S. This was done for 300 different exposure times evenly distributed between zero and the maximum reasonable exposure for data taking. For internal sources this was taken to be 48 h while for external sources a limit of 6 h was chosen such that several calibration runs at different heights can be performed. Finally, the significance, S, of the peak above the background was calculated for all source activities, exposure times, and the background scaled according to the top and bottom measurement, as well as their average. This was done using the formula

$$S = \frac{N_S}{\sqrt{N_B}} = \frac{N_{S_0}\sqrt{t_{exp}}}{\sqrt{N_{B_0}}} \text{ since } N_{S(B)} = N_{S_0(B_0)} \cdot t_{exp}. \tag{5.5}$$

The results of this procedure are displayed by plotting the 1σ, 3σ and 5σ contour lines in the two dimensional significance space spanned by the source activities and exposures. Additionally, each contour line is enveloped in a region that represents the systematic error, which is taken as the contour line according to the top and bottom measurements respectively. Such a plot, again on the example of the 661.7 keV peak of ^{137}Cs, can be seen in figure 50.

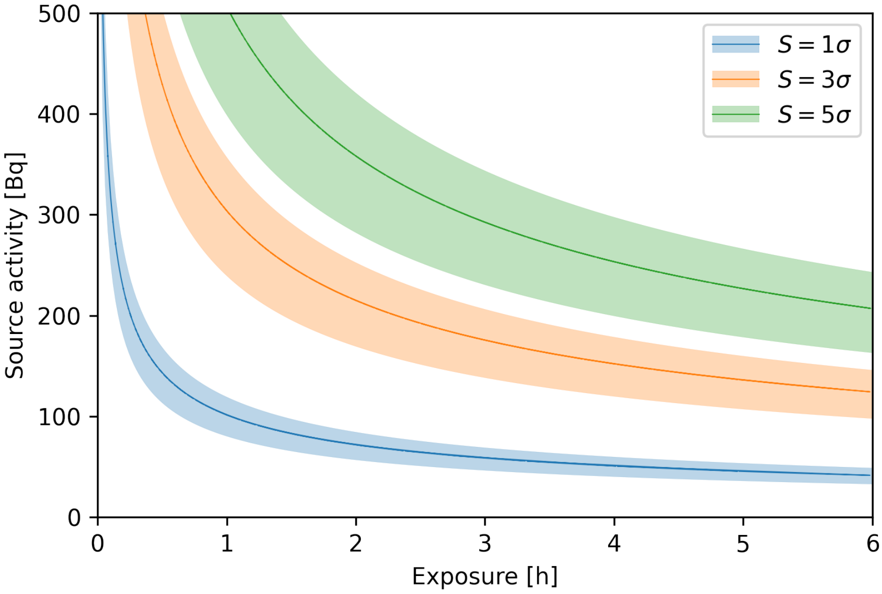

Figure 50: Resulting significance, S, of the 661.7 keV γ-line of ^{137}Cs. The 1σ, 3σ and 5σ contour lines are plotted for the average background. The shaded region indicates the difference between scaling the background according to the measurements on top and bottom.

5.2 Results

In this section, the results of the procedure explained above are presented and discussed individually for all calibration sources. An overview of the energies of the analyzed γ-lines along with the expected background can be found in figure 51. The significance plots are not shown for all sources but they are included in the appendix in section 7.1.

^{83m}Kr

For ^{83m}Kr, only the line at 41.5 keV was analyzed. A ^{83m}Kr activity of about 6×10^{-5} Bq/kg is sufficient such that this peak can be seen with 5 σ significance above the background

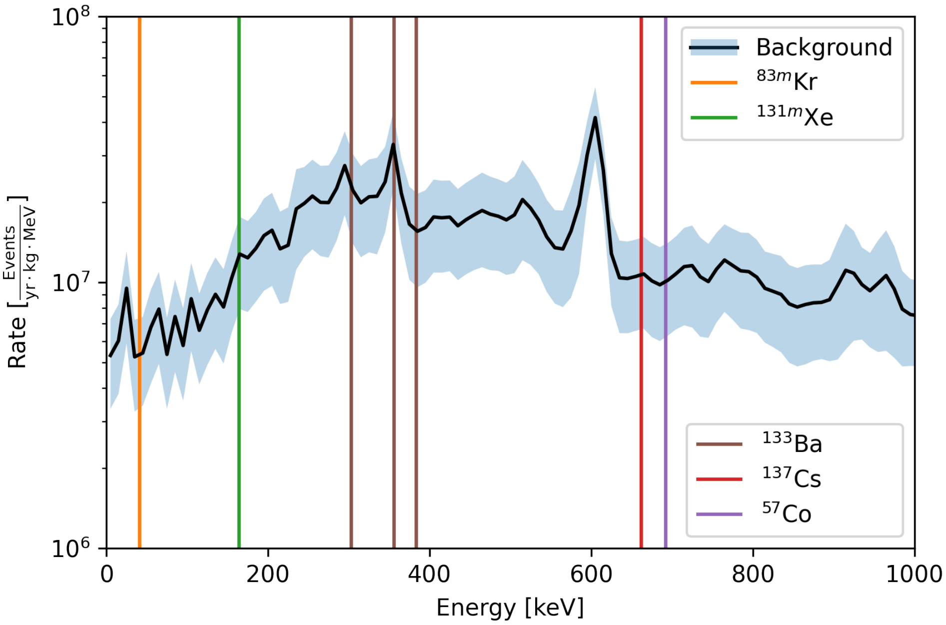

Figure 51: Energies of all analyzed γ-lines with the expected average background in black. The range between the background scaled according to the top and bottom measurements is shaded in blue.

within 48 h. The activity here is given per kg of liquid xenon. Summed up over the entire 371.4 kg of xenon in the cryostat, this corresponds to a total activity of 2.2×10^{-2} Bq. With the ^{83}Rb source available at the Physics Department of the University of Zurich, which has an activity of 7.45 kBq [1], this activity is clearly within reach. However, a calibration with ^{83m}Kr only is not enough, because solely the combined line at 41.5 keV will be visible, while the 32.1 keV and 9.4 keV lines will not be resolved separately due to insufficient time resolution as pointed out in section 4.4.

^{131m}Xe

For ^{131m}Xe, the only γ-peak at 163.9 keV was analyzed. A ^{131m}Xe activity of about 1.2×10^{-4} Bq/kg is sufficient such that this peak can be seen with 5 σ significance above the background within 48 h. The difference to the ^{83m}Kr comes from the enhanced background at the concerning energy. Summed up, this corresponds to an overall activity of 4.4×10^{-2} Bq. At the moment the Physics Department of the University of Zurich does not possess a ^{131}I source. However, a new source with the required activity can in principle be purchased since ^{131}I is commonly used in medical and industrial applications and is, therefore, commercially available. It has to be noted again that additional sources are needed to cover the entire energy range with the calibration.

---

[1] As of 03.11.2021.

^{220}Rn

In contrast to the two internal calibration sources above, ^{220}Rn is part of a decay chain. Therefore, the energy spectrum features several different α-, and γ-peaks, that need to be analyzed separately, as well as multiple overlapping β^--spectra. One has to note that ^{220}Rn is part of the ^{232}Th chain that also contributes to the radiogenic background. However, because the background radiation hits the detector from outside, all α-particles and electrons are absorbed in the steel walls of the outer and inner cryostat as well as the layer of liquid xenon around the TPC, leaving only the γ-peaks to contribute. For a calibration using α-peaks from an internal source this is very convenient because the background in their energy region above 5 MeV is very low, as clearly visible in figure 52. In fact, the background is so low that not a single event of the simulated background has an energy in the relevant region between 6 MeV and 7 MeV. However, internal background from ^{222}Rn, emanated form the steel walls, is expected in this energy region. For this reason, no significance and minimal activity can be calculated in the same way as for the other sources. In order to obtain the displayed signal in figure 52 after 48 h, a ^{220}Rn activity of roughly 1.8×10^{-5} Bq is theoretically sufficient.

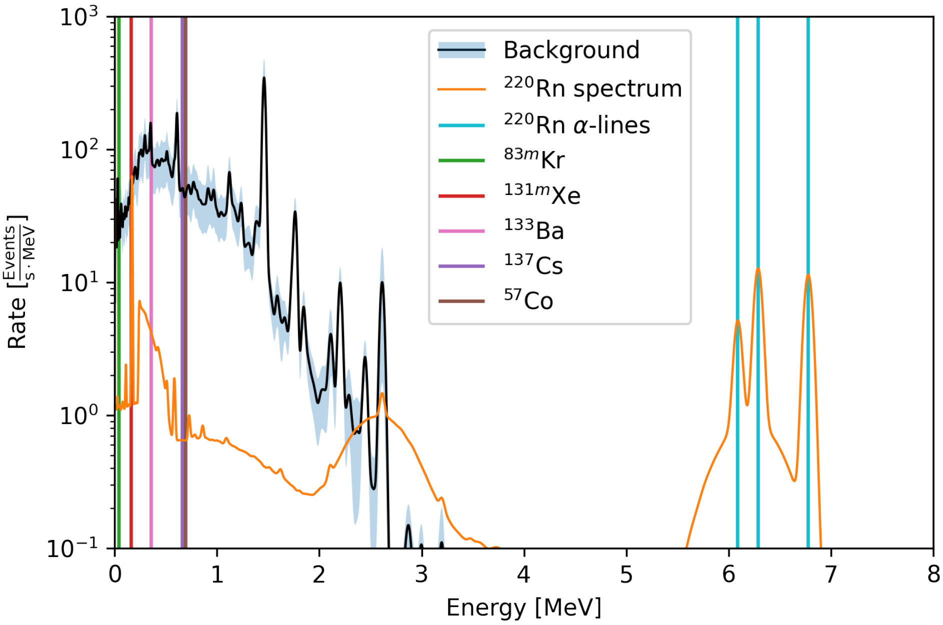

Figure 52: Energy spectrum of an internal ^{220}Rn source of 3 Bq with all following decays from the decay chain, compared to the averaged background. It can be seen that the high energy α-peaks are in a region with very low background. The underlying broad peak around 6 MeV comes from α-decays with low branching ratios.

For the γ-lines on the other hand, the peaks coincide with peaks in the background which makes the differentiation more difficult. Also, the peaks are less clearly visible because of the accompanying β-spectrum, which act as an additional background that scales with the source activity. Therefore, a low energy calibration using the γ-peaks of ^{220}Rn and the following decays is not feasible for the level of radiogenic background in Xenoscope.
At the moment the Physics Department of the University of Zurich does not possess a ^{220}Rn source. However, a calibration with the high energy α-lines of ^{220}Rn is possible and a new source with the required activity can in principle be purchased.

^{137}Cs

For ^{137}Cs, the γ-peak at 661.7 keV was analysed. A ^{137}Cs activity of about 2.5×10^2 Bq is sufficient such that this peak can clearly be seen above the background. The maximum time here was chosen to be 6 h because it should be possible to calibrate several times at different heights within a reasonable amount of time. The ^{137}Cs source available at the Physics Department of the University of Zurich has an activity of 236.37 kBq [2]. This is about three orders of magnitude higher than necessary. Therefore, using the 661.7 keV for the calibration is clearly possible, although again at least one other peak is needed for a calibration in the entire energy range.

^{57}Co

For ^{57}Co, only the γ-peak at 692.4 keV could be analyzed. Even though it has a low branching ratio of 0.15 %, it is the only peak that was visible in the energy spectrum inside the TPC of the simulated 2×10^8 events. The low energy γ-peaks at 136.4 keV, 122.1 keV, and 14.4 keV that all have higher branching ratios could not be found. These γ-rays get absorbed in the steel walls of the outer and inner cryostat, and the liquid xenon outside the TPC because of their low energy. A ^{57}Co activity of about 1.2×10^5 Bq would be needed such that the 692.4 keV peak reaches 5σ above background. The ^{57}Co source available at the Physics Department of the University of Zurich has an activity of 2.41 kBq [2] which is not enough for a calibration. In principle, new ^{57}Co sources with an activity in the order of MBq could be bought. However, since only the 692.4 keV γ-line can be used that has nearly the same energy as the main ^{137}Cs line but a 570 times smaller branching ratio, this would not be a requirement for the calibration.

^{133}Ba

For ^{133}Ba, three γ-peaks were analysed, namely the ones at 356.0 keV, 302.9 keV and 383.8 keV. Similarly to the low energy ^{57}Co peaks, the ^{133}Ba γ-peak at 81.0 keV was not found in the energy deposition spectrum. The peak at 356.0 keV has the highest branching ratio of about 62 %. A ^{133}Ba activity of about 1.5 kBq is sufficient such that this peak can clearly be seen above the background. The ^{133}Ba source available at the Physics Department of the University of Zurich has an activity of 1.84 kBq [2] which is enough for a calibration with this peak

---

[2] As of 03.11.2021.

The two other considered peaks have lower branching ratios, therefore a higher activity of about 7 kBq is needed for an additional calibration with those two peaks. This would in principle be possible with a new source. On the downside, the three peaks are located very close to each other which makes the result dependent on the energy resolution. For example, the two higher energetic γ-lines both have a width of $\sigma = 7$ keV by a separation of 27.8 keV. This makes the corresponding 2σ regions almost touch each other. Moreover, since the branching ratio of the 383.8 keV line is only about 9 %, events from the high energy tail of the 356.0 keV peak already significantly contribute at the low energy edge of its 2σ region. For this reason, an area of only 1.5σ around the peak was considered in the corresponding analysis. In case the energy resolution is not as good as expected, the two peaks would further merge and could hence not be separated anymore.

Radiation Load in the Detector Environment

With the calculated required activities above, for all considered calibration sources the radiation load in the vicinity of the detector does not come close to a critical magnitude, for various reasons: The calculated required activities of the external sources are well below the maximum activity the collimator is able to shield ($\mathcal{O}$(MeV)). Of the internal sources, ^{83m}Kr and ^{133m}Xe deposit almost all of their energy within the detector and only very few γ-rays with low branching ratios escape. This is not the case for ^{220}Rn and its follow-up decays which feature also higher energetic γ-lines, as for example the 2.6 MeV line of ^{208}Tl. However, because the background in the relevant energy region for a calibration with the ^{220}Rn α-lines is close to zero, the needed activity is well below a harmful level. Consequently, the work of calibrating Xenoscope will be safe. Nevertheless, a dosimeter should be worn at all times for this task.

6 Conclusion

Summary

Despite tremendous efforts of scientist all around the globe performing a variety of experiments, the nature of dark matter and some properties of neutrinos remain mysteries up to this date. To address these open questions, DARWIN, envisaged as the ultimate dark matter detector, containing 50 t of liquid xenon in an about 3 m high and wide cryostat, will be built. However, since it will be the first dual-phase xenon TPC of this magnitude, extensive R&D work is still necessary before DARWIN can be realised. A crucial step in this process is the design, construction, and commissioning of Xenoscope, the first dual-phase xenon TPC with the full 2.6 m high drift region of DARWIN.

This work was dedicated to background studies and calibration source simulations for Xenoscope. The radiogenic background environing the experiment was measured with an NaI(Tl) detector and the activities of the three main background components were determined (^{40}K, ^{232}Th, and ^{238}U). Based on these findings, a background model for the detector was developed by means of Monte Carlo simulations. The resulting background energy spectrum showed that a calibration using γ-peaks from the background is possible at energies between roughly 1.5 MeV and 2.5 MeV.

Furthermore, the signals of different calibration sources were simulated and it was checked whether they can be used for calibration. Of the tested internal sources, ^{83m}Kr and ^{131m}Xe were shown to be applicable for a calibration at low energies using their lines at 41.5 keV and 163.9 keV respectively. At high energies, ^{220}Rn and its follow-up decays can be used for a calibration using the α-lines above 6 MeV. However, as a drawback it was found that this source introduces an additional background at low energies. For the external sources, in addition to the simulations, a setup was designed that allows for a safe and convenient calibration at different heights along the full extent of Xenoscope. The geometry of this setup was implemented in the Geant4 framework for the simulations. Of the three considered external calibration sources, ^{137}Cs and ^{133}Ba were shown to be viable for a calibration at 661.7 keV and around 356.0 keV respectively. The energy calibration data can in their case also be used for a measurement of the electron live-time and xenon purity in the detector, complementary to the one of the purity monitor.

Discussion of Results

The measurement of the radiogenic background at the location of Xenoscope yielded an integrated rate inside the detector of (90 ± 30) Hz, that is about one order of magnitude lower than previously estimated by simply scaling up the measured background of the Xurich-II detector. The discrepancy could arise for example from varying concrete activities since the Xurich-II experiment is located in a different lab in the building. In the end, crosschecking all steps produced consistent results and the main uncertainty in the measurements comes from the intrinsic background of the NaI(Tl) detector.

In the case of the simulations, the main uncertainties were the unknown energy and time resolution of the detector. For the time resolution, 1 µs was assumed, which is in the order of the width of the S2 signals after drifting for 1.75 ms through the 2.6 m high TPC. With a total background rate of about 90 Hz and the calculated necessary calibration source activities no pile up problems are expected to arise. For the energy resolution, the same values as in XENON1T were assumed, which is about 5% at the ^{83m}Kr energy and about 1% in the MeV range. Considering that in Xenoscope only S2 signals will be measured but no S1 signals, this is a quite optimistic assumption. A study from XENON100 showed that the S2 only resolution is significantly worse than the resolution of the combined energy scale, as shown in figure 53.

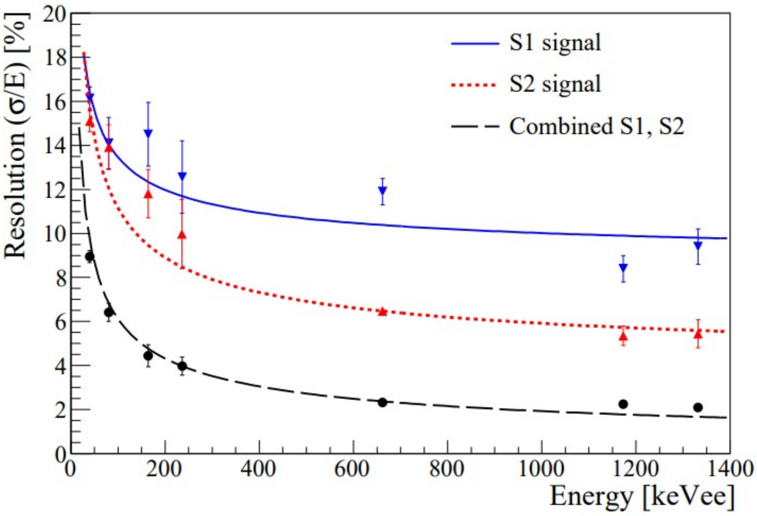

Figure 53: Energy resolution of the XENON100 experiment using only the S1 (blue) or S2 (red) signal and their combination (black). In more recent experiments the S1 only resolution strongly improved due to a better light collection efficiency and is now better than the S2 only resolution. Figure from [135].

For the background rate at a given energy, a worse energy resolution would not drastically change the result but only lead to a slight smearing-out of the peaks. However, the energy resolution is of importance for the study of the calibration sources: When the energy resolution is worse than expected, the number of signal events within the enlarged 2σ region remains the same while the number of background events scales up approximately linearly with the width of the selected window. Looking at formula 5.5 for the significance S, one can see that if the resolution changes by a factor of f, the significance drops according to $1/\sqrt{f}$. To reach the same significance as with the assumed resolution in this work, the measurement time has to be prolonged by the same factor f as can easily be calculated:

$$S' = \frac{N_{S_0}\sqrt{t'_{exp}}}{\sqrt{N'_{B_0}}} = \frac{N_{S_0}\sqrt{t_{exp}\cdot x}}{\sqrt{N_{B_0}\cdot f}} \overset{!}{=} S = \frac{N_{S_0}\sqrt{t_{exp}}}{\sqrt{N_{B_0}}} \rightarrow x = f. \tag{6.1}$$

In this formula, the primed variables belong to a measurement with an energy resolution differing by a factor f from the assumptions, which has to be prolonged by an initially unknown factor x to reach the same required significance, S. N_{S_0} and N_{B_0} are the number of signal and background events in the selected 2σ region per second respectively and t_{exp} is the measurement time. It can be seen that alternatively, instead of prolonging the measurement, a source with an activity enhanced by a factor of $\sqrt{f}$ can be used.

Outlook

The Xenoscope facility was successfully commissioned at the beginning of 2021. The subsystems including the gas system, cryogenics, and storage system were tested and the cryostat was filled with 80 kg of liquid xenon. The first stage of the DARWIN Vertical Demonstrator with the purity monitor is ongoing with the datataking about to start. Until Xenoscope runs with the full height TPC roughly another year will pass. It is at this stage, when a calibration of the TPC will be done and the results of this work will be of great value. At this point, an ongoing study of the cosmogenic background will also be finished and the muons crossing Xenoscope will be measured using scintillator panels.

Now that the background from the concrete walls is not as high as expected, it could be interesting to look into the background from the materials used to build the detector. This background is anticipated to be small for two reasons. On one hand, the cryostat was already mounted at the time when the measurement was performed. The NaI(Tl) measurement, close to the cryostat, did not yield a very high activity. On the other hand, the usually most problematic components, PTFE and PMTs, are not present in the detector. Either way, an exact simulation of this background was out of the scope of this thesis and it is not possible at this point because the radioactivity of the steel, and also other components, is not known.

Once Xenoscope has completed its mission of drifting electrons over 2.6 m, the facility will be available for other R&D projects for DARWIN. The construction of DARWIN detector itself tentatively will start in 2024. It is planned to be commissioned and filled with liquid xenon for the first time in 2026 and will start its operation in 2027. It will then run for several years to hopefully reach its goals of directly detecting dark matter and shining light on the nature of neutrinos themselves, as well as their sources. The full timeline of the DARWIN project can be found in figure 54.

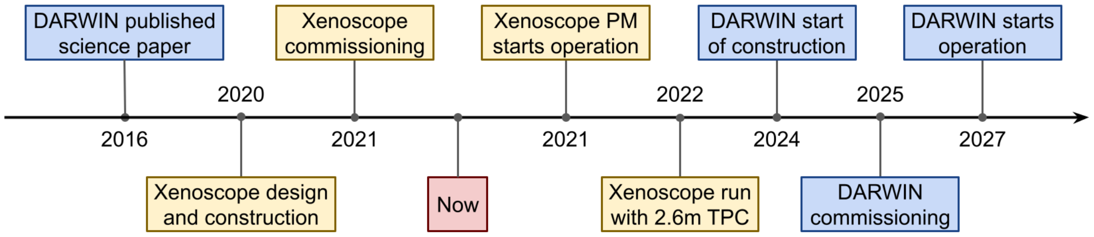

Figure 54: Timeline of the Darwin experiment and its R&D project Xenoscope.

7 Appendix

7.1 Significance Plots

^{83m}Kr

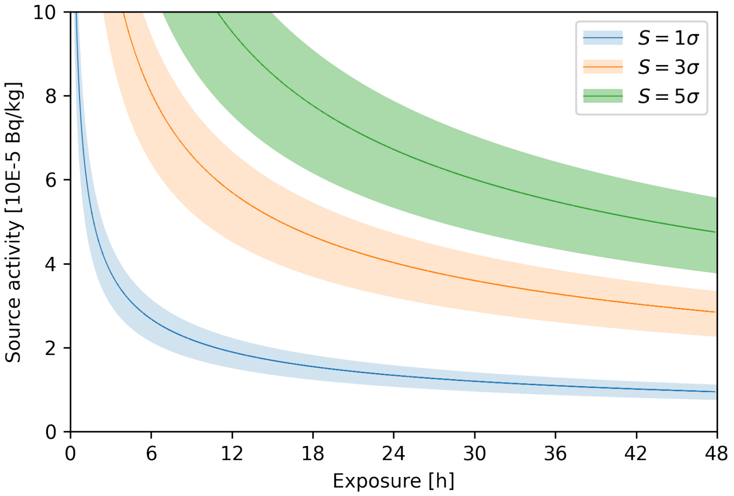

Figure 55: Resulting significance contour lines of the 41.5 keV γ-line of ^{83m}Kr.

^{131m}Xe

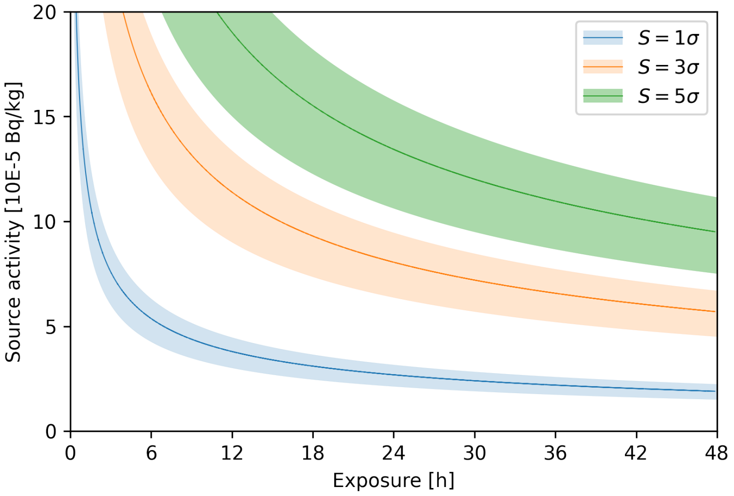

Figure 56: Resulting significance contour lines of the 163.9 keV γ-line of ^{131m}Xe.

^{57}Co

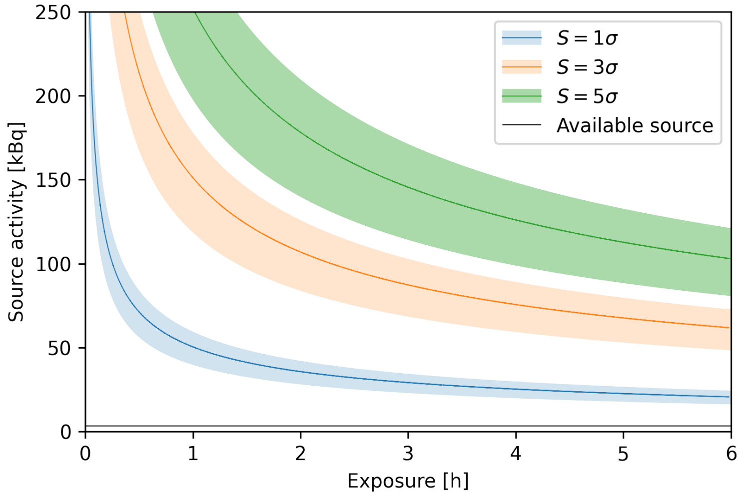

Figure 57: Resulting significance contour lines of the 692.4 keV γ-line of ^{57}Co. The activity of the available source at the Physics Department of the University of Zurich is shown by the black horizontal line.

^{133}Ba

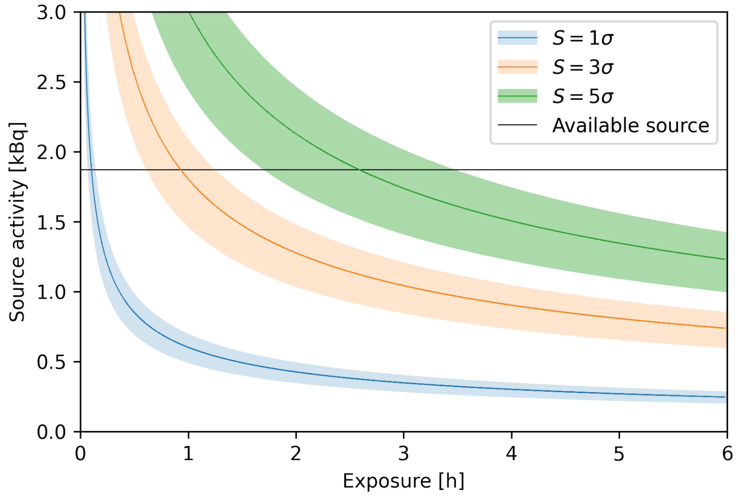

Figure 58: Resulting significance contour lines of the 356.0 keV γ-line of ^{133}Ba. The activity of the available source at the Physics Department of the University of Zurich is shown by the black horizontal line.

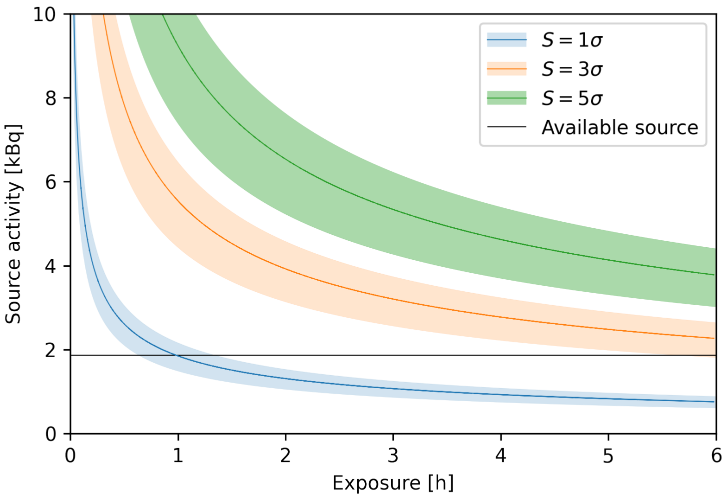

(a)

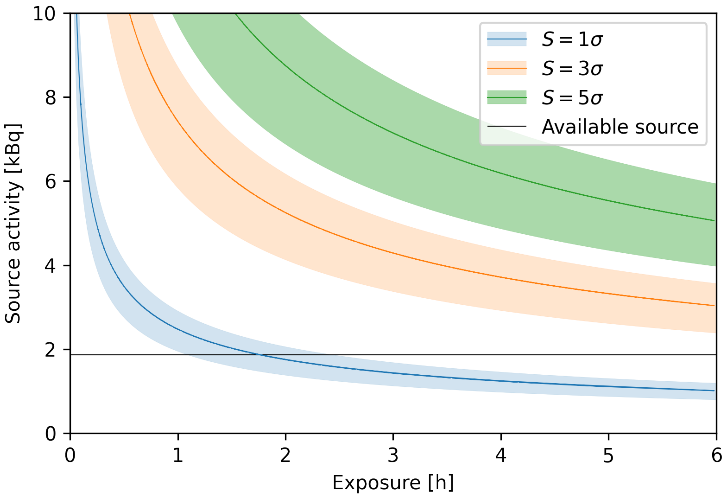

(b)

Figure 59: Resulting significance contour lines of the (a): 302.9 keV and (b): 383.8 keV γ-lines of ^{133}Ba. The activity of the available source at the Physics Department of the University of Zurich is shown by the black horizontal line.

7.2 Picture of the DARWIN Vertical Demonstrator

Figure 60: Picture of the DARWIN Demonstrator with its support structure in the assembly hall.

7.3 ^{220}Rn and Follow-up Decay Schemes

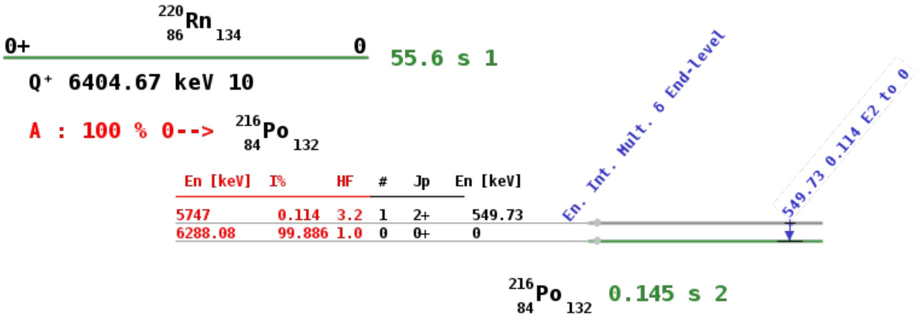

(a)

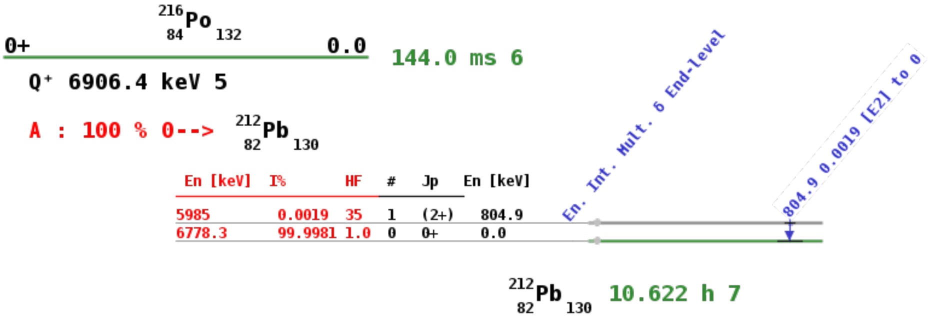

(b)

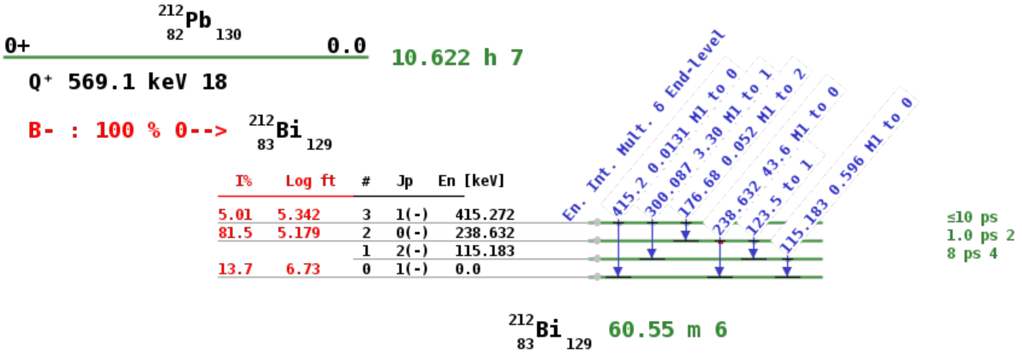

(c)

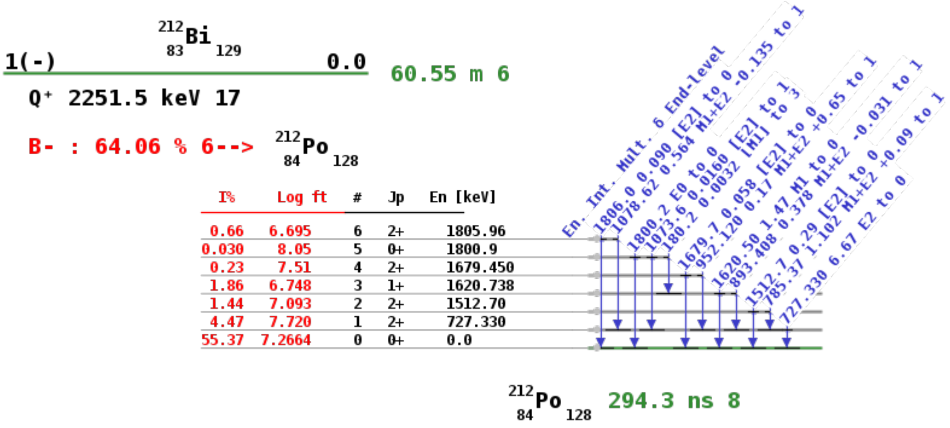

I%	Log ft	#	Jp	En [keV]
0.66	6.695	6	2+	1805.96
0.030	8.05	5	0+	1800.9
0.23	7.51	4	2+	1679.450
1.86	6.748	3	1+	1620.738
1.44	7.093	2	2+	1512.70
4.47	7.720	1	2+	727.330
55.37	7.2664	0	0+	0.0

(d)

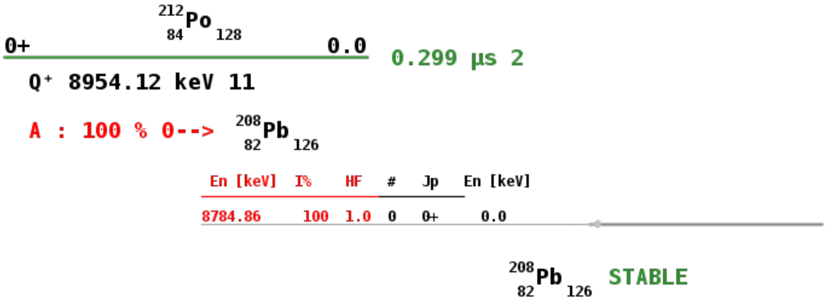

En [keV]	I%	HF	#	Jp	En [keV]
8784.86	100	1.0	0	0+	0.0

(e)

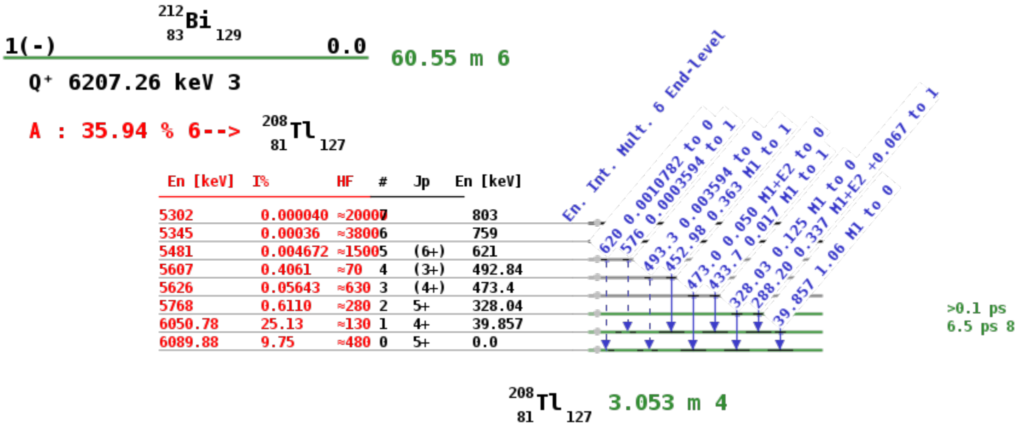

En [keV]	I%	HF	#	Jp	En [keV]
5302	0.000040	≈20000	7		803
5345	0.00036	≈3800	6		759
5481	0.004672	≈1500	5	(6+)	621
5607	0.4061	≈70	4	(3+)	492.84
5626	0.05643	≈630	3	(4+)	473.4
5768	0.6110	≈280	2	5+	328.04
6050.78	25.13	≈130	1	4+	39.857
6089.88	9.75	≈480	0	5+	0.0

(f)

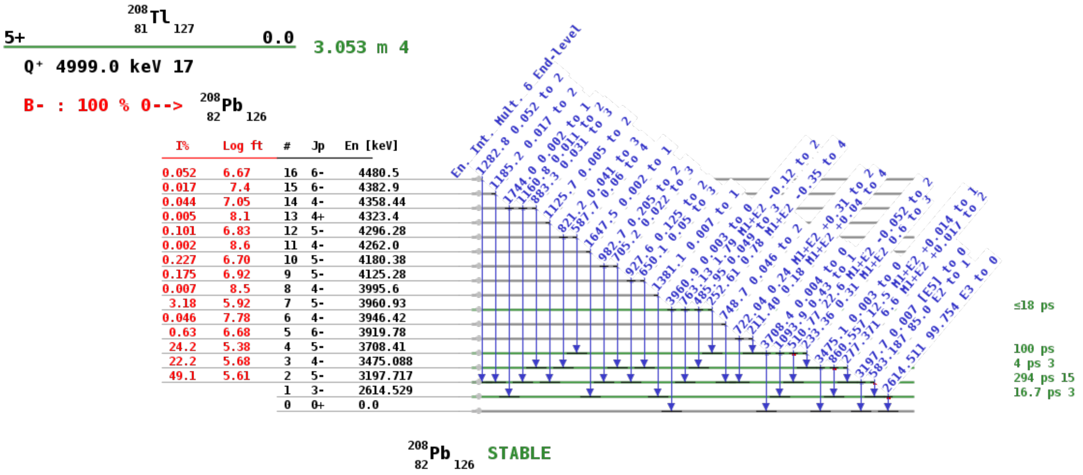

I%	Log ft	#	Jp	En [keV]
0.052	6.67	16	6-	4480.5
0.017	7.4	15	6-	4382.9
0.044	7.05	14	4-	4358.44
0.005	8.1	13	4+	4323.4
0.101	6.83	12	5-	4296.28
0.002	8.6	11	4-	4262.0
0.227	6.70	10	5-	4180.38
0.175	6.92	9	5-	4125.28
0.007	8.5	8	4-	3995.6
3.18	5.92	7	5-	3960.93
0.046	7.78	6	4-	3946.42
0.63	6.68	5	6-	3919.78
24.2	5.38	4	5-	3708.41
22.2	5.68	3	4-	3475.088
49.1	5.61	2	5-	3197.717
		1	3-	2614.529
		0	0+	0.0

(g)

Figure 60: Decay plots of the ^{220}Rn source with the following decays from the ^{232}Th decay chain. Figures plotted with [128] based on data from [115].

Bibliography

[1] F. Zwicky. "Die Rotverschiebung von extragalaktischen Nebeln". In: *Helvetica physica acta* 6 (1933), pp. 110–127.

[2] P. A. Zyla et al. "Review of Particle Physics". In: *PTEP* 2020.8 (2020), p. 083C01. DOI: `10.1093/ptep/ptaa104`.

[3] E. Aprile et al. "Dark Matter Search Results from a One Ton-Year Exposure of XENON1T". In: *Phys. Rev. Lett.* 121.11 (2018), p. 111302. DOI: `10/gd596b`. eprint: `1805.12562`.

[4] J. Aalbers, F. Agostini, M. Alfonsi, et al. "DARWIN: towards the ultimate dark matter detector". In: *Journal of Cosmology and Astroparticle Physics* 2016.11 (2016), p. 017.

[5] L. Baudis et al. "Design and construction of Xenoscope - a full-scale vertical demonstrator for the DARWIN observatory". In: *Journal of Instrumentation* 16.08 (Aug. 2021), P08052. ISSN: 1748-0221. DOI: `10.1088/1748-0221/16/08/p08052`.

[6] S. Agostinelli et al. "Geant4 - a simulation toolkit". In: *Nuclear Instruments and Methods in Physics Research Section A: Accelerators, Spectrometers, Detectors and Associated Equipment* 506.3 (2003), pp. 250–303. DOI: `10.1016/S0168-9002(03)01368-8`.

[7] J. Billard, M. Boulay, et al. *Direct Detection of Dark Matter – APPEC Committee Report*. 2021. arXiv: `2104.07634`.

[8] V. C. Rubin, W. Kent Ford Jr., and N. Thonnard. "Extended rotation curves of high-luminosity spiral galaxies. IV-Systematic dynamical properties, SA through SC". In: *The Astrophysical Journal* 225 (1978), pp. L107–L111.

[9] K. G. Begeman, A. H. Broeils, and R. H. Sanders. "Extended rotation curves of spiral galaxies: Dark haloes and modified dynamics". In: *Monthly Notices of the Royal Astronomical Society* 249.3 (1991), pp. 523–537.

[10] *Astronomy Picture of the Day (APOD) by Nasa.* Accessed: 27.09.2021. URL: `https://apod.nasa.gov/apod/ap170115.html`.

[11] D. Clowe et al. "A direct empirical proof of the existence of dark matter". In: *The Astrophysical Journal Letters* 648.2 (2006), p. L109.

[12] A. A. Penzias and R. W. Wilson. "A measurement of excess antenna temperature at 4080 Mc/s." In: *The Astrophysical Journal* 142 (1965), pp. 419–421.

[13] W. Hu and S. Dodelson. "Cosmic Microwave Background Anisotropies". In: *Annual Review of Astronomy and Astrophysics* 40.1 (2002), pp. 171–216. DOI: `10.1146/annurev.astro.40.060401.093926`.

[14] N. Aghanim et al. "Planck 2018 results". In: *Astronomy & Astrophysics* 641 (Sept. 2020), A6. ISSN: 1432-0746. DOI: `10.1051/0004-6361/201833910`.

[15] R. Adam et al. “Planck 2015 results”. In: *Astronomy & Astrophysics* 594 (Sept. 2016), A1. ISSN: 1432-0746. DOI: `10.1051/0004-6361/201527101`.

[16] N. Aghanim et al. “Planck 2018 results”. In: *Astronomy & Astrophysics* 641 (Sept. 2020), A1. ISSN: 1432-0746. DOI: `10.1051/0004-6361/201833880`.

[17] G. Jungman, M. Kamionkowski, and K. Griest. “Supersymmetric dark matter”. In: *Physics Reports* 267.5 (1996), pp. 195–373. ISSN: 0370-1573. DOI: `https://doi.org/10.1016/0370-1573(95)00058-5`.

[18] A. D. Sakharov. “Violation of CP invariance, C asymmetry, and baryon asymmetry of the universe”. In: *Journal of Experimental and Theoretical Physics Letters* 5 (1967), 24–27.

[19] J. H. Christenson et al. “Evidence for the 2π Decay of the K_2^0 Meson”. In: *Phys. Rev. Lett.* 13 (4 July 1964), pp. 138–140. DOI: `10.1103/PhysRevLett.13.138`.

[20] K. Abe et al. “Constraint on the matter–antimatter symmetry-violating phase in neutrino oscillations”. In: *Nature* 580.7803 (Apr. 2020), 339–344. ISSN: 1476-4687. DOI: `10.1038/s41586-020-2177-0`.

[21] C. Abel et al. “Measurement of the Permanent Electric Dipole Moment of the Neutron”. In: *Phys. Rev. Lett.* 124 (8 Feb. 2020), p. 081803. DOI: `10.1103/PhysRevLett.124.081803`.

[22] R. D. Peccei and H. R. Quinn. “CP Conservation in the Presence of Pseudoparticles”. In: *Phys. Rev. Lett.* 38 (25 June 1977), pp. 1440–1443. DOI: `10.1103/PhysRevLett.38.1440`.

[23] L. D. Duffy and K. v. Bibber. “Axions as dark matter particles”. In: *New Journal of Physics* 11.10 (Oct. 2009), p. 105008. DOI: `10.1088/1367-2630/11/10/105008`.

[24] K. N. Abazajian and P. J. Harding. “Constraints on WIMP and Sommerfeld-enhanced dark matter annihilation from HESS observations of the galactic center”. In: *Journal of Cosmology and Astroparticle Physics* 2012.01 (2012), p. 041.

[25] J. Aleksić, S. Ansoldi, L. A. Antonelli, et al. “Optimized dark matter searches in deep observations of Segue 1 with MAGIC”. In: *Journal of Cosmology and Astroparticle Physics* 2014.02 (2014), p. 008.

[26] V. A. Acciari et al. “VERITAS search for VHE gamma-ray emission from dwarf spheroidal galaxies”. In: *The Astrophysical Journal* 720.2 (2010), p. 1174.

[27] A. Acharyya et al. “Sensitivity of the Cherenkov Telescope Array to a dark matter signal from the Galactic centre”. In: *Journal of Cosmology and Astroparticle Physics* 2021.01 (Jan. 2021), 057–057. ISSN: 1475-7516. DOI: `10.1088/1475-7516/2021/01/057`.

[28] A. Achterberg et al. “First Year Performance of The IceCube Neutrino Telescope”. In: *Astropart. Phys.* 26 (2006), pp. 155–173. DOI: `10.1016/j.astropartphys.2006.06.007`. arXiv: `astro-ph/0604450`.

[29] K. Abe et al. “Indirect search for dark matter from the Galactic Center and halo with the Super-Kamiokande detector”. In: *Physical Review D* 102.7 (Oct. 2020). ISSN: 2470-0029. DOI: `10.1103/physrevd.102.072002`.

[30] K. C. Y. Ng et al. “Sensitivities of KM3NeT on decaying dark matter”. In: (July 2020). arXiv: `2007.03692 [astro-ph.HE]`.

[31] P. Picozza et al. “PAMELA - A payload for antimatter matter exploration and light-nuclei astrophysics”. In: *Astroparticle physics* 27.4 (2007), pp. 296–315.

[32] M. Ackermann et al. “Measurement of separate cosmic-ray electron and positron spectra with the Fermi Large Area Telescope”. In: *Physical Review Letters* 108.1 (2012), p. 011103.

[33] F. Barao. “AMS - Alpha magnetic spectrometer on the international space station”. In: *Nuclear Instruments and Methods in Physics Research Section A: Accelerators, Spectrometers, Detectors and Associated Equipment* 535.1-2 (2004), pp. 134–138.

[34] O. Adriani et al. “An anomalous positron abundance in cosmic rays with energies 1.5 - 100 GeV”. In: *Nature* 458.7238 (2009), pp. 607–609.

[35] M. Aguilar et al. “First Result from the Alpha Magnetic Spectrometer on the International Space Station: Precision Measurement of the Positron Fraction in Primary Cosmic Rays of 0.5–350 GeV”. In: *Phys. Rev. Lett.* 110 (14 Apr. 2013), p. 141102. DOI: `10.1103/PhysRevLett.110.141102`.

[36] S. Profumo. “Dissecting cosmic-ray electron-positron data with Occam’s Razor: the role of known Pulsars”. In: *Open Physics* 10.1 (2012), pp. 1–31.

[37] P. J. Fox et al. “Missing energy signatures of dark matter at the LHC”. In: *Phys. Rev. D* 85 (5 Mar. 2012), p. 056011. DOI: `10.1103/PhysRevD.85.056011`.

[38] O. Buchmueller, C. Doglioni, and L. T. Wang. “Search for dark matter at colliders”. In: *Nature Physics* 13.3 (2017), pp. 217–223.

[39] M. Aaboud et al. “Search for dark matter at $\sqrt{s} = 13\mathrm{TeV}$ in final states containing an energetic photon and large missing transverse momentum with the ATLAS detector”. In: *The European Physical Journal C* 77.6 (June 2017). ISSN: 1434-6052. DOI: `10.1140/epjc/s10052-017-4965-8`.

[40] A. M. Sirunyan et al. “Search for dark matter particles produced in association with a Higgs boson in proton-proton collisions at $\sqrt{\mathrm{s}} = 13$ TeV”. In: *Journal of High Energy Physics* 2020.3 (Mar. 2020). ISSN: 1029-8479. DOI: `10.1007/jhep03(2020)025`.

[41] P. Cushman et al. *Snowmass CF1 Summary: WIMP Dark Matter Direct Detection*. 2013. arXiv: `1310.8327 [hep-ex]`.

[42] Y. Wang et al. “Improved limits on solar axions and bosonic dark matter from the CDEX-1B experiment using the profile likelihood ratio method”. In: *Physical Review D* 101.5 (2020), p. 052003.

[43] R. Agnese et al. “Search for low-mass weakly interacting massive particles with SuperCDMS”. In: *Physical Review Letters* 112.24 (2014), p. 241302.

[44] E. Armengaud et al. "Constraints on low-mass WIMPs from the EDELWEISS-III dark matter search". In: *Journal of Cosmology and Astroparticle Physics* 2016.05 (2016), p. 019.

[45] F. Petricca et al. "First results on low-mass dark matter from the CRESST-III experiment". In: *Journal of Physics: Conference Series*. Vol. 1342. 1. IOP Publishing. 2020, p. 012076.

[46] C Amole et al. "Dark matter search results from the PICO-60 CF 3 I bubble chamber". In: *Physical Review D* 93.5 (2016), p. 052014.

[47] S. Baum, K. Freese, and C. Kelso. "Dark Matter implications of DAMA/LIBRA-phase2 results". In: *Physics Letters B* 789 (2019), pp. 262–269.

[48] J. Amare et al. "Annual Modulation Results from Three Years Exposure of ANAIS-112". In: *Phys. Rev. D* 103.10 (2021), p. 102005. DOI: `10.1103/PhysRevD.103.102005`. arXiv: `2103.01175 [astro-ph.IM]`.

[49] G. Adhikari et al. "Strong constraints from COSINE-100 on the DAMA dark matter results using the same sodium iodide target". In: (Apr. 2021). DOI: `10.1126/sciadv.abk2699`. arXiv: `2104.03537 [hep-ex]`.

[50] K. Abe et al. "Direct dark matter search by annual modulation in XMASS-I". In: *Physics Letters B* 759 (2016), pp. 272–276.

[51] P. A. Amaudruz et al. "First results from the DEAP-3600 dark matter search with argon at SNOLAB". In: *Physical Review Letters* 121.7 (2018), p. 071801.

[52] P. Agnes et al. "Low-mass dark matter search with the DarkSide-50 experiment". In: *Physical Review Letters* 121.8 (2018), p. 081307.

[53] A. Rubbia. "ArDM: a ton-scale liquid Argon experiment for direct detection of Dark Matter in the Universe". In: *Journal of Physics: Conference Series*. Vol. 39. 1. IOP Publishing. 2006, p. 028.

[54] D. S. Akerib et al. "Results from a search for dark matter in the complete LUX exposure". In: *Physical Review Letters* 118.2 (2017), p. 021303.

[55] Q. Wang et al. "Results of dark matter search using the full PandaX-II exposure". In: *Chinese Physics C* 44.12 (2020), p. 125001.

[56] E. Aprile et al. "Excess electronic recoil events in XENON1T". In: *Phys. Rev. D* 102.7 (2020), p. 072004. DOI: `10.1103/PhysRevD.102.072004`. arXiv: `2006.09721 [hep-ex]`.

[57] M. Schumann. "Direct detection of WIMP dark matter: concepts and status". In: *Journal of Physics G: Nuclear and Particle Physics* 46.10 (2019), p. 103003.

[58] SuperCDMS. *Dark Matter Limit Plotter*. Version 5.16, Updated 03.09.2021. URL: `https://supercdms.slac.stanford.edu/dark-matter-limit-plotter`.

[59] R. A. Llewellyn P. A. Tipler. *Modern Physics*. Ed. by Jessica Fiorillo. W.H. Freeman and Company, 2012. ISBN: 978-1-4292-5078-8.

[60] F. Reines and C. L. Cowan Jr. "Detection of the free neutrino". In: *Physical Review* 92.3 (1953), p. 830.

[61] R. Davis Jr., D. S. Harmer, and K. C. Hoffman. "Search for neutrinos from the sun". In: *Physical Review Letters* 20.21 (1968), p. 1205.

[62] J. N. Abdurashitov et al. "Solar neutrino flux measurements by the Soviet-American gallium experiment (SAGE) for half the 22-year solar cycle". In: *Journal of Experimental and Theoretical Physics* 95.2 (2002), pp. 181–193.

[63] M. Altmann et al. "Complete results for five years of GNO solar neutrino observations". In: *Physics Letters B* 616.3-4 (2005), pp. 174–190.

[64] S. P. Mikheyev and A. Y. Smirnov. "Resonant neutrino oscillations in matter". In: *Progress in Particle and Nuclear Physics* 23 (1989), pp. 41–136.

[65] L. Wolfenstein. "Neutrino oscillations in matter". In: *Physical Review D* 17.9 (1978), p. 2369.

[66] Y. Fukuda et al. "Evidence for oscillation of atmospheric neutrinos". In: *Physical Review Letters* 81.8 (1998), p. 1562.

[67] Q. R. Ahmad et al. "Direct evidence for neutrino flavor transformation from neutral-current interactions in the Sudbury Neutrino Observatory". In: *Physical Review Letters* 89.1 (2002), p. 011301.

[68] N. Agafonova et al. "Observation of tau neutrino appearance in the CNGS beam with the OPERA experiment". In: *Progress of theoretical and experimental physics* 2014.10 (2014), p. 101C01.

[69] K. Abe et al. "Observation of electron neutrino appearance in a muon neutrino beam". In: *Physical Review Letters* 112.6 (2014), p. 061802.

[70] D. G. Michael et al. "Observation of muon neutrino disappearance with the MINOS detectors in the NuMI neutrino beam". In: *Physical Review Letters* 97.19 (2006), p. 191801.

[71] S. M. Bilenky and C. Giunti. "Neutrinoless double-beta decay: a probe of physics beyond the standard model". In: *International Journal of Modern Physics A* 30.04n05 (2015), p. 1530001.

[72] M. G. Inghram and J. H. Reynolds. "Double beta-decay of Te 130". In: *Physical Review* 78.6 (1950), p. 822.

[73] S. R. Elliott, A. A. Hahn, and M. K. Moe. "Direct evidence for two-neutrino double-beta decay in Se 82". In: *Physical Review Letters* 59.18 (1987), p. 2020.

[74] A. Gando et al. "Search for Majorana neutrinos near the inverted mass hierarchy region with KamLAND-Zen". In: *Physical Review Letters* 117.8 (2016), p. 082503.

[75] S. A. Kharusi et al. "nEXO pre-conceptual design report". In: *arXiv:1805.11142* (2018).

[76] C. Adams et al. "Sensitivity of a tonne-scale NEXT detector for neutrinoless double-beta decay searches". In: *Journal of High Energy Physics* 2021.8 (2021), pp. 1–24.

[77] M. Agostini et al. “Probing Majorana neutrinos with double-β decay”. In: *Science* 365.6460 (2019), pp. 1445–1448.

[78] S. I. Alvis et al. “Search for neutrinoless double-β decay in Ge 76 with 26 kg yr of exposure from the Majorana Demonstrator”. In: *Physical Review C* 100.2 (2019), p. 025501.

[79] V. D’Andrea. “Neutrinoless Double Beta Decay Search with ^{76}Ge: Status and Prospect with LEGEND”. In: *arXiv:1905.06572* (2019).

[80] D. Q. Adams et al. “Improved Limit on Neutrinoless Double-Beta Decay in Te 130 with CUORE”. In: *Physical Review Letters* 124.12 (2020), p. 122501.

[81] The CUPID Interest Group. “CUPID pre-CDR”. In: *arXiv:1907.09376* (2019).

[82] C. Capelli. “Search for Dark Matter and Neutrinoless Double Beta Decay in XENON1T and Calibration of the Photosensors in XENONnT”. PhD thesis. Universität Zürich, 2020.

[83] S. Dell’Oro, S. Marcocci, and F. Vissani. “New expectations and uncertainties on neutrinoless double beta decay”. In: *Phys. Rev. D* 90 (3 Aug. 2014), p. 033005. DOI: `10.1103/PhysRevD.90.033005`.

[84] C. Arpesella et al. “First real time detection of 7Be solar neutrinos by Borexino”. In: *Physics Letters B* 658.4 (2008), pp. 101–108.

[85] M. Agostini et al. “Simultaneous precision spectroscopy of pp, ^{7}Be, and pep solar neutrinos with Borexino Phase-II”. In: *Physical Review D* 100.8 (2019), p. 082004.

[86] M. Agostini et al. “Experimental evidence of neutrinos produced in the CNO fusion cycle in the Sun”. In: *Nature* 587 (2020), pp. 577–582. DOI: `10.1038/s41586-020-2934-0`. arXiv: `2006.15115 [hep-ex]`.

[87] A. S. Barabash and A. I. Bolozdynya. “How to detect the dark matter of the Galaxy if it is made up of weakly interacting neutral particles with masses 1-10 GeV/c 2.” In: *Soviet Journal of Experimental and Theoretical Physics Letters* 49.6 (1989), pp. 356–359.

[88] G. J. Alner et al. “First limits on nuclear recoil events from the ZEPLIN I galactic dark matter detector”. In: *Astroparticle Physics* 23.5 (2005), pp. 444–462. ISSN: 0927-6505. DOI: `https://doi.org/10.1016/j.astropartphys.2005.02.004`.

[89] J. Angle et al. “First results from the XENON10 dark matter experiment at the Gran Sasso National Laboratory”. In: *Physical Review Letters* 100.2 (2008), p. 021303.

[90] J. B. Albert et al. “Improved measurement of the $2\nu\beta\beta$ half-life of ^{136}Xe with the EXO-200 detector”. In: *Phys. Rev. C* 89 (1 Jan. 2014), p. 015502. DOI: `10.1103/PhysRevC.89.015502`.

[91] *NIST Chemistry WebBook, NIST Reference Standard Database Number 69*. Accessed: 05.10.2021. DOI: `https://doi.org/10.18434/T4D303`. URL: `https://webbook.nist.gov/`.

[92] E. Aprile and T. Doke. “Liquid xenon detectors for particle physics and astrophysics”. In: *Reviews of Modern Physics* 82.3 (July 2010), 2053–2097. ISSN: 1539-0756. DOI: `10.1103/revmodphys.82.2053`.

[93] J. Wulf. “Direct Dark Matter Search with XENON1T and Developments for Multi-Ton Liquid Xenon Detectors”. PhD thesis. Universität Zürich, 2018.

[94] V. K. Zworykin, G. A. Morton, and L. Malter. “The Secondary Emission Multiplier-A New Electronic Device”. In: *Proceedings of the Institute of Radio Engineers* 24.3 (1936), pp. 351–375. DOI: `10.1109/JRPROC.1936.226435`.

[95] P. Barrow et al. “Qualification tests of the R11410-21 photomultiplier tubes for the XENON1T detector”. In: *Journal of Instrumentation* 12.01 (2017), P01024.

[96] L. Baudis et al. “The first dual-phase xenon TPC equipped with silicon photomultipliers and characterisation with ^{37}Ar”. In: *The European Physical Journal C* 80.5 (2020), pp. 1–13.

[97] L. Baudis, P. Sanchez-Lucas, and K. Thieme. *A measurement of the mean electronic excitation energy of liquid xenon*. 2021. arXiv: `2109.07151 [physics.ins-det]`.

[98] L. Baudis et al. “Characterisation of Silicon Photomultipliers for liquid xenon detectors”. In: *Journal of Instrumentation* 13.10 (2018), P10022.

[99] J. Calvo et al. “Measurement of the attenuation length of argon scintillation light in the ArDM LAr TPC”. In: *Astroparticle Physics* 97 (2018), pp. 186–196. ISSN: 0927-6505. DOI: `https://doi.org/10.1016/j.astropartphys.2017.11.009`.

[100] A. Neumeier et al. “Attenuation of vacuum ultraviolet light in liquid argon”. In: *The European Physical Journal C* 72.10 (2012), pp. 1–9.

[101] C. Macolino. “Recent results from XENON1T and future perspectives for the direct dark matter search with XENONnT”. In: *La Thuile 2021* (Mar. 2021).

[102] L. Baudis. “DARWIN: dark matter WIMP search with noble liquids”. In: *J. Phys. Conf. Ser.* 375 (2012). Ed. by Lothar Oberauer, Georg Raffelt, and Robert Wagner, p. 012028. DOI: `10.1088/1742-6596/375/1/012028`. arXiv: `1201.2402 [astro-ph.IM]`.

[103] G. Bellini et al. “Cosmogenic Backgrounds in Borexino at 3800 m water-equivalent depth”. In: *Journal of Cosmology and Astroparticle Physics* 2013.08 (2013), p. 049.

[104] *Laboratori Nazionali del Gran Sasso (LNGS)*. https://www.lngs.infn.it/en. Accessed: 22.09.2021.

[105] *SNOLAB*. https://www.SNOlab.ca/. Accessed: 22.09.2021.

[106] A. Bettini. “Underground laboratories”. In: *Nuclear Instruments and Methods in Physics Research Section A: Accelerators, Spectrometers, Detectors and Associated Equipment* 626-627 (2011), S64–S68. ISSN: 0168-9002. DOI: `https://doi.org/10.1016/j.nima.2010.05.017`.

[107] D. M. Mei and A. Hime. “Muon-induced background study for underground laboratories”. In: *Phys. Rev. D* 73 (5 Mar. 2006), p. 053004. DOI: `10.1103/PhysRevD.73.053004`.

[108] C. A. J. O’Hare. *Fog on the horizon: a new definition of the neutrino floor for direct dark matter searches*. 2021. arXiv: `2109.03116 [hep-ph]`.

[109] F. Agostini et al. “Sensitivity of the DARWIN observatory to the neutrinoless double beta decay of ^{136}Xe”. In: *Eur. Phys. J. C* 80.9 (2020), p. 808. DOI: `10.1140/epjc/s10052-020-8196-z`. arXiv: `2003.13407 [physics.ins-det]`.

[110] J. Aalbers et al. “Solar neutrino detection sensitivity in DARWIN via electron scattering”. In: *Eur. Phys. J. C* 80.12 (2020), p. 1133. DOI: `10.1140/epjc/s10052-020-08602-7`. arXiv: `2006.03114 [physics.ins-det]`.

[111] E. Aprile et al. “Removing krypton from xenon by cryogenic distillation to the ppq level”. In: *The European Physical Journal C* 77.5 (2017), pp. 1–12.

[112] C. Macolino. “Recent Results from Xenon1T and future perspectives for the direct dark matter search with XENONnT”. La Thuile. 2021. URL: `https://agenda.infn.it/event/25022/contributions/130206/`.

[113] R. Saakyan. “Two-neutrino double-beta decay”. In: *Annual Review of Nuclear and Particle Science* 63 (2013), pp. 503–529.

[114] G. F. Knoll. *Radiation Detection and Measurement*. Ed. by Ann Arbor. John Wiley & Sons, Inc., 1989. ISBN: 0-471-81504-7.

[115] *Evaluated Nuclear Structure Data Files (ENSDF) database*. `http://www.nndc.bnl.gov/ensarchivals/`. Accessed: 03.09.2021.

[116] ThaLibster via Wikimedia Commons. *Decay chain of Thorium-232*. `https://commons.wikimedia.org/wiki/File:Decay_Chain_of_Thorium-232.svg`. Accessed: 07.09.2021. 2017.

[117] ThaLibster via Wikimedia Commons. *Decay chain of Uranium-238*. `https://commons.wikimedia.org/wiki/File:Decay_Chain_of_Uranium-238.svg`. Accessed: 07.09.2021. 2017.

[118] K. Gehrcke et al. *Natürliche Radioaktivität in Baumaterialien und die daraus resultierende Strahlenexposition*. Tech. rep. BfS-SW-14/12. Bundesamt für Strahlenschutz (BfS), 2012. URL: `http://nbn-resolving.de/urn:nbn:de:0221-201210099810`.

[119] R. Arevalo, W. F. McDonough, and M. Luong. “The K/U ratio of the silicate Earth: Insights into mantle composition, structure and thermal evolution”. In: *Earth and Planetary Science Letters* 278.3 (2009), pp. 361–369. ISSN: 0012-821X. DOI: `https://doi.org/10.1016/j.epsl.2008.12.023`.

[120] M. Haffke et al. “Background measurements in the Gran Sasso Underground Laboratory”. In: *Nuclear Instruments and Methods in Physics Research Section A: Accelerators, Spectrometers, Detectors and Associated Equipment* 643.1 (2011), pp. 36–41. ISSN: 0168-9002. DOI: `https://doi.org/10.1016/j.nima.2011.04.027`.

[121] L. Baudis et al. “Gator: a low-background counting facility at the Gran Sasso Underground Laboratory”. In: *Journal of Instrumentation* 6.08 (2011), P08010.

[122] M. Haffke. “Studien des externen Untergrunds eines Flüssig-Xenon-Detektor auf Tonnenskala zum Nachweis von dunkler Materie”. PhD thesis. Universität Zürich, 2010.

[123] E. Aprile et al. “The XENON1T dark matter experiment”. In: *The European Physical Journal C* 77.12 (2017), pp. 1–23.

[124] Dassault Systemes. *SolidWorks*. Version Education Edition 2018 SP5.0. URL: `https://www.solidworks.com/`.

[125] R. F. Lang et al. “A 220Rn source for the calibration of low-background experiments”. In: *Journal of Instrumentation* 11.04 (2016), P04004.

[126] V. Hannen et al. “Limits on the release of Rb isotopes from a zeolite based 83mKr calibration source for the XENON project”. In: *Journal of Instrumentation* 6.10 (2011), P10013.

[127] D. S. Akerib et al. “^{83m}Kr calibration of the 2013 LUX dark matter search”. In: *Physical Review D* 96.11 (2017), p. 112009.

[128] *Live chart of nuclides from Nuclear Data Services (NDS) by the International Atomic Energy Agency (IAEA)*. Accessed: 03.09.2021. URL: `https://www-nds.iaea.org/relnsd/vcharthtml/VChartHTML.html`.

[129] D. S. Akerib et al. “Improved measurements of the β-decay response of liquid xenon with the LUX detector”. In: *Physical Review D* 100.2 (2019), p. 022002.

[130] E. Aprile et al. “Results from a calibration of XENON100 using a source of dissolved radon-220”. In: *Physical Review D* 95.7 (2017), p. 072008.

[131] E. Aprile et al. “XENON1T Dark Matter Data Analysis: Signal Reconstruction, Calibration and Event Selection”. In: *Phys. Rev. D* 100.5 (2019), p. 052014. DOI: `10.1103/PhysRevD.100.052014`. arXiv: `1906.04717 [physics.ins-det]`.

[132] O. Njoya et al. “Measurements of electron transport in liquid and gas Xenon using a laser-driven photocathode”. In: *Nuclear Instruments and Methods in Physics Research Section A: Accelerators, Spectrometers, Detectors and Associated Equipment* 972 (2020), p. 163965. ISSN: 0168-9002. DOI: `https://doi.org/10.1016/j.nima.2020.163965`.

[133] P. Sorensen. “Anisotropic diffusion of electrons in liquid xenon with application to improving the sensitivity of direct dark matter searches”. In: *Nuclear Instruments and Methods in Physics Research Section A: Accelerators, Spectrometers, Detectors and Associated Equipment* 635.1 (Apr. 2011), 41–43. ISSN: 0168-9002. DOI: `10.1016/j.nima.2011.01.089`.

[134] E. Aprile et al. “Energy resolution and linearity of XENON1T in the MeV energy range”. In: *The European Physical Journal C* 80.8 (2020). DOI: `10.1140/epjc/s10052-020-8284-0`.

[135] E. Aprile et al. “The XENON100 Dark Matter Experiment”. In: *Astropart. Phys.* 35 (2012), pp. 573–590. DOI: `10.1016/j.astropartphys.2012.01.003`. arXiv: `1107.2155 [astro-ph.IM]`.